

# Modeling and Optimizing Space Cooling with Solar Energy

Exploring the Potential of Ejector-Boosted and Mechanical Sub-Cooling Cycles

ME55035: EFPT MSc Thesis

Toon Peters

# Modeling and Optimizing Space Cooling with Solar Energy

## Exploring the Potential of Ejector-Boosted and Mechanical Sub-Cooling Cycles

by

Toon Peters

to obtain the degree of Master of Science  
at the Delft University of Technology,  
to be defended publicly on Tuesday March 4, 2025 at 10:30 AM.

Student number: 4955536  
Project duration: April 9, 2024 – March 4, 2025  
Thesis committee: Dr. ir. E. Zanetti, TU Delft, supervisor  
Prof. dr. K. Hooman, TU Delft, co-supervisor  
Dr. ir. M. Ramdin, TU Delft

Cover: Array of air conditioning condensing units in Hong Kong [1].

An electronic version of this thesis is available at <http://repository.tudelft.nl/>.

# Preface

This thesis project was conducted at the Delft University of Technology. The university's slogan, 'Impact for a better society,' is reflected in this thesis, which aims to serve as an example and inspiration for improved, more sustainable refrigeration in residential applications. I express my deepest gratitude to Dr. Emanuele Zanetti, my supervisor, for his steadfast guidance, expert support, inspirational suggestions and the countless hours he dedicated to assist me in this thesis project. Over the past few months, our constructive discussions and the positive attitude of Dr. Zanetti helped me see this project through. Additionally, I thank Prof. Kamel Hooman for his co-supervising, suggestions and support. I would also like to express a word of appreciation to Dr. Marloes Peeters-Reus for her logistical support.

This thesis project has supplied me with valuable knowledge on both the potential and challenges of sustainable methods for refrigeration. With this project, I hope to inspire and aid further research and development in the field of sustainable refrigeration.

*Toon Peters*  
*February 2025*

# Abstract

Heating and cooling systems contribute to approximately 50% of the world's final energy consumption, highlighting their crucial role in the global energy transition. Ejector refrigeration cycles have the potential to convert heat into cooling, thereby improving refrigeration sustainability. This study aims to provide a thermodynamic performance analysis of solar ejector refrigeration cycles, specifically focusing on their applicability for residential air conditioning. To provide a framework for ejector refrigeration, all components of a solar ejector refrigeration system are analyzed, detailing their fundamental principles, working mechanisms and relevant nomenclature. The emphasis of this part of the study lies on the ejector itself, including an analysis of key factors determining ejector performance such as entrainment ratios, and the definition of ejector efficiency along with typical values.

Next, conventional and ejector refrigeration cycles are explained, highlighting the function of the ejector inside a refrigeration cycle. An overview of refrigerants, emphasizing R744 ( $\text{CO}_2$ ) is also included. Following this, a short review on thermodynamic ejector modeling is presented, highlighting differences and similarities across existing models in literature. Based on this literature review, two thermodynamic ejector models are developed and presented. The first model can predict the outlet saturation temperature with a maximum error of 1.54 °C for known entrainment ratios. The second thermodynamic ejector is able to predict entrainment ratios and outlet pressures with an average error of 5.86% and is used for the subsequent simulations.

Three ejector refrigeration cycles are presented in terms of configuration and COP calculation. One of the presented cycles uses ejector refrigeration for mechanical sub-cooling of a R744 vapor compression cycle. A thermodynamic model is developed for both the mechanical sub-cooling cycle and a hybrid ejector refrigeration cycle to evaluate their seasonal performance. The results of this evaluation are presented through a comparative study, comparing the performance of the proposed ejector refrigeration cycles to reference vapor compression refrigeration cycles. This comparison is carried out in four distinct Köppen climate types: tropical, arid, temperate and continental. The proposed hybrid ejector refrigeration system shows a seasonal coefficient of performance (SCOP) increase between 4.74% and 18.7% across the four climate types through the use of the refrigerant R290 (propane) and a solar thermal collector area of 25 m<sup>2</sup>. The mechanical sub-cooling cycle that combines R290 and R744 displays a SCOP increase between 11.3% and 25.1% through the use of a solar thermal area of 20 m<sup>2</sup>. A multi-ejector design is presented to enhance performance under varying refrigerant mass flow, as well as a short economic analysis of the proposed refrigeration cycles. This research aims to form a starting point for assessing the feasibility and potential of solar ejector refrigeration cycles in residential space cooling.

# Contents

<b>1</b>	<b>Introduction</b>	<b>1</b>
<b>2</b>	<b>Research Objectives and Approach</b>	<b>4</b>
<b>3</b>	<b>Literature Review</b>	<b>7</b>
3.1	Ejector Description . . . . .	7
3.1.1	Working Principle . . . . .	7
3.1.2	Operating Conditions . . . . .	8
3.1.3	Geometry . . . . .	8
3.2	Ejector Efficiency . . . . .	10
3.2.1	Overall Ejector Efficiency . . . . .	10
3.2.2	Ejector Partial Efficiencies . . . . .	11
3.3	Ejector Modeling . . . . .	12
3.4	Ejector Refrigeration Cycles . . . . .	14
3.4.1	Conventional Refrigeration Cycles . . . . .	14
3.4.2	Ejector Refrigeration Cycles . . . . .	14
3.4.3	Refrigerants . . . . .	16
3.5	CO <sub>2</sub> as a Refrigerant . . . . .	17
3.5.1	History . . . . .	17
3.5.2	Challenges . . . . .	17
3.5.3	Transcritical Cycle . . . . .	17
3.5.4	Examples . . . . .	18
3.6	Solar Thermal Collectors . . . . .	19
3.6.1	Flat Plate Collectors . . . . .	19
3.6.2	Evacuated Tube Collectors . . . . .	20
3.6.3	PVT Collectors . . . . .	20
3.6.4	Thermal Efficiency Comparison . . . . .	20
3.6.5	Real-World Performance . . . . .	21
3.7	Heat Exchangers . . . . .	22
3.8	Compressors . . . . .	23
<b>4</b>	<b>Steady-State Thermodynamic Ejector Model</b>	<b>24</b>
4.1	Introduction . . . . .	24
4.1.1	Parameter identification . . . . .	24
4.2	Ejector Model 1 . . . . .	25
4.2.1	Modeling Procedure Model 1 . . . . .	25
4.2.2	Validation Model 1 . . . . .	29
4.3	Ejector Model 2 . . . . .	31
4.3.1	Modeling Procedure Model 2 . . . . .	31
4.3.2	Ejector Model 2 Validation . . . . .	35
4.3.3	Efficiency Analysis Ejector Model 2 . . . . .	38
4.4	Modeling Methods . . . . .	40
4.4.1	Speed of Sound in Two-Phase Flow . . . . .	40
4.4.2	Iterating procedure . . . . .	41

<b>5</b>	<b>Ejector Refrigeration Cycles</b>	<b>42</b>
5.1	Hybrid Ejector Refrigeration Cycle 1 . . . . .	42
5.1.1	Configuration . . . . .	42
5.1.2	Coefficient of Performance Hybrid 1 . . . . .	43
5.2	Hybrid Ejector Refrigeration Cycle 2 . . . . .	44
5.2.1	Configuration . . . . .	44
5.2.2	Coefficient of Performance Hybrid 2 . . . . .	44
5.3	Mechanical Sub-Cooling Cycle . . . . .	45
5.3.1	Configuration . . . . .	45
5.3.2	Coefficient of Performance MSC . . . . .	45
5.4	Multi Ejector Design . . . . .	47
5.5	Seasonal Performance Evaluation and Economic Analysis . . . . .	48
<b>6</b>	<b>Results</b>	<b>51</b>
6.1	Vapor Compression Cycle with PV Panels . . . . .	52
6.2	Hybrid 1 . . . . .	53
6.2.1	Influence Secondary Pressure on COP Hybrid 1 . . . . .	53
6.2.2	Influence Ambient Temperature on COP Hybrid 1 . . . . .	54
6.2.3	Hourly Coefficient of Performance Hybrid 1 . . . . .	57
6.2.4	Seasonal Coefficient of Performance Hybrid 1 . . . . .	58
6.2.5	Rate of Success Hybrid 1 . . . . .	60
6.2.6	Ejector Performance Hybrid 1 . . . . .	61
6.3	Mechanical Sub-Cooling Cycle . . . . .	63
6.3.1	Influence Ambient Temperature on COP MSC . . . . .	63
6.3.2	Hourly Coefficient of Performance MSC . . . . .	65
6.3.3	Seasonal Coefficient of Performance MSC . . . . .	66
6.3.4	Cooling Surplus MSC . . . . .	67
6.3.5	Ejector Performance MSC . . . . .	68
6.4	Multi Ejector Design . . . . .	70
6.5	Economic Analysis . . . . .	71
<b>7</b>	<b>Discussion</b>	<b>72</b>
<b>8</b>	<b>Conclusion and Recommendations</b>	<b>77</b>
	<b>References</b>	<b>81</b>
<b>A</b>	<b>Absorption Refrigeration Cycles</b>	<b>90</b>
<b>B</b>	<b>Refrigerants</b>	<b>91</b>
<b>C</b>	<b>Matlab Script Ejector Model 2</b>	<b>92</b>
<b>D</b>	<b>Symbol List</b>	<b>98</b>
<b>E</b>	<b>Matlab Script Hybrid 1 and MSC</b>	<b>99</b>
<b>F</b>	<b>Ejector Array Optimization Script</b>	<b>107</b>
<b>G</b>	<b>Pressure Optimization R744 Vapor Compression</b>	<b>108</b>

# List of Figures

1.1	Projected increase in surface temperature between 2015 and 2050 [3]. . . . .	1
1.2	Predicted increase in number of AC units between 2024 and 2050. Data: [5]. . .	2
1.3	Projected effect of Kigali Amendment on HFC-emissions, radiative forcing and surface temperature increase due to HFCs [9]. . . . .	2
1.4	Example of an ejector [11]. . . . .	3
2.1	Visual representation of research approach. . . . .	6
3.1	Drawing of an ejector with motive, suction and discharge flows. Image: [20]. . . .	7
3.2	Operational modes ejector for fixed secondary inlet pressure $P_s$ . . . . .	8
3.3	Schematic drawing ejector with relevant geometrical parameters. . . . .	9
3.4	Entrainment ratio versus back pressure for different nozzles by Yang et al. [25]. . .	9
3.5	Schematic drawing variable geometry ejector by Gutiérrez and León [26]. . . . .	10
3.6	Drawing, P,h- and T,s-diagram of a vapor compression refrigeration cycle. . . . .	14
3.7	Schematic drawing of an ejector refrigeration cycle. . . . .	15
3.8	T,s-diagram of an ejector refrigeration cycle. . . . .	15
3.9	P,h-diagram of an ejector refrigeration cycle. . . . .	16
3.10	T,s-diagram of a theoretical transcritical cycle. . . . .	18
3.11	R744 ejector cooling cycles 1 (a) & 2 (b) studied by Yadav and Sarkar [57]. . . . .	18
3.12	Flat plate solar thermal collectors. Image: [59]. . . . .	19
3.13	Evacuated tube solar thermal collectors. Image: [60]. . . . .	20
3.14	Thermal efficiency flat plate and evacuated tube collector vs $T_{sc} - T_{air}$ . . . . .	21
3.15	Temperature distribution inside parallel (left) and counter-current (right) HEX. .	22
3.16	Diagram of a rotary compressor (a) and reciprocal compressor (b). Images: [75].	23
4.1	Schematic drawing of ejector by Ma et al. [44]. . . . .	25
4.2	Expanding flowcore and cross section before mixing. . . . .	32
4.3	Ejector model 2 flowchart. . . . .	34
4.4	Entrainment ratio prediction model 2 versus outlet saturation temperature. . . .	38
4.5	$\eta_{ejector}$ vs $P_s$ and $P_p$ for different pressure lifts. . . . .	39
4.6	Experimental validation of relation by Nguyen et al. [80]. . . . .	40
4.7	Visual representation of the bisection method. . . . .	41
5.1	Schematic drawing of hybrid 1. . . . .	42
5.2	Hybrid 1 simulation flowchart. . . . .	43
5.3	Schematic drawing of hybrid 2. . . . .	44
5.4	Schematic drawing of MSC. . . . .	45
5.5	Mechanical sub-cooling cycle simulation flowchart. . . . .	46
5.6	Visualization of an array of 4 ejectors. . . . .	47
5.7	World map with reviewed locations. . . . .	48
6.1	Seasonal simulation vapor compression cycle with PV panels. Data: [95]. . . . .	52
6.2	COP hybrid 1 vs secondary inlet pressure. . . . .	53
6.3	$COP_{H1}$ and $COP_{vc}$ vs ambient temperature, $G = 600 [W/m^2]$ . . . . .	54
6.4	$COP_{H1}$ and $COP_{vc}$ vs ambient temperature, $G = 900 [W/m^2]$ . . . . .	55
6.5	$COP_{H1}$ and $COP_{vc}$ vs ambient temperature, $G = 1200 [W/m^2]$ . . . . .	55
6.6	Hourly COP in hybrid 1 for all four locations. . . . .	57
6.7	SCOP hybrid 1 vs area of solar panels. . . . .	59

6.8	Distribution and average of achieved ejector efficiencies $\eta_{ejector}$ in hybrid 1 for all four locations. . . . .	61
6.9	Distribution and average of $\gamma$ in hybrid 1. . . . .	62
6.10	$COP_{MSC}$ and $COP_{vc}$ vs ambient temperature, $G = 600 [W/m^2]$ . . . . .	63
6.11	$COP_{MSC}$ and $COP_{vc}$ vs ambient temperature, $G = 900 [W/m^2]$ . . . . .	64
6.12	$COP_{MSC}$ and $COP_{vc}$ vs ambient temperature, $G = 1200 [W/m^2]$ . . . . .	64
6.13	Hourly COP in MSC for all four locations. . . . .	65
6.14	SCOP MSC vs area of solar panels. . . . .	67
6.15	Distribution and average of achieved ejector efficiencies $\eta_{ejector}$ in MSC for all four locations. . . . .	68
6.16	Distribution and average of $\gamma$ in MSC. . . . .	69
6.17	Distribution of achievable ejector throat areas for 4, 5, 6 and 7 ejectors in parallel. . . . .	70
A.1	Absorption refrigeration cycle. Image: [127]. . . . .	90
G.1	COP R744 vapor compression cycle vs gas-cooler pressure. . . . .	108

# List of Tables

3.1	Overview of overall ejector efficiencies in literature. . . . .	10
3.2	Overview of partial ejector efficiencies in literature. . . . .	11
3.3	Comparison of six models across four criteria. . . . .	13
3.4	Zero-loss efficiencies and specific coefficients of solar thermal collectors. . . . .	21
3.5	Isentropic efficiencies of different compressor types. . . . .	23
4.1	Comparison model 1 to 2014 experiments by Garcia del Valle et al. [81]. . . . .	29
4.2	Comparison model 1 to 2012 experiments by Jia and Wenjian [82]. . . . .	29
4.3	Comparison model 2 to 2014 experiments by Garcia del Valle et al. [81]. . . . .	35
4.4	Comparison model 2 to 2012 experiments by Jia and Wenjian [82]. . . . .	36
4.5	Comparison entrainment prediction Model 2 to 2014 experiments by Garcia del Valle et al. [81]. . . . .	36
4.6	Comparison entrainment prediction model 2 to 2012 experiments by Jia and Wenjian. [82]. . . . .	37
4.7	Comparison Entrainment Prediction Model 2 to 2024 Experiments by Mastrowski et al. [45]. . . . .	37
5.1	Mean daily and maximum temperature and sunshine hours 1991-2020 for reviewed locations. . . . .	49
5.2	Mean and maximum temperature and mean nonzero solar irradiance 2023 for reviewed locations. Data: [95]. . . . .	49
5.3	Assumed component prices 2023 for reviewed locations. . . . .	50
5.4	Electricity prices 2023 for reviewed locations. . . . .	50
6.1	Seasonal energy data for refrigeration and solar generation for reviewed locations. . . . .	52
6.2	COP hybrid 1 at different values of secondary pressure $P_s$ with fixed proportional primary pressure, ambient temperature and solar irradiance. . . . .	54
6.3	Comparison of COPs hybrid 1 for different ambient temperatures and solar irradiance. . . . .	56
6.4	Average COP vapor compression and average, highest and lowest COP hybrid 1. . . . .	58
6.5	Seasonal coefficient of performance hybrid 1 . . . . .	58
6.6	Seasonal coefficient of performance hybrid 1 with 4 ejectors. . . . .	59
6.7	Successful cooling hours. . . . .	60
6.8	Average, highest and lowest $\eta_{ejector}$ hybrid 1. . . . .	61
6.9	Average, highest and lowest $\gamma$ hybrid 1. . . . .	62
6.10	Average COP vapor compression and average, highest and lowest COP MSC. . . . .	65
6.11	Seasonal coefficient of performance MSC . . . . .	66
6.12	Seasonal coefficient of performance MSC with 4 ejectors . . . . .	66
6.13	Hours ejector cycle provides surplus of cooling. . . . .	67
6.14	Average, highest and lowest $\eta_{ejector}$ MSC. . . . .	68
6.15	Average, highest and lowest $\gamma$ MSC. . . . .	69
6.16	Ejector configurations and achievable effective throat areas. . . . .	70
6.17	2023 capital costs of two reference cycles, hybrid 1 and the MSC. . . . .	71
6.18	2023 operational costs of two reference cycles, hybrid 1 and the MSC for reviewed locations. . . . .	71
B.1	Overview of refrigerants. . . . .	91

D.1 Symbol list. Images: [130]. . . . . 98

G.1 COP R744 vapor compression cycle for different gas-cooler pressures. . . . . 108

# Nomenclature

## General Symbols

$\eta$	(Isentropic) efficiency [-]
$\gamma$	Entrainment ratio [ $\frac{\dot{m}_s}{\dot{m}_p}$ ]
$\kappa$	Specific heat ratio [ $\frac{c_{cp}}{c_{cv}}$ ]
$\rho$	Density [ $\frac{kg}{m^3}$ ]
$A$	Area [ $m^2$ ]
$c$	Specific heat [ $\frac{J}{kg \cdot K}$ ]
$D$	Diameter [ $m$ ]
$G$	Solar irradiation [ $\frac{W}{m^2}$ ]
$H$	Enthalpy [ $J$ ]
$h$	Specific enthalpy [ $\frac{J}{kg}$ ]
$M$	Mach number [-]
$P, p$	Pressure [ $bar$ or $Pa$ ]
$R$	Gas constant [ $\frac{L \cdot kPa}{mol \cdot K}$ ]
$S$	Entropy [ $J$ ]
$s$	Specific entropy [ $\frac{J}{kg}$ ]
$T, t$	Temperature [ $^{\circ}C$ or $K$ ]
$u$	Flow velocity [ $\frac{m}{s}$ ]
$V$	Volume [ $m^3$ ]
$v$	Specific volume [ $\frac{m^3}{kg}$ ]

## Subscripts

$a$	primary nozzle exit
$b$	secondary nozzle exit
$c$	condenser
$cp$	constant pressure
$cv$	constant volume
$d$	diffuser
$e$	evaporator
$et$	evacuated tube

<i>fp</i>	flat plate
<i>g</i>	generator
<i>is</i>	isentropic
<i>m1</i>	model 1
<i>m2</i>	model 2
<i>mix</i>	mixing section
<i>n</i>	nozzle
<i>p</i>	primary (motive)
<i>pvt</i>	photovoltaic thermal
<i>r</i>	ratio
<i>s</i>	secondary (suction)
<i>sc</i>	solar collector
<i>solar</i>	solar thermal collector, photovoltaic panel
<i>t</i>	throat

### **Abbreviations**

AC	Air conditioning
CFC	Chlorofluorocarbon
COP	Coefficient of performance
ERC	Ejector refrigeration cycle
GWP	Global warming potential
HC	Hydrocarbon
HFC	Hydrofluorocarbon
HFO	Hydrofluoroolefin
LMTD	Logarithmic mean temperature difference
MERC	Multi-ejector refrigeration cycle
MSC	Mechanical sub-cooling cycle
ODP	Ozone depleting potential
SCOP	Seasonal coefficient of performance
SERC	Solar ejector refrigeration cycle

# Introduction

---

With surface heat records broken year after year and an ever-rising frequency of extreme weather incidents, human-induced climate change might be the most pressing global issue for the immediate future. While nearly all parts of the planet suffer from climate change, effects are not evenly distributed. According to the NASA Goddard Institute for Space Studies, global mean surface temperatures have increased by approximately  $1\text{ }^{\circ}\text{C}$  since the pre-industrial era. However, regional data, from for example India, show increases that are double or even triple that [2]. In figure 1.1, the predicted further increase in surface temperature between 2015 and 2050 can be seen.

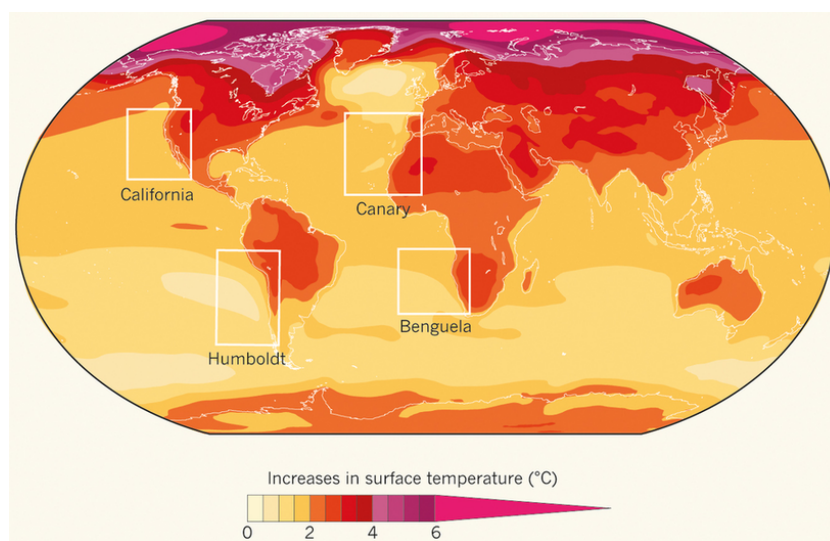


Figure 1.1: Projected increase in surface temperature between 2015 and 2050 [3].

As a result of this global increase in temperature, air conditioning (AC) and residential refrigeration demand is expected to increase at an unprecedented rate in the coming years. India is a notable example of this increasing demand. Its growing middle class together with the high regional sensitivity to climate change leads the International Energy Agency to a prediction of a 23-fold increase in number of AC units [4]. In figure 1.2, the predicted worldwide increase in number of AC units can be seen, indicating a doubling in the next 27 years [5]. While heating and cooling currently represents about 50% of the global final energy consumption [6], Sherman et al. predict that in some countries, the share of energy consumed by air conditioning systems could be up to 75% by 2050 [7].

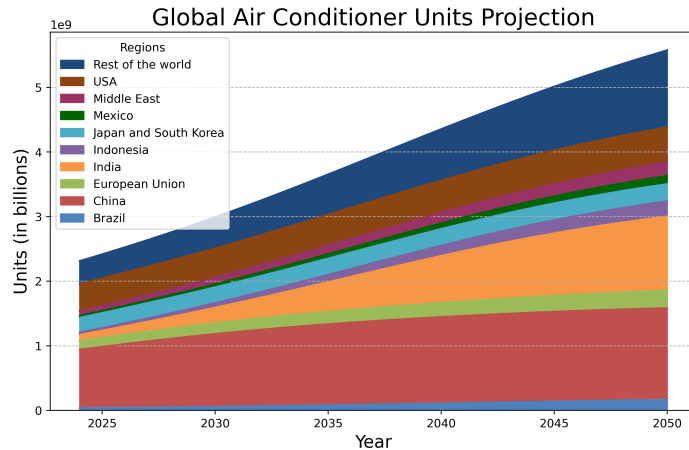


Figure 1.2: Predicted increase in number of AC units between 2024 and 2050. Data: [5].

Simultaneously with this expected air conditioning boom, more and more refrigerants, predominantly chlorofluorocarbons (CFCs) and hydrofluorocarbons (HFCs), are being banned or phased out since the Montreal Protocol of 1987 [8]. Haloalkanes, among them refrigerants commonly used in the past (and still in use today), are found to be responsible for the depletion of the ozone layer. On top of these ozone depleting capabilities, refrigerants often have a high global warming potential (GWP), ranging from 10 to 10000  $CO_2$ -equivalents. In 2016, the Kigali Amendment was added to the Montreal Protocol. The amendment requires a phased decrease in the consumption and production of high-GWP HFCs by over 80 percent, measured in  $CO_2$ -equivalents, between 2016 and 2045 [9]. This will directly have a large effect on surface temperature rise as can be seen in figure 1.3.

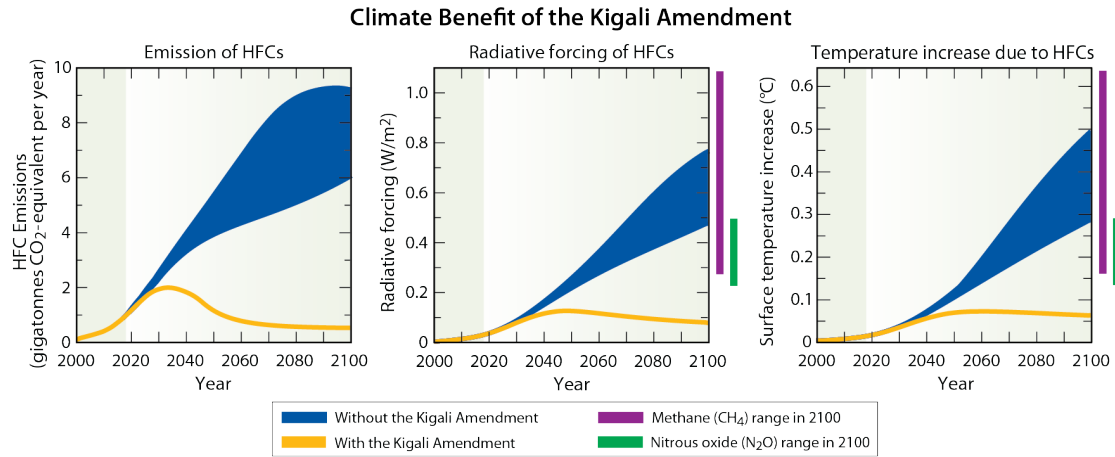


Figure 1.3: Projected effect of Kigali Amendment on HFC-emissions, radiative forcing and surface temperature increase due to HFCs [9].

Even more recent than the Kigali Amendment to the Montreal Protocol, the European Union

published new, stricter regulations on the use of fluorinated greenhouse gases [10]. One of the prohibitions presented in the 2024 restrictions is the 2029 ban of refrigerants with a GWP of more than 150 in split air-to-air systems, the most common type of residential and commercial refrigeration system.



Figure 1.4: Example of an ejector [11].

The future image of higher global temperatures, in combination with limited options for conventional refrigerants has sparked the interest into more sustainable refrigeration methods. An emerging development in the field of refrigeration cycles is that of ejector refrigeration. An ejector, which can be seen in figure 1.4, is a device that uses a high-pressure fluid to entrain and compress a lower-pressure fluid through momentum transfer. It operates based on the Venturi effect, where the primary fluid accelerates through a nozzle, creating a low-pressure zone that entrains the secondary fluid. In refrigeration cycles, ejectors enable the use of low-grade thermal heat (below  $150\text{ }^{\circ}\text{C}$  [12]) for refrigeration by acting as a thermal compressor [13]. The possibility to use low-grade thermal heat enables the use of sustainable sources like solar thermal collectors. Refrigeration cycles that use heat for compression are known as thermally driven refrigeration cycles. The combination of the ejector and solar thermal collectors results in a so-called solar ejector refrigeration cycle. This is the main topic of this research. By combining such a sustainable heat source with environmentally friendly refrigerants, solar ejector refrigeration could be a promising alternative for residential refrigeration.

In this research, the ejector component is explained, along with all other relevant components of possible ejector refrigeration cycles. Based on a short literature review on current numerical ejector models, two thermodynamic ejector models were created and validated with experiments, to enable simulation of two ejector refrigeration cycles. Of the two simulated cycles, one uses the ejector refrigeration cycle as the direct source of cooling, the other cycle uses an ejector refrigeration cycle as a dedicated mechanical sub-cooler for a vapor compression cycle. The simulations were conducted with weather data from four geographical locations representing four out of five Köppen climate types. The performance of the cycles in terms of COP and SCOP was compared to reference vapor compression cycles. A statistical analysis was done to ensure realistic ejector performance in the simulations. The simulations provide insight into the feasibility and potential of solar ejector refrigeration in residential applications.

# Research Objectives and Approach

---

In this chapter, the existing research gap on the topic of this thesis is identified. Subsequently the research topics covered in this thesis will be presented along with an explanation of the approach.

## 2.1 Previous Research

Ejector refrigeration cycles are not a novelty, as early as 1990 cycles were proposed in literature [14]. Research into the addition of solar collectors as a heat source has also been conducted before [15][16][17], as well as research into the use of sustainable refrigerants [18]. There exists however a research gap in the simulating of ejector refrigeration cycles that combine sustainable refrigerants and solar thermal collectors, under real-world conditions.

## 2.2 Research Objectives

The research gap established in section 2.1, together with the relevance of solar ejector refrigeration as presented in chapter 1, leads to the development of the following research objectives and sub-topics:

### Research objective 1:

*"To develop a steady-state thermodynamic ejector model for simulating ejector refrigeration cycles."*

This research objective leads to the following sub-questions:

- What is the effect of varying ejector geometry on the model?
- What is the effect of varying back pressure on the mass entrainment ratio and the model?

### Research objective 2:

*"To develop and optimize a sustainable solar ejector refrigeration cycle (SERC) for air conditioning."*

This research objective leads to the following key aspects that are to be studied:

- Testing solar ejector refrigeration cycles directly for air conditioning and refrigeration cycles where ejector refrigeration performs mechanical sub-cooling.
- Feasibility study on possibility to use R744, or similar sustainable refrigerants in the proposed cycle.
- Technoeconomic analysis of the SERC including seasonal performance in various climates, comparing to conventional refrigeration cycles.

## 2.3 Approach

This section presents the research approach used to answer the developed research questions from section 2.2. In figure 2.1, a graphical representation of the approach can be seen. This represents in what way answering the sub-questions aids in addressing the main research objectives.

### Literature Review

The literature review that is summarized in chapter 3 was conducted before the theoretical research. It serves as a framework to identify what was researched in the past and where literature can be combined or supplemented to create new results. It also covers essential parameters found in literature and their typical values, that will be used in the theoretical research afterwards.

### Thermodynamic Model Development

The first part of the theoretical research presented in this thesis is the development of two thermodynamic ejector models, these models are developed and evaluated on the basis of pre-determined requirements. The critical step in the development of the thermodynamic models is the validation with experimental works.

### Ejector Refrigeration Cycle Modeling

By using the thermodynamic ejector model developed in the previous part of the theoretical research, a number of different cycles can be tested and evaluated in terms of their thermal and economic performance and sustainability, dealing with the second set of subtopics to arrive at an optimized sustainable solar ejector refrigeration cycle for air conditioning, both as a direct refrigeration system and as a mechanical sub-cooler.

### Evaluation

The findings and information gathered throughout the process are thoroughly analyzed and evaluated to ensure a well-rounded understanding of the research results. The results will be followed by a detailed discussion. Based on this analysis, a well-supported conclusion will be drawn on whether or not aforementioned goal is reached. Recommendations will be provided to guide future work or application of the findings.

## 2.4 Structure

This thesis consists of the introduction, formulation of the research questions together with a presentation of the approach, a literature review and the theoretical research itself. The literature review can be read in chapter 3. The theoretical research is structured in two parts, covering the development of a thermodynamic ejector model in chapter 4 and the presentation of various ejector refrigeration cycles in chapter 5. The proposed ejector refrigeration cycles are evaluated in terms of seasonal performance through the combination of the developed ejector models and weather data to form the results that can be read in chapter 6. These results are discussed in chapter 7 and the paper concludes with recommendations for future research in chapter 8.

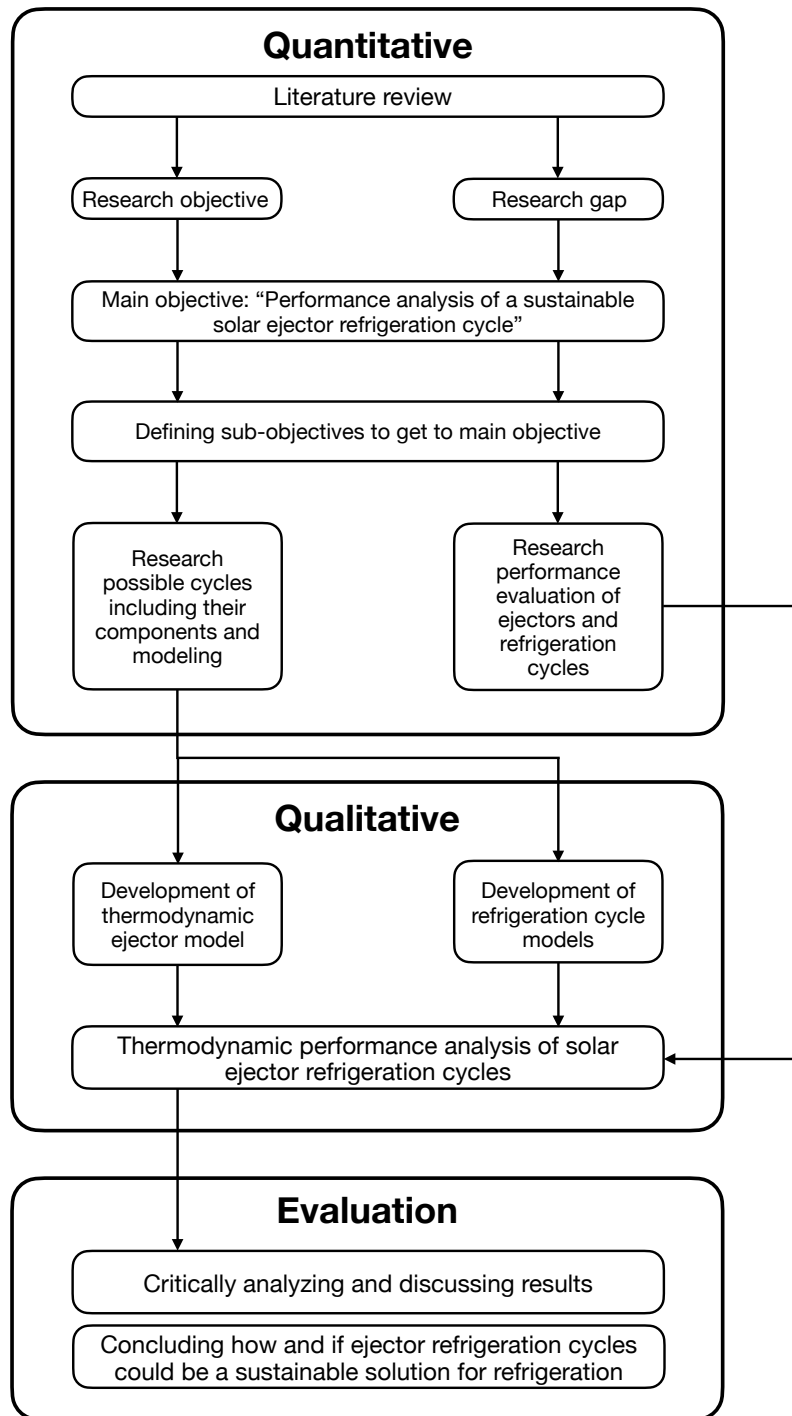


Figure 2.1: Visual representation of research approach.

In this chapter, a short literature review on relevant topics regarding the ejector and ejector refrigeration cycles can be read. The literature review begins with an explanation of ejectors, focusing on their critical parameters, which are essential for understanding their operation. Since the subsequent research will involve theoretical analysis, the review also includes an overview of ejector efficiencies and thermodynamic modeling approaches, which are discussed in sections 3.2 and 3.3, respectively. After covering the topics of efficiencies and modeling, section 3.4 introduces a general ejector refrigeration cycle (ERC). To provide context on sustainable refrigerants, section 3.4.3 provides an overview of the current state of sustainable refrigerants. Thereafter, section 3.5 offers a more detailed overview of  $CO_2$  as a refrigerant because of its distinct implications. Finally, the review examines possible components of solar ejector refrigeration cycles, which are covered in sections 3.6 through 3.8. These sections provide necessary background information on the components relevant to the development of solar ejector refrigeration cycles.

### 3.1 Ejector Description

Ejectors, often described as jet pumps without moving parts, have been in use since the early 1900s [19]. Today, they are primarily utilized for vacuum generation in industries such as chemical and pharmaceutical manufacturing. Other applications include slurry transport in mining and mineral processing, as well as fuel transfer in aircraft systems. This section provides an overview of the working principle, geometry, and operating conditions of ejectors.

#### 3.1.1 Working Principle

Ejectors are a type of passive vacuum pump. The vacuum in an ejector is produced by means of the Venturi effect. An ejector functions by using a high-pressure (primary) fluid to create a low-pressure zone. This low-pressure zone is achieved through a flow velocity increase in a converging-diverging nozzle. The low-pressure zone entrains a secondary fluid. The primary and secondary flow mix, and the combined flow is then discharged through a diffuser, where the pressure of the fluid is increased through a velocity decrease. This results in an outlet pressure higher than the secondary inlet pressure, highlighting an ejector's ability to compress the secondary fluid. A drawing of an ejector with a visualization of the primary (motive), secondary (suction) and mixed fluid (discharge) can be viewed in figure 3.1.

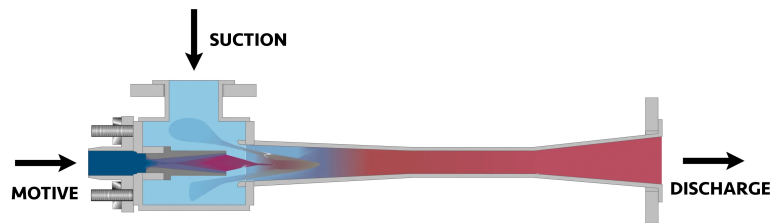


Figure 3.1: Drawing of an ejector with motive, suction and discharge flows. Image: [20].

### 3.1.2 Operating Conditions

Ejectors can operate at a variety of operating conditions. Operating conditions usually form the basis for the geometry of the ejector. This is common practice, as ejector performance is very sensitive to variable operating conditions and therefore the geometry has to be optimized accordingly. A 2007 experimental study by Yapici and Yetişen [21] found that when an ejector with a fixed geometry is exposed to variable operating conditions, the coefficient of performance of a system can drop as much as 120%. An important figure for the performance of ejectors is the entrainment ratio [22], usually denoted with  $\gamma$ . This is defined as the mass flow of the secondary flow over the mass flow of the primary flow.  $\gamma$  is strongly depended on the pressure at the outlet of the ejector  $P_{outlet}$  [23]. The outlet pressure has to be high enough to 'overcome' the back pressure, and prevent backflow. If this requires a very high  $P_{outlet}$ , this implies a relatively high pressure in the low-pressure zone (see section 3.1.1). This in turn limits the entrainment of the secondary fluid, as the pressure difference between the low-pressure zone and the secondary inlet is decreased. The maximum back pressure that allows entrainment by the ejector is known as the critical back pressure. In figure 3.2, the effect of  $P_{outlet}$  on the entrainment ratio  $\gamma$  can be seen, it should be noted that this graph assumes a fixed pressure for the secondary inlet.

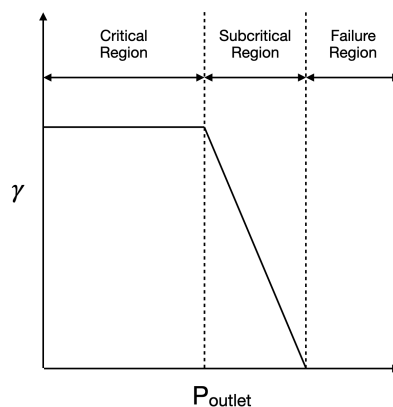


Figure 3.2: Operational modes ejector for fixed secondary inlet pressure  $P_s$ .

### 3.1.3 Geometry

The geometry of ejectors can be divided in two categories, fixed geometry ejectors and variable geometry ejectors. A schematic drawing of an ejector can be seen in figure 3.3. In figure 3.3, different sections can be seen, from left to right: an inlet section, a mixing chamber, a constant area section and a diffuser section. In the inlet section, the primary and secondary fluid enter the ejector. As stated earlier, the primary fluid enters via a converging-diverging nozzle with a throat diameter  $D_t$  and a nozzle exit diameter  $D_a$ . Ejectors can differ greatly in size, with nozzle throat diameters varying between 0.5 millimeters and multiple centimeters [24].

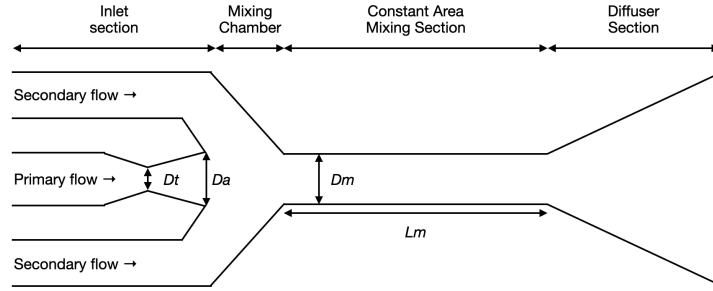


Figure 3.3: Schematic drawing ejector with relevant geometrical parameters.

In order to mitigate the sharp decline in performance due to variable operating conditions, various designs have been presented for ejectors with a variable geometry and nozzle structures. In 2012, Yang et al. [25] tested several nozzle structures with different exit planes (circle-shaped, cross-shaped, elliptical, square and rectangular). Through a CFD study, Yang et al. concluded that the exit plane of the nozzle structure has a large influence on the level of mixing, and thereby on the entrainment ratio  $\gamma$ . Yang et al. also found that a high level of mixing causes energy loss that lowers the critical back pressure. This can be seen in figure 3.4. Note that the shape of the graph in figure 3.4 is similar to the one in figure 3.2.

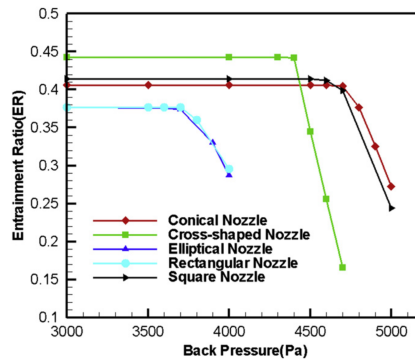


Figure 3.4: Entrainment ratio versus back pressure for different nozzles by Yang et al. [25].

A solution to the challenges found by Yang et al. that is capable of high levels of mixing when back pressure is not an issue, but also has the capability to operate with lower levels of mixing when the critical back pressure should be elevated, could be the variable-geometry ejector design that was presented in 2014 by Gutiérrez and León [26]. This design features an inner ring that moves lengthwise to block or unblock multiple orifices, to alter the primary nozzle outlet and thereby controlling the degree of mixing between the primary and secondary fluid. A schematic drawing with streamlines of the the ejector with the proposed multi-outlet nozzle by Gutiérrez and León can be seen in figure 3.5.

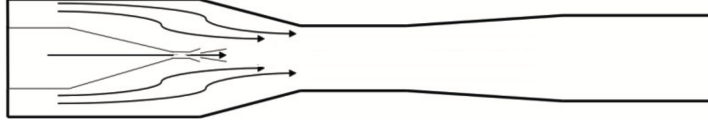


Figure 3.5: Schematic drawing variable geometry ejector by Gutiérrez and León [26].

## 3.2 Ejector Efficiency

In this section an overview of different calculation methods for ejector efficiency can be read, as well as an analysis of their similarities and differences. Also, an overview of typical values for ejector efficiencies can be read.

### 3.2.1 Overall Ejector Efficiency

The efficiency of an ejector in a broad sense can be described by the definition of Köhler et al. [27]. This definition of ejector efficiency considers only external parameters, which are usually easy to measure. The definition of Köhler et al. can be seen in equation 3.1:

$$\eta_{ejector} = \gamma \cdot \frac{h'_{s,is-d} - h_s}{h_p - h'_{p,is-d}} \quad (3.1)$$

where  $h_{s,is-d}$  is the specific enthalpy of an assumed isentropic state change of the secondary flow, between the secondary nozzle inlet and the ejector (diffuser) outlet. In other words,  $h'_{s,is-d}$  depends on the specific entropy of the secondary flow and the ejector outlet pressure.  $h'_{p,is-d}$  is similarly defined for the primary flow, and thus depends on the specific entropy of the primary flow and the ejector outlet pressure.  $\gamma$  is the entrainment ratio, which is defined as the mass flow of the secondary flow over the mass flow of the primary flow:

$$\gamma = \frac{\dot{m}_s}{\dot{m}_p} \quad (3.2)$$

From equation 3.1 it can be seen that the ejector efficiency increases when mass entrainment ratio is increased. As stated earlier the mass entrainment ratio is a key factor in ejector performance. In 2012, Lucas and Köhler [28], experimentally found that there is a relationship between the efficiency of the ejector and the high-side pressure. In table 3.1, an overview of the overall efficiencies of ejectors in literature can be seen.

Authors	Ref.	$\eta_{ejector}$
Nakagawa et al. (2011)	[29]	0.22
Lucas and Köhler (2012)	[28]	0.22
Chen et al. (2014)	[30]	0.15-0.25
Hafner et al. (2014)	[31]	0.2 (constant)
Elbarghthi et al. (2021)	[32]	0.11-0.35

Table 3.1: Overview of overall ejector efficiencies in literature.

### 3.2.2 Ejector Partial Efficiencies

As stated in section 3.1, an ejector consists of a primary nozzle, secondary nozzle, mixing section and diffuser. These four parts of an ejector have individual (isentropic) efficiencies. In 2013, Liu and Groll [33] defined equations for both nozzle efficiencies and the mixing section efficiency. The isentropic efficiency for the primary nozzle is defined in equation 3.3:

$$\eta_p = \frac{h_p - h_t}{h_p - h_{t, is}} \quad (3.3)$$

The isentropic efficiency for the secondary nozzle is defined in equation 3.4:

$$\eta_s = \frac{h_s - h_b}{h_s - h_{b, is}} \quad (3.4)$$

In line with the assumption by Huang et al. [34], Liu and Groll proposed a mixing efficiency that is assumed to cover all friction losses in the mixing section of the ejector. In equation 3.5, the mass conservation between the inlet and outlet of the mixing section that includes  $\eta_{mix}$  can be seen:

$$p_t A_t + \eta_{mix} \rho_t A_t V_t^2 + p_b (A_{mix} - A_t) + \eta_{mix} \rho_b (A_{mix} - A_t) V_b^2 = p_{mix} A_{mix} + \rho_{mix} A_{mix} V_{mix}^2 \quad (3.5)$$

The efficiency of the diffuser  $\eta_d$  was described by Ksayer in 2007 [35] and is defined as the change in enthalpy between the diffuser outlet and primary nozzle outlet in an isentropic ejector over the change in enthalpy in a non-isentropic ejector.

$$\eta_d = \frac{h_{d, out, is} - h_a}{h_{d, out} - h_a} \quad (3.6)$$

In most literature on ejectors, values between 0.7 and 1 are assumed for the efficiencies of the individual parts of an ejector. In 2014, Liu [36] did an extensive review of ejector efficiencies in literature. The findings of Liu, as well as the efficiencies assumed by the ejector models in section 3.3 can be viewed in table 3.2.

Authors	Ref.	$\eta_p$	$\eta_s$	$\eta_{mix}$	$\eta_d$
Aly et al. (1999)	[37]	0.9	0.9	0.95	0.9
Huang et al. (1999)	[34]	0.95	0.85	0.95	0.85
Li and Groll (2005)	[38]	0.9	0.9	-	0.8
Ksayer (2007)	[35]	0.95	1.0	0.9-0.98	1
Zhu et al. (2008)	[39]	0.95	0.85	0.95	0.85
Fangtian and Yitai (2011)	[40]	0.9	0.9		0.8
Manjili and Yavari (2012)	[41]	0.7	0.7	0.95	0.8
Vereda et al. (2012)	[42]	0.85	0.85	0.9	0.8
Chen et al. (2014)	[43]	0.85	0.85	0.9	0.8
Ma et al. (2017)	[44]	0.95	0.85	-	-
Mastrowski et al. (2024)	[45]	0.97	0.45	0.95	0.91

Table 3.2: Overview of partial ejector efficiencies in literature.

In table 3.2, it can be seen that Ksayer used a range of mixing zone efficiencies  $\eta_{mix}$ . Ksayer developed a correlation that relates the mixing zone efficiency to the ratio between the diameter of the constant area and the diameter of the nozzle throat:

$$\eta_{mix} = -0.0113 \left( \frac{D_{mix}}{D_t} \right)^2 + 1.0501 \quad (3.7)$$

### 3.3 Ejector Modeling

To develop a comprehensive understanding of the current state of ejector modeling, six distinct ejector models spanning the period between 1999 and 2024 have been analyzed:

- 1999 steam jet ejector model by Aly et al. [37].
- 2008 simplified ejector model by Zhu et al. [39].
- 2014 optimum working conditions ejector model by Chen et al. [43].
- 2014 one-dimensional ejector model by Kumar and Ooi [46].
- 2016 detailed thermodynamic ejector model by Ma et al. [44].
- 2024 theoretical low-grade heat ejector model by Mastroski et al. [45].

These models were chosen based on their relevance to solar ejector refrigeration and contributions to the field. A key observation is that all the analyzed models share some fundamental similarities, most notably their reliance on predefined efficiencies or loss factors—denoted by  $\eta$ —to account for various inefficiencies such as resistance, choking, and mixing losses. These predefined parameters simplify the modeling process but also highlight an inherent limitation in terms of generalizability. Furthermore, all models assume steady-state operation and consider the ejectors to be adiabatic.

Three of the models (Aly et al., Chen et al. and Kumar and Ooi), are based on the (local) Mach number as a primary parameter in their calculations. Mastrowski et al. incorporated Mach number-based calculations as well, although only for specific parts of the ejector. The models presented by Zhu et al. and Ma et al. use conservation laws for their calculations. Furthermore, the six models use experimental results to validate their theoretical predictions, demonstrating a strong reliance on empirical data to reinforce model accuracy and relevance in the field of ejector modeling.

Despite these similarities, significant differences exist among the models, particularly concerning the geometry of the ejectors and the assumptions that form the basis of their calculations. Zhu et al. and Chen et al. utilize variable geometry ejectors, which offer flexibility in adapting to varying operating conditions. In contrast, Aly et al. and Ma et al. assume fixed geometry ejectors, which simplify the modeling process but potentially limit the applicability under dynamic conditions. Mastrowski et al. propose two modeling strategies, one for ejector design and one for thermodynamic calculations with a fixed-geometry ejector. Furthermore, Aly et al. and Ma et al. initiate their modeling by assuming an initial value for the entrainment ratio,  $\gamma$ , as the starting point of their iterative calculations. On the other hand, Zhu et al., Chen et al., and Kumar and Ooi base their iterative processes on initial pressure assumptions that influence the entrainment.

The model by Zhu et al. introduces a notable deviation by assuming two-dimensional flow instead of the one-dimensional flow assumed by the other models. This two-dimensional approach allows for a more nuanced representation of the flow field, especially in complex geometries. Additionally, Zhu et al. employ the shock circle model in their analysis, which provides an alternative to the conventional shock wave calculations used in the other models. The models by Zhu et al. and Ma et al. also differ from the rest in that they do not require a predefined back pressure for their calculations. This characteristic makes these models potentially more versatile, particularly

in applications where back pressure conditions are uncertain or variable.

Another aspect of the model by Ma et al. is its initial reliance on a predefined efficiency for the nozzle, a common approach among the analyzed models. However, if measured efficiency values are available, the model by Ma et al. incorporates these empirical values, thus enhancing its adaptability and precision. In addition, the model of Ma et al. requires empirical correlations for the hypothetical throat area to support further modeling efforts, a feature that differentiates it from the other models, which do not require this additional empirical input.

In summary, while all six models share foundational assumptions and rely heavily on empirical validation, they differ significantly in their approaches to geometry, initial assumptions, and the specific methods used for flow and efficiency calculations. In table 3.3 an overview of the differences and similarities can be seen.

<b>Model</b>	<b>Dimensions</b>	<b>Base for Calculations</b>	<b>Experimentally Validated</b>	<b>Requires <math>\gamma</math></b>
Aly et al. [37]	1	Mach relations	Yes	Yes
Zhu et al. [39]	2	Conservation laws	Yes	No
Chen et al. [47]	1	Mach relations	Yes	No
Kumar and Ooi [46]	1	Mach relations	Yes	No
Ma et al. [44]	1	Conservation laws	Yes	Yes
Mastrowski et al. [45]	1	Both	Yes	No

Table 3.3: Comparison of six models across four criteria.

## 3.4 Ejector Refrigeration Cycles

In this section, an explanation of conventional and thermally driven refrigeration cycles and the application of ejectors in refrigeration cycles can be read.

### 3.4.1 Conventional Refrigeration Cycles

A conventional refrigeration cycle, often referred to as a vapor compression refrigeration cycle, operates similarly to a reversed Rankine cycle. However, the key components are adapted to serve the specific purpose of refrigeration. In this reversed process, the boiler found in a typical Rankine cycle is substituted by an evaporator. The evaporator's function is to absorb heat from a low-temperature environment, enabling the refrigeration process. Additionally, the turbine of the Rankine cycle, which typically extracts work from the working fluid, is replaced with a compressor. Instead of generating work, the compressor in a refrigeration cycle performs the addition of work to the working fluid and thus consumes energy.

In figure 3.6, the schematic representation of the conventional refrigeration cycle including its main components and configuration can be seen, including its corresponding P-h and T-s diagrams. The schematic highlights the sequential processes that the working fluid undergoes, compression (1→2), condensation (2→3), expansion (3→4), and evaporation (4→1).

In summary, the vapor compression refrigeration cycle mirrors the Rankine cycle in structure but is adapted with specific components like the evaporator and compressor to accomplish the goal of heat extraction from low-temperature environments. Figure 3.6 provides a visualization of both the cycle's layout and its thermodynamic representation.

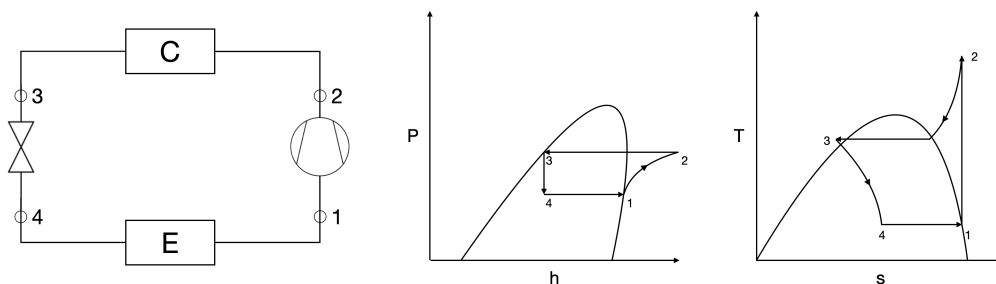


Figure 3.6: Drawing, P,h- and T,s-diagram of a vapor compression refrigeration cycle.

### 3.4.2 Ejector Refrigeration Cycles

As became clear from section 3.1, an ejector can be used to convert the two inlet flows, to a mixed discharge with a pressure higher than the pressure of the secondary flow. Therefore, in many ejector refrigeration cycles in literature, the ejector replaces or assists the compressor. In other words, the evaporator outlet becomes the secondary or suction flow of the ejector. This can be seen in figure 3.7. In figure 3.8, the T,s-diagram of a refrigeration cycle working solely with an ejector, generator and pump can be seen, the dotted lines represent the ejector process of a high pressure and temperature (point 5) and low pressure and temperature stream

(point 1) mixing to form the intermediate pressure outlet stream (point 2). the P,h-diagram of the same cycle can be viewed in figure 3.9. The primary or motive flow of the ejector gets its energy input from a pump and generator, which makes it a thermally-driven refrigeration cycle. Another example of a thermally-driven cycle is an absorption refrigeration cycle, which works by consecutively dissolving a refrigerant in an absorbent and using heat to separate the solution again, thereby acting as a thermal compressor, a more detailed explanation can be read in appendix A. A limitation of absorption refrigeration cycles is the minimum temperature of  $75\text{ }^{\circ}\text{C}$  at which the heat has to be supplied for separation [48]. Since this research centers on using (non-concentrated) solar heat and  $75\text{ }^{\circ}\text{C}$  is difficult to reach (see section 3.6.5) with solar thermal collectors, absorption cycles will not be considered in this research.

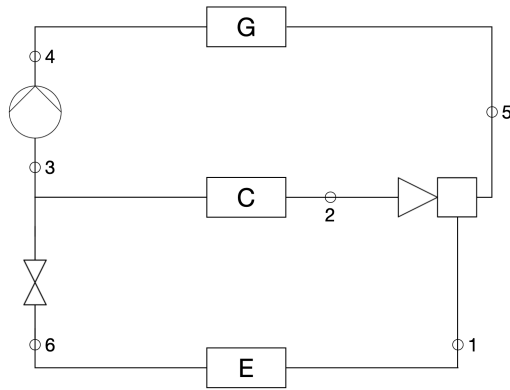


Figure 3.7: Schematic drawing of an ejector refrigeration cycle.

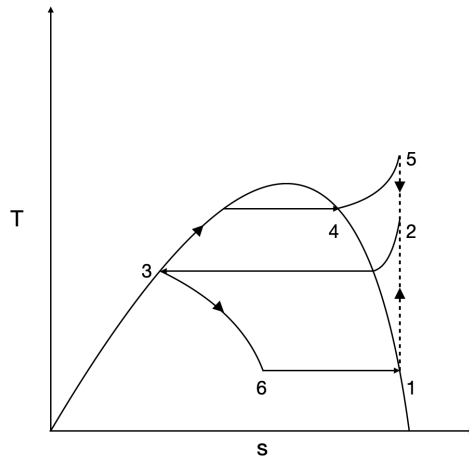


Figure 3.8: T,s-diagram of an ejector refrigeration cycle.

As the power consumption of the pump typically is negligible compared to the generator input [49], the COP of an ejector refrigeration cycle is calculated as the cooling duty over the heat input of the generator. As can be seen from figure 3.7, the ejector outlet pressure should be equal or higher than the desired condenser pressure. The condenser pressure has a lower limit,

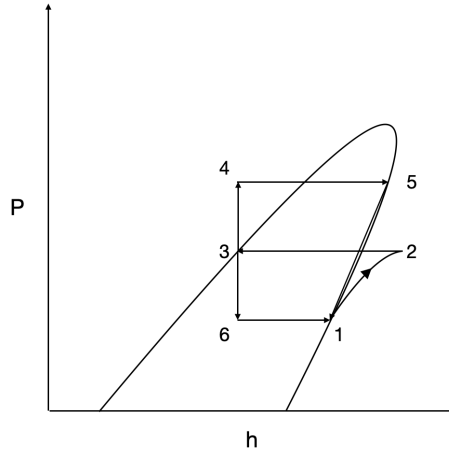


Figure 3.9: P,h-diagram of an ejector refrigeration cycle.

dictated by the ambient conditions of the condenser. In practice it is useful to have a condenser temperature that is relatively high compared to the ambient to ensure condensation and limit required condenser surface area. At higher logarithmic mean temperature difference ( $LMTD$ ) and a constant heat transfer coefficient  $U$ , a smaller heat exchanger area  $A$  results in the same heat transfer  $\dot{Q}_{HEX}$ . In this research, a minimum temperature difference between the condenser and ambient temperature of 5 K is maintained. This is explained in more detail in section 3.7.

### 3.4.3 Refrigerants

Refrigerants play a critical role in thermodynamic systems, serving as the working fluid that undergoes phase transitions to transfer heat in refrigeration cycles. Their selection is governed by a combination of thermodynamic, environmental, and safety considerations, each of which has specific parameters that must be met for optimal performance. Refrigerants typically have low boiling points, ensuring evaporation even at low temperatures on the cold side of the refrigeration [50]. As stated in chapter 1, historically refrigerants are predominantly chlorofluorocarbons (CFC's) and hydrofluorocarbons (HFC's) with high global warming and ozone depleting potentials. Today however, due to previously stated legislation and bans, the demand for sustainable, natural refrigerants like propane,  $CO_2$  and ammonia is increasing [51]. Efficiently using  $CO_2$  as a refrigerant requires specific measures which will be detailed in section 3.5. The combination of an ejector refrigeration cycle with sustainable refrigerants has been explored in 2020 by Galindo et al. [15]. A CFD study on ammonia as a refrigerant in an ERC has been done by Saeid et al. in 2024 [17]. An overview of refrigerants and their relevant properties mentioned in this research can be seen in appendix B.

## 3.5 CO<sub>2</sub> as a Refrigerant

In this section, a short review of the history, challenges and examples of using CO<sub>2</sub> as a refrigerant can be read.

### 3.5.1 History

The use of CO<sub>2</sub> as a refrigerant for comfort cooling began in the 1900s, and peaked in the 1930s. Around that time, most refrigeration cycles were conventional subcritical refrigeration cycles, which in combination with CO<sub>2</sub> as the refrigerant lead to inefficient operation. To counter this inefficiency, a CO<sub>2</sub> refrigeration cycle requires high pressures. High pressure systems often caused leaks, which lead to increased demand for safe and efficient refrigerants. The subsequent invention of CFC's caused a sharp decline in the use of CO<sub>2</sub> as a refrigerant [52].

### 3.5.2 Challenges

As mentioned before, in order to use CO<sub>2</sub> as a refrigerant, high system pressures are required, due to its low critical point temperature (31 °C) and high critical point pressure (7.4 MPa). The low critical point temperature of R744 (The ASHRAE name for CO<sub>2</sub>) excludes efficient operation in a conventional subcritical refrigeration cycle. This stems from the fact that the condenser in the refrigeration cycle will not transfer heat above the critical temperature (the highest temperature at which the substance can exist as a liquid). In a 1994 study, Lorentzen [53] already concluded that the only way to effectively use R744 is in a transcritical cycle.

### 3.5.3 Transcritical Cycle

A transcritical cycle, of which the theoretical T,s-diagram can be viewed in figure 3.10, is a cycle that is not limited by the critical temperature of the working fluid. This is the case because the heat is extracted from the cycle in a temperature glide (2→3 in figure 3.10). In a transcritical cycle, thus in a system with its high pressure above the critical pressure of 7.4 MPa, refrigeration with R744 is possible between -50 °C and 120 °C [54]. The heat rejection in a transcritical cycle happens in the gas-cooler, which takes the place of the condenser in a conventional refrigeration cycle. Though both a condenser and gas-coolers are heat exchangers, they are different because no actual condensation takes place inside a gas-cooler. Instead, the supercritical refrigerant only cools down by rejecting the heat.

High system pressures require robust and expensive system design and components. Because of this, R744 is often ruled out in refrigerant selection [55]. Despite these complexities, research and implementation of R744 refrigeration cycles is increasing because of its environmental benefits. In the United States, the number of R744 refrigeration systems in supermarkets is expected to grow by over 300% between 2023 and 2027 [56], indicating its relevance.

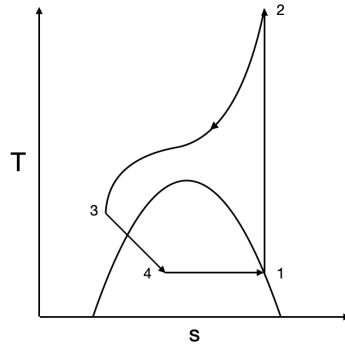


Figure 3.10: T,s-diagram of a theoretical transcritical cycle.

### 3.5.4 Examples

In 2021, Yadav and Sarkar [57] studied 6 different transcritical R744 systems. The first tested cycle can be viewed in figure 3.11a. This cycle consists of a conventional refrigeration cycle, with the addition of a sub-cooler in between the gas cooler and expansion valve. The sub-cooler is part of an ejector cycle, where it replaces the evaporator. The conventional refrigeration cycle uses R744 as the working fluid. The second cycle (figure 3.11b) adds an internal heat exchanger between the evaporator and sub-cooler outlet.

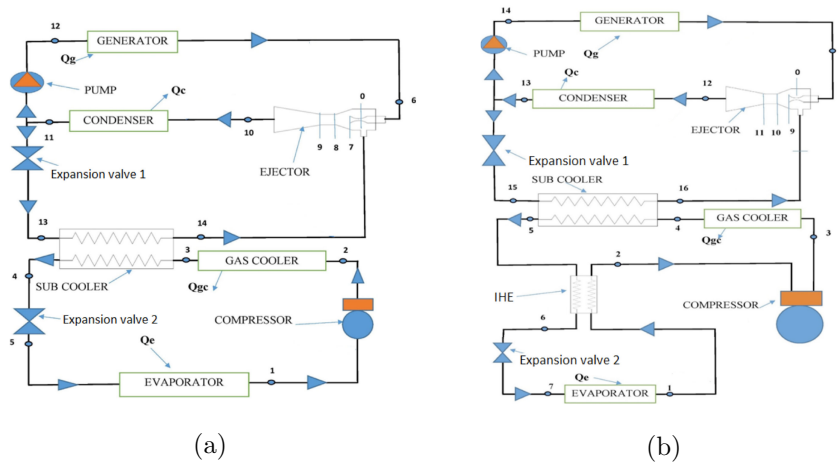


Figure 3.11: R744 ejector cooling cycles 1 (a) & 2 (b) studied by Yadav and Sarkar [57].

Yadav and Sarkar tested the performance of all tested cycles for a cooling capacity of 100 kW. In the test case, cycle 1 showed a COP of 1.013. Yadav and Sarkar found that the best cycle in the case of available waste or renewable heat was cycle 2. Cycle 2 can be viewed in figure 3.11b. Cycle 2 showed a COP of 1.077 without waste heat, and a COP of 2.218 if waste heat was available. A reference cycle, a conventional R744 refrigeration cycle was also tested and achieved a COP of 2.051. Yadav and Sarkar concluded that the COP if every tested cycle increased with increasing evaporator temperature and decreasing ambient temperature.

## 3.6 Solar Thermal Collectors

Solar thermal collectors are a critical part of solar ejector refrigeration cycles, where they take the place of the generator. In this section, an explanation of the different types of solar thermal collectors and their characteristics can be read.

Solar thermal collectors are a type of heat collector that collects heat by absorbing sunlight. Solar thermal collectors can be either concentrated or non-concentrated. In the non-concentrated variant, the area that receives solar radiation is about the same as the area of the absorber. In concentrated solar thermal collectors, the area that receives the solar radiation is much bigger than the absorber area, and usually in the form of a mirror that is focused on the absorber. Due to the larger footprint of concentrated solar thermal collectors, these are almost exclusively used in large (power) generation installations. Commercial solar thermal collectors, relevant for the solar ejector refrigeration cycle, are predominantly non-concentrated collectors. Non-concentrated collectors can be categorized into two types, so-called flat plate collectors and evacuated tube collectors.

### 3.6.1 Flat Plate Collectors

In Europe, 72% of solar thermal collectors are flat plate collectors [58]. A flat plate collector has a sandwich structure consisting of:

1. An optional sheet of glass, serving as insulation to reduce heat loss to the ambient, while allowing most solar radiation to pass through.
2. A sheet of highly conductive material, also known as the absorber plate, usually dark-colored to absorb the most radiation.
3. An array of tubes through which the working fluid passes, thermally connected to the absorber plate.
4. A layer of insulation material to reduce heat loss to the ambient, usually the sides are also insulated.

The collected heat is then transported by the working fluid and used for space heating, or, in the case of a thermally driven/assisted refrigeration cycle, as the heat source of the generator. An image of a flat plate collector installation can be seen in figure 3.12. The losses in a flat plate collector stem from reflection, convection and radiation which will be explained in section 3.6.4.



Figure 3.12: Flat plate solar thermal collectors. Image: [59].

### 3.6.2 Evacuated Tube Collectors

Evacuated tube collectors are the most common type of solar thermal collector worldwide, at nearly 59% in 2022 [58]. They consist of a series of glass tubes, each containing a vacuum layer that acts as insulation, reducing heat loss to the ambient. Inside each tube is the absorber that absorbs the solar radiation and converts it into heat. This heat is transferred to the fluid that circulates through the tubes. An image of an evacuated tube collector setup can be seen in figure 3.13.



Figure 3.13: Evacuated tube solar thermal collectors. Image: [60].

### 3.6.3 PVT Collectors

A third type of solar thermal collector is the photovoltaic thermal, or PVT collector that combines a photovoltaic panel to generate electricity, and a thermal collector to collect heat. The thermal collector essentially cools the PV panel, increasing its electrical efficiency up to 30% with respect to a conventional PV panel [61].

### 3.6.4 Thermal Efficiency Comparison

The thermal efficiency  $\eta_{sc}$  of a solar thermal collector is defined as the useful heat taken out of the collector over the total irradiance that is received by the collector. The thermal efficiency of a solar thermal collector is described by the following relation [62]:

$$\eta_{sc} = \eta_0 - a_1 \cdot T^* - a_2 \cdot (T^*)^2 \quad (3.8)$$

where  $a_1$  and  $a_2$  are the collector-specific first and second order coefficients, respectively and  $T^*$  is defined as:

$$T^* = \left( \frac{T_{sc} - T_{air}}{G} \right) \quad (3.9)$$

where  $T_{sc}$  and  $T_{air}$  are the temperature of the solar collector and the ambient (air), respectively and  $G$  is the solar irradiance in  $\frac{W}{m^2}$ . Typically, flat plate collectors have a higher zero-loss efficiency  $\eta_0$  than evacuated tube collectors, which is explained by the larger amount of losses to reflection in evacuated tube collectors. Flat plate collectors without a glass top sheet have especially little losses due to reflection, albeit at an increase in losses to convection and radiation. Because of the higher degree of insulation, evacuated tubes typically have lower collector-specific coefficients, resulting in higher retention of efficiency at increased difference between the collector and ambient temperature.

Figure 3.14 shows the characteristics of each type of solar thermal collector by plotting the thermal efficiency of the collectors at 3 different values of solar irradiance (cloudy =  $600 \frac{W}{m^2}$ , partly cloudy =  $900 \frac{W}{m^2}$  & sunny =  $1200 \frac{W}{m^2}$ ) against the temperature difference between the solar collector and the ambient. For the comparison, the zero-loss efficiencies and coefficients of collectors that are comparable in size are used. The models and values be seen in table 3.4.

Solar Collector	Type	Ref.	$\eta_0$	$a_1$	$a_2$
CPC 12 INOX by Ritter Energie	Evacuated Tube	[63]	0.56	0.65	0.004
SUN600.20 by Lacaze Energies	Flat Plate	[64]	0.755	3.745	0.015
aH72 M2 by Abora	Flat Plate PVT	[65]	0.7	5.98	0.0

Table 3.4: Zero-loss efficiencies and specific coefficients of solar thermal collectors.

In figure 3.14, the evacuated tube collector efficiency is denoted as  $\eta_{et}$ , while the efficiencies of the flat plate collector and PVT panel are denoted as  $\eta_{fp}$  and  $\eta_{pvt}$ , respectively.

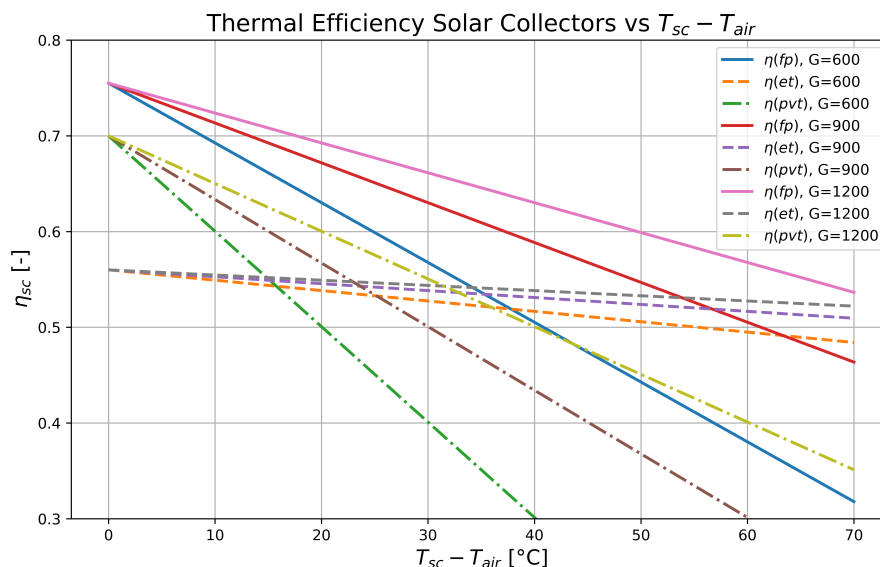


Figure 3.14: Thermal efficiency flat plate and evacuated tube collector vs  $T_{sc} - T_{air}$ .

### 3.6.5 Real-World Performance

In real-world applications, maximum outlet temperatures of up to 95 degrees centigrade are possible for flat plate collectors [66] while evacuated tubes can reach outlet temperatures between 50 and 200 degrees centigrade [67], maximum outlet temperature decreases for increasing mass flow [68].

### 3.7 Heat Exchangers

A frequently used method to model heat exchangers in refrigeration cycles is the logarithmic mean temperature or LMTD method as presented by Bergman et al. [69]. The LMTD is calculated in the following way:

$$LMTD = \frac{\Delta T_1 - \Delta T_2}{\ln\left(\frac{\Delta T_1}{\Delta T_2}\right)} \quad (3.10)$$

where the calculation of  $\Delta T_1$  and  $\Delta T_2$  depends on the flow arrangement inside the heat exchanger. The three types of flow arrangements are parallel, counter-current or cross-current, referring to the flow direction of the two heat exchanging fluids with respect to each other. In figure 3.15, the temperature distribution across a parallel and counter-current heat exchanger can be seen. For cross-current, the distribution is similar to a counter-current heat exchanger.

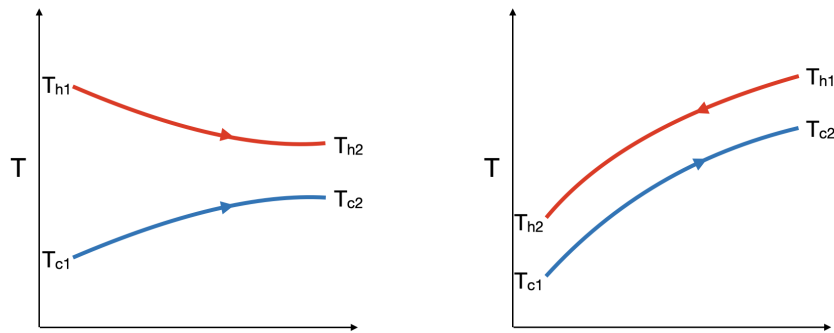


Figure 3.15: Temperature distribution inside parallel (left) and counter-current (right) HEX.

The calculations for  $\Delta T_1$  and  $\Delta T_2$  for a parallel flow heat exchanger are calculated as:

$$\Delta T_1 = T_{h1} - T_{c1}, \Delta T_2 = T_{h2} - T_{c2} \quad (3.11)$$

For a counter-current heat exchanger,  $\Delta T_1$  and  $\Delta T_2$  are calculated differently:

$$\Delta T_1 = T_{h1} - T_{c2}, \Delta T_2 = T_{h2} - T_{c1} \quad (3.12)$$

For a cross-current heat exchanger, the LMTD is adjusted with respect to the LMTD of a counter current heat exchanger with the help of a correction factor  $F$ :

$$LMTD_{cross} = F \cdot LMTD_{counter} \quad (3.13)$$

The correction factor  $F$  depends on the temperature differences inside the heat exchanger and can be found in books like Perry's Chemical Engineers' Handbook [70]. With the LMTD calculated, the heat exchanged within an heat exchanger can be calculated:

$$\dot{Q}_{HEX} = U \cdot A \cdot LMTD \quad (3.14)$$

Where  $U$  is the heat transfer coefficient in  $\frac{W}{m^2 \cdot K}$ , and  $A$  is the exchanger area in  $m^2$ .

### 3.8 Compressors

For the modeling of the compressor in the refrigeration cycle, the ideal isentropic compression is calculated, which is adjusted by the isentropic efficiency, to calculate its energy requirement per kg of mass passing through the compressor. Assuming known inlet and outlet conditions and mass flow, the required compressor work can be calculated as follows [71]:

$$W_{comp} = \frac{h_{2,ideal} - h_1}{\eta_{comp}} \cdot \dot{m}_{comp} \quad (3.15)$$

where  $h_{2,ideal}$  is the enthalpy of the fluid at the outlet of the compressor, which can be calculated by assuming an isentropic compression ( $s_2 = s_1$ ) and calculating the isentropic enthalpy increase for the desired outlet pressure.

#### Compressor types

In the case of residential air conditioning, nowadays the most used compressor type is the rotary compressor [72], that is typically more energy efficient and more quiet than the reciprocal compressor that is used in older air conditioning systems [73]. A diagram of both types of compressor can be seen in figure 3.16. A compressor can also be operated with an inverter, enabling variations mass flow and compression [74]. Compressors operated by an inverter are known as inverter compressors.

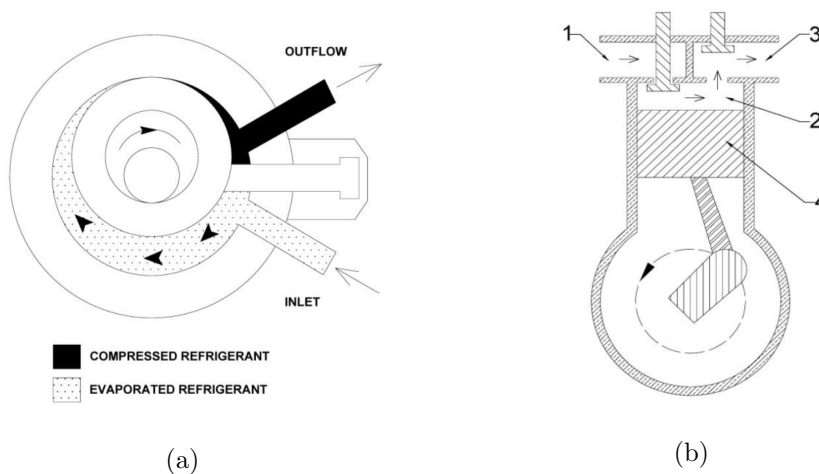


Figure 3.16: Diagram of a rotary compressor (a) and reciprocal compressor (b). Images: [75].

In table 3.5, an overview of the different relevant compressor types and their typical isentropic efficiencies can be seen.

Compressor Type	$\eta_{comp}$	Ref.
Rotary	$\pm 90\%$	[76]
Reciprocal	70%-90%	[77]

Table 3.5: Isentropic efficiencies of different compressor types.

# Steady-State Thermodynamic Ejector Model

---

## 4.1 Introduction

From the literature review, it can be concluded that ejector refrigeration is a potential method for increasing the sustainability of cooling and heating. In this research, analysis is done through modeling of refrigeration cycles. In order to simulate different cycles and thereby analyze the potential of ejectors in refrigeration cycles, a steady-state thermodynamic model for the ejector should be developed. The ejector model should meet the following requirements:

- *Easy to implement in different cycle-models:* by creating the model in a standardized format that takes inlet state variables and converts these to outlet parameters, the model is applicable to multiple refrigeration cycles.
- *Require minimum amount of (measurable) inputs:* in line with the previous requirement, the model should require the minimum amount of parameters.
- *Predict entrainment ratio by combining operating conditions and geometry:* by predicting instead of imposing the entrainment ratio, the model avoids limitation by availability of data from past experimental studies.

### 4.1.1 Parameter identification

This subsection serves to aid in the understanding of which parameters the thermodynamic ejector model should require as inputs. The parameters can be divided into three categories; state variables, efficiencies, and geometrical parameters. According to the state principle of thermodynamics, the state of a simple compressible system can be specified by two independent, intensive properties [78]. Because of this, the ejector model will need two of the following: enthalpy (in  $\frac{kJ}{kg}$ ), absolute pressure (in  $Pa$ ) and temperature (in  $K$ ) to obtain the state of the incoming primary and secondary flow.

The efficiency parameters of the ejector model comprise the partial efficiencies as presented in section 3.2.2. The overall ejector efficiency presented in section 3.2.1 is used to verify realistic output of the model.

In section 3.1.3, the geometrical parameters were presented. For the thermodynamic ejector model, the following parameters are required for calculations:

- $D_t$ ; the diameter of the primary nozzle throat, where the primary flow reaches the local speed of sound i.e. where  $M = 1$ . This diameter dictates the primary mass flow (and by entrainment ratio thus also the secondary mass flow) through the ejector.
- $D_a$ ; the diameter of the outlet of the converging-diverging nozzle that the primary flow passes through.
- $D_m$  or  $D_{mix}$ ; the diameter of the constant-area section where the primary and secondary flow mix.
- $D_d$ ; the diameter of the outlet of the diffuser, the exit of the ejector.

## 4.2 Ejector Model 1

In this section, an explanation and validation of the first thermodynamic model developed for the simulation of ejector refrigeration cycles will be presented.

### 4.2.1 Modeling Procedure Model 1

Ejector model 1 is developed based on the 2016 work of Ma et al. [44]. To aid in the understanding of the equations and different parts of the ejector referred to in the first model, the schematic diagram of the ejector used by Ma et al. is included in figure 4.1.

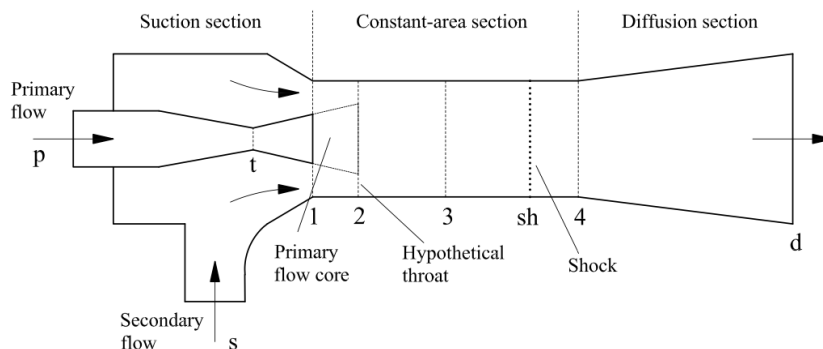


Figure 4.1: Schematic drawing of ejector by Ma et al. [44].

In the model, the following is assumed:

- The flow is adiabatic.
- The kinetic energy at both inlets (primary and secondary flow) is negligible.
- Flow friction is captured by isentropic efficiencies.
- Losses during momentum transfer are represented by a mixing loss factor.
- A pre-defined entrainment ratio is available.

In ejector model 1, the primary flow in the ejector is assumed not to mix with the secondary flow and instead fan out from the nozzle in a certain downstream distance. This leads to the formation of a 'hypothetical throat' at the distance where the secondary flow reaches the local speed of sound (cross section 2 in figure 4.1). In line with the aforementioned assumptions, the expansion process of the primary flow in the converging-diverging nozzle of the primary flow is non-isentropic, with an isentropic efficiency  $\eta_p$ , defined as:

$$\eta_p = \frac{h_p - h_t}{h_p - h_{t,is}} \quad (4.1)$$

$$\eta_p = \frac{h_t - h_a}{h_t - h_{a,is}} \quad (4.2)$$

where  $h_{t,is}$  is the enthalpy for an isentropic compression. This can be obtained using the present pressure and the past entropy:

$$h_{t,is} = f_{REFPROP}(P_t, s_p) \quad (4.3)$$

Similarly,  $h_{a,is}$  is the enthalpy for isentropic expansion. This can be obtained via equation 4.4:

$$h_{a,is} = f_{REFPROP}(P_a, s_t) \quad (4.4)$$

By applying energy conservation to the nozzle section, the following equations can be obtained.

$$h_p = h_t + \frac{u_t^2}{2} \quad (4.5)$$

$$h_t + \frac{u_t^2}{2} = h_a + \frac{u_a^2}{2} \quad (4.6)$$

where  $u_t$  and  $u_a$  are the primary flow velocities at the throat (equal to the local speed of sound) and outlet of the nozzle, respectively.

The local speed of sound and density of the flow in the throat can be determined using equations 4.7 and 4.8:

$$u_t = f_{REFPROP}(P_t, h_t) \quad (4.7)$$

$$\rho_t = f_{REFPROP}(P_t, h_t) \quad (4.8)$$

With the flow velocity and density in the throat established, the mass flow can be derived:

$$\dot{m}_p = \dot{m}_t = \rho_t A_t u_t \quad (4.9)$$

The flow velocity at the outlet of the nozzle,  $u_a$  can then be obtained by a mass balance equation:

$$u_a = \frac{\dot{m}_p}{A_a \cdot \rho_a} \quad (4.10)$$

As stated earlier, the model assumes the formation of a 'hypothetical throat' which according to the hypothesis Munday & Bagster [79] is where the secondary flow reaches the local speed of sound.

The secondary or suction flow and its nozzle efficiency is governed by equations similar to the primary nozzle:

$$\eta_s = \frac{h_s - h_{s2}}{h_s - h_{s,is}} \quad (4.11)$$

The primary flow core is modeled as an extended expansion at the outlet of the diverging nozzle section. This results in equations similar to equations 4.1, 4.2 and 4.11:

$$\eta_n = \frac{h_a - h_{p2}}{h_a - h_{p2,is}} \quad (4.12)$$

The model assumes no mixing of the primary and secondary fluid before the choke of the secondary flow. There is however energy transfer between the two flows. The secondary mass flow follows from the imposed entrainment ratio  $\gamma$ :

$$\dot{m}_s = \gamma \cdot \dot{m}_p \quad (4.13)$$

With the secondary mass flow established, the hypothetical throat area  $A_{s2}$  can be calculated with the velocity and density of the secondary flow at section 2:

$$A_{s2} = \frac{\dot{m}_s}{u_{s2} \cdot \rho_{s2}} \quad (4.14)$$

where  $u_{s2}$  and  $\rho_{s2}$  follow from equations similar to equations 4.7 and 4.8, respectively. In the case of two phase flow, a 1981 relation by Nguyen et al. [80] is used to calculate the speed of sound of the secondary flow in cross section 2, this empirical relation is detailed in section 4.4.1.

$$A_{s2} = \frac{\dot{m}_s}{u_{s2} \cdot \rho_{s2}} \quad (4.15)$$

With  $A_{s2}$ , established, the primary flow core area  $A_{p2}$  can be calculated from the geometry of the ejector:

$$A_{p2} = A_2 - A_{s2} \quad (4.16)$$

With  $A_{p2}$ , determined, the flow velocity of the primary flow in section 2  $u_{p2}$  can be calculated:

$$u_{p2} = \frac{\dot{m}_p}{A_{p2} \cdot \rho_{p2}} \quad (4.17)$$

where  $\rho_{p2}$  is a function of the enthalpy  $h_{p2}$  and pressure  $P_{p2} = P_{s2} = P_2$ . The energy balance can then be shown to be:

$$\dot{m}_p \left( h_a + \frac{u_a^2}{2} \right) + \dot{m}_s h_s = \dot{m}_p \left( h_{p2} + \frac{u_{p2}^2}{2} \right) + \dot{m}_s \left( h_{s2} + \frac{u_{s2}^2}{2} \right) \quad (4.18)$$

To describe the mixing process in sections 2 and 3, a mass balance equation, energy balance equation, momentum balance equation and a thermodynamic state equation are used:

$$\rho_3 u_3 A_3 = \dot{m}_p + \dot{m}_s = \dot{m}_3 \quad (4.19)$$

$$\dot{m}_p \left( h_{p2} + \frac{u_{p2}^2}{2} \right) + \dot{m}_s \left( h_{s2} + \frac{u_{s2}^2}{2} \right) = \dot{m}_3 \left( h_3 + \frac{u_3^2}{2} \right) \quad (4.20)$$

$$\eta_{mix} (\dot{m}_p u_{p2} + \dot{m}_s u_{s2}) + P_{p2} A_{p2} + P_{s2} A_{s2} = \dot{m}_3 u_3 + P_3 A_3 \quad (4.21)$$

$$\rho_3 = f(P_3, h_3) \quad (4.22)$$

where  $\eta_{mix}$  is the mixing efficiency.

The normal shock that takes place in the constant area section (1-4 in figure 4.1). The normal shock causes a pressure increase and velocity decrease. This process can not be considered isentropic. Instead, similar to the modeling of the mixing process, equations for conservation of mass, energy and momentum are applied together with a state equation for the density:

$$\rho_3 u_3 = \rho_4 u_4 = \frac{\dot{m}_3}{A_3} \quad (4.23)$$

$$h_3 + \frac{u_3^2}{2} = h_4 + \frac{u_4^2}{2} \quad (4.24)$$

$$P_3 A_3 + \dot{m}_3 u_3 = P_4 A_3 + \dot{m}_3 u_4 \quad (4.25)$$

$$\rho_4 = \rho(P_4, h_4) \quad (4.26)$$

The working fluid is decelerated to subsonic speed after the shock in the diffuser. During the divergence, the pressure increases and the velocity decreases. The energy balance in the diffuser is as follows:

$$h_d + \frac{u_d^2}{2} = h_4 + \frac{u_4^2}{2} \quad (4.27)$$

where as stated earlier, losses are governed by a predefined diffuser efficiency  $\eta_d$ :

$$\eta_d = \frac{h_{d,is} - h_4}{h_d - h_4} \quad (4.28)$$

If the working fluid can be decelerated to stagnant, the most pressure is recovered. In most real cases however, the outlet velocity  $u_d$  cannot be considered to be 0 and the following mass balance equation must be satisfied:

$$\dot{m}_d = \dot{m}_3 = \rho_d u_d A_d \quad (4.29)$$

In ejector model 1, simulation is done in the following steps:

1. Input of ejector geometric parameters; inlet pressures and temperatures.
2. Assuming value for  $P_t$  at nozzle throat. Determination of local sound speed via  $P_t$  and calculated enthalpy  $h_t$ . Iterative process until assumption  $P_t$  results in a  $u_t$  equal to the local sound speed. Primary mass flow  $\dot{m}_p$  calculated with density and given throat area.
3. Calculation of  $u_a$  via both energy balance (with an assumed  $P_a$ ) and mass balance equations. Iterative process to find  $P_a$  which leads to a sufficiently small difference between the two motive nozzle outlet velocities obtained by the two different calculation methods.
4. Assuming value for  $P_2$ , calculating the isentropic enthalpy at section 2 and using it to calculate the isentropic enthalpy in section 2. The real enthalpy is then calculated through the use of a predefined isentropic secondary efficiency. The experimental entrainment ratio can then be used to determine the mass flow rate of the secondary flow, which is in turn used to calculate the hypothetical throat area. With a known mixing area, flow velocity can be calculated for the primary flow in section 2. Then, an iterative process is started to find a  $P_2$  to satisfy equation 4.18.
5. Assuming value for  $P_3$ , calculating the flow velocity via equation 4.21, where enthalpy and density follow from equation 4.20 and 4.22, respectively. The pressure is then adjusted iteratively to satisfy mass balance equation 4.19.
6. Solving shock wave equations 4.23 through 4.26, calculations procedure same as step 5.
7. In on-design conditions, in other words if the designed working conditions are satisfied, the exit velocity  $u_d$  can be considered to be 0. With this, the diffuser enthalpy can be calculated and so the diffuser pressure  $P_d$  can be calculated through the isentropic enthalpy and entropy in section 4.
8. In off-design conditions, the diffuser outlet area is required for subsequent calculations. With the diffuser outlet area, the exit velocity  $u_d$  should be assumed, to start an iterative process to achieve mass conservation in equation 4.29.

An explanation on the iterative process used in the model can be read in section 4.4.2. It should be noted that in order for the simulation to work, input of the experimental critical entrainment ratio was required in step 4 (equation 4.13).

## 4.2.2 Validation Model 1

In this subsection, model 1 will be validated by comparing its diffuser outlet conditions calculation to experimental studies. The partial efficiencies used in model 1 of the ejector are  $\eta_p = 0.95$ ,  $\eta_s = 0.85$ ,  $\eta_{mix} = 0.95$  and  $\eta_d = 0.85$ .

### Diffuser Outlet Conditions

The results presented in table 4.1 provide a comparative validation of model 1 ( $m_1$ ) against experimental data from Garcia del Valle et al. [81]. The table includes key parameters such as throat diameter ( $D_t$ ), primary nozzle exit diameter ( $D_a$ ), mixing area diameter ( $D_{mix}$ ), diffuser outlet diameter ( $D_d$ ), and the experimental ( $T_{d,sat,exp}$ ) and modeled ( $T_{d,sat,m1}$ ) saturation temperatures. The error ( $T_{d,sat,m1} - T_{d,sat,exp}$ ) quantifies the absolute deviation between the modeled results and experimental measurements.

$D_t$ (mm)	$D_a$ (mm)	$D_{mix}$ (mm)	$D_d$ (mm)	$T_p$ ( $^{\circ}C$ )	$T_s$ ( $^{\circ}C$ )	$\gamma$	$T_{d,sat,exp}$ ( $^{\circ}C$ )	$T_{d,sat,m1}$ ( $^{\circ}C$ )	Error ( $^{\circ}C$ )
2	3	4.8	10	89.37	17	0.422	28.95	28.15	-0.8
2	3	4.8	10	89.37	20	0.494	29.41	29.03	-0.38
2	3	4.8	10	94.39	17	0.342	31.68	30.93	-0.75
2	3	4.8	10	94.39	20	0.398	32.48	31.68	-0.80
2	3	4.8	10	99.15	15	0.273	32.02	33.59	1.57
2	3	4.8	10	99.15	17	0.297	34.11	33.91	-0.20
2	3	4.8	10	99.15	20	0.339	35.41	34.52	-0.89

Table 4.1: Comparison model 1 to 2014 experiments by Garcia del Valle et al. [81].

In table 4.2, a comparative validation of model 1 against experimental data by Jia and Wenjian [82] can be seen, indicating large absolute errors in the prediction of the diffuser outlet conditions. This could be because of the missing diffuser outlet diameter ( $D_d$ ) which is estimated based on the 3 available diameters.

$D_t$ (mm)	$D_a$ (mm)	$D_{mix}$ (mm)	$D_d$ (mm)	$T_p$ ( $^{\circ}C$ )	$T_s$ ( $^{\circ}C$ )	$\gamma$	$T_{d,sat,exp}$ ( $^{\circ}C$ )	$T_{d,sat,m1}$ ( $^{\circ}C$ )	Error ( $^{\circ}C$ )
2.5	4.1	4.8	-	68.57	12.00	0.276	33.05	6.953	-26.10
2.5	4.1	4.8	-	68.57	10.00	0.220	33.05	6.290	-26.76
2.5	4.1	4.8	-	68.57	8.03	0.140	33.05	5.367	-27.68
2.5	4.1	5.1	-	74.73	12.00	0.302	31.76	10.54	-21.22
2.5	4.1	5.1	-	74.73	10.00	0.254	31.76	9.972	-21.79
2.5	4.1	5.1	-	74.73	8.03	0.172	31.76	9.054	-22.71
2.2	3.8	4.8	-	77.58	12.00	0.403	30.00	11.19	-18.81
2.2	3.8	4.8	-	77.58	10.00	0.318	30.00	10.26	-19.74
2.2	3.8	4.8	-	77.58	8.03	0.215	30.00	9.149	-20.85

Table 4.2: Comparison model 1 to 2012 experiments by Jia and Wenjian [82].

## Evaluation Model 1

The evaluation of the first ejector model demonstrates that it achieves a usable level of accuracy, provided that all input parameters are available. This model requires only a minimal set of measurable input parameters, which makes it simple to implement across various operational cycles and configurations. Its adaptability and ease of use make it suitable for a wide range of applications. However, despite these advantages, the first model has a notable limitation. Specifically, it requires the entrainment ratio to be predefined, which is not practical in many real-world scenarios where this parameter cannot be easily measured or determined in advance. The dependency on a known entrainment ratio restricts the model's flexibility and limits its applicability since entrainment ratio is affected by operational conditions. To summarize, model 1 does not meet the requirements presented in section 4.1, to address this limitation and increase overall modeling accuracy, a second thermodynamic ejector model will be developed with the primary goal of predicting the entrainment ratio.

## 4.3 Ejector Model 2

In this section, an explanation and validation of the second thermodynamic model developed for the modeling of ejector refrigeration cycles will be presented. This new model aims to overcome the constraints of the first model, providing a more adaptable and comprehensive tool for the subsequent ejector refrigeration cycle analysis.

### 4.3.1 Modeling Procedure Model 2

As mentioned before, the second ejector model is designed with the aim of incorporating entrainment ratio prediction, ejector model 2 is developed based on the 2024 work of Mastrowski et al. [45].

In the second ejector model, the following is assumed:

- The flow along the ejector is steady and adiabatic.
- The primary (motive) and secondary (suction) inlet velocities are equal to 0.
- The boundary conditions of the model are formed by the pressure and enthalpy at the inlet and the pressure at the outlet.
- Primary and secondary fluid mix under constant pressure.
- The frictional factor throughout the mixing chamber is constant.
- The flow in the mixing chamber is considered to be Fanno flow [83].

The model uses real gas properties for its calculations. Like the first model, the second model starts with an iterative calculation of the primary nozzle throat pressure to obtain the pressure where the primary fluid reached the local speed of sound in the throat. The velocity of the fluid in the throat is then calculated from the energy conservation equation:

$$u_t = \sqrt{2 \cdot (h_p - h_t) + u_{in}^2} \quad (4.30)$$

where  $u_{in}$  is equal to zero according to the assumptions. With the velocity in the throat established, the primary or motive mass flow is calculated:

$$\dot{m}_p = A_t \cdot u_t \cdot \rho_t \quad (4.31)$$

where  $A_t$  and  $\rho_t$  are the area of and the density in the throat, respectively. To calculate the parameters at the primary nozzle outlet, the model assumes that the pressure at the primary nozzle outlet is equal to the inlet pressure of the secondary flow, i.e.  $P_a = P_{s2}$ . The enthalpy at the primary nozzle outlet is then equal to:

$$h_a = h_t - \eta_p \cdot (h_t - h_{a,is}) \quad (4.32)$$

After the enthalpy at the primary nozzle outlet is calculated, the velocity can be calculated by the conservation of energy equation, similar to equation 4.30. Next, the hypothetical throat cross-section is calculated. The final area of the internal flow core, in other words the last cross-section of the primary fluid before mixing is calculated by a modified mass conservation equation:

$$A_{p2} = \frac{\eta_a \cdot \dot{m}_p}{\rho_{p2} \cdot u_{p2}} \quad (4.33)$$

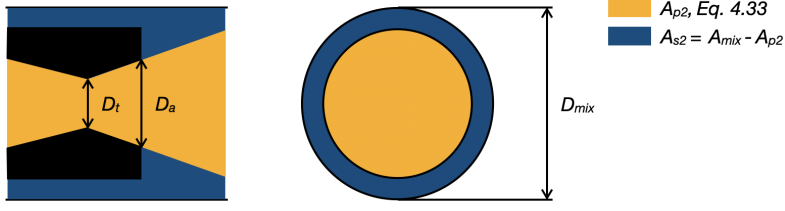


Figure 4.2: Expanding flowcore and cross section before mixing.

where  $\eta_a$  is introduced by this model as the efficiency of the expansion of the primary fluid. The area of the secondary fluid in the hypothetical throat can then be calculated by subtracting  $A_{p2}$  from the mixing area  $A_{mix}$ , similar to in equation 4.16. This is visualized in figure 4.2 where the primary and secondary fluid are depicted in yellow and blue, respectively. With  $A_{s2}$  found, the secondary mass flow is calculated analogously to the primary mass flow:

$$\dot{m}_s = A_{s2} \cdot u_{s2} \cdot \rho_{s2} \quad (4.34)$$

where  $u_{s2}$  is the velocity of the secondary fluid at the hypothetical throat, calculated similarly to the throat velocity in equation 4.30.  $\rho_{s2}$  can be calculated from the pressure and enthalpy at the throat. The enthalpy of the secondary fluid in the hypothetical throat is found in the same way as the enthalpy at the outlet of the primary nozzle (equation 4.32). The pressure at the hypothetical throat is adjusted until it results in the highest value for the secondary mass flow  $\dot{m}_s$ .

For the mixing inlet of the mixing section, the flow velocity is assumed to be a weighted average of the flow velocities of the primary and secondary flow velocities at the hypothetical throat, adjusted by the mixing efficiency:

$$u_{mix} = \eta_{mix} \cdot \frac{u_{p2} \cdot \dot{m}_p + u_{s2} \cdot \dot{m}_s}{\dot{m}_p + \dot{m}_s} \quad (4.35)$$

The enthalpy at the inlet of the mixing section can then be calculated from the energy balance equation, equation 4.20 in model 1. The mach number, temperature and pressure after mixing is calculated iteratively by the following set of equations:

$$T_{mix,out} = T_{mix,in} \cdot \frac{1 + \frac{\kappa_{mix,avg}-1}{2} \cdot M_{mix,in}^2}{1 + \frac{\kappa_{mix,avg}-1}{2} \cdot M_{mix,out}^2} \quad (4.36)$$

$$p_{mix,out} = p_{mix,in} \cdot \frac{M_{mix,in}}{M_{mix,out}} \cdot \sqrt{\frac{1 + \frac{\kappa_{mix,avg}-1}{2} \cdot M_{mix,in}^2}{1 + \frac{\kappa_{mix,avg}-1}{2} \cdot M_{mix,out}^2}} \quad (4.37)$$

$$\begin{aligned} \frac{f_m \cdot l_{mix}}{d_{mix}} &= \frac{\kappa_{mix,avg} + 1}{2 \cdot \kappa_{mix,avg}} \cdot \ln \left( \frac{1 + \frac{\kappa_{mix,avg}-1}{2} \cdot M_{mix,out}^2}{1 + \frac{\kappa_{mix,avg}-1}{2} \cdot M_{mix,in}^2} \right) \\ - \frac{1}{\kappa_{mix,avg}} \left( \frac{1}{M_{mix,out}^2} - \frac{1}{M_{mix,in}^2} \right) &- \frac{\kappa_{mix,avg} + 1}{2 \cdot \kappa_{mix,avg}} \cdot \ln \left( \frac{M_{mix,out}^2}{M_{mix,in}^2} \right) \end{aligned} \quad (4.38)$$

where  $f_m$  is related to the Reynolds number of the local flow and numerically found through Schlichting equation [84]:

$$\frac{1}{\sqrt{f_m}} = 2 \cdot \log \left( Re_{mix} \cdot \sqrt{f_m} \right) - 0.8 \quad (4.39)$$

where the Reynolds number for the mixing  $Re_{mix}$  section is calculated using the following relation:

$$Re_{mix} = \frac{u_{mix} \cdot D_{mix} \cdot \rho_{mix}}{\mu_{mix}} \quad (4.40)$$

For the inlet of the diffuser, a new state point in the model is introduced. A set of mach number relations that can be found in books like *Fluid Mechanics: Fundamentals and Applications* by Çingel and Cimbala [85] are used for the calculation of the temperature, pressure and mach number at the inlet of the diffuser:

$$\frac{T_{d,in}}{T_{mix}} = (2 + M_{mix}^2 \cdot (k_{mix} - 1)) \cdot \frac{2 \cdot k_{mix} \cdot M_{mix}^2 - (k_{mix} - 1)}{M_{mix}^2 \cdot (k_{mix} + 1)^2} \quad (4.41)$$

$$\frac{P_{d,in}}{P_{mix}} = \frac{1}{k_{mix} + 1} \cdot (2 \cdot k_{mix} \cdot M_{mix}^2 - (k_{mix} - 1)) \quad (4.42)$$

$$M_{d,in} = \sqrt{\frac{2 + M_{mix}^2 \cdot (k_{mix,d} - 1)}{2 \cdot k_{mix} \cdot M_{mix}^2 - (k_{mix,d} - 1)}} \quad (4.43)$$

For the diffuser and thus ejector outlet, the temperature and pressure are calculated based on the mach number and ratio of specific heat:

$$\frac{T_d}{T_{d,in}} = \eta_d \cdot \left( 1 + \frac{k_{dif} - 1}{2} \cdot M_{d,in}^2 \right) \quad (4.44)$$

$$\frac{P_d}{P_{d,in}} = \eta_d \cdot \left( 1 + \frac{k_{dif} - 1}{2} \cdot M_{d,in}^2 \right)^{\frac{k_d}{k_d - 1}} \quad (4.45)$$

The outlet pressure  $P_d$  is then compared to the predefined outlet pressure (the condenser pressure in a standard ejector refrigeration cycle). If  $P_d < P_{cond}$  backflow would occur. To prevent this, the hypothetical throat pressure  $P_{hypth}$  is increased until  $P_d > P_{cond}$ . Herein  $P_{hypth}$  is limited by  $P_s$ , since a hypothetical throat pressure larger than the secondary pressure (i.e.  $P_{hypth} > P_s$ ) would cause backflow in the secondary inlet. The mixing efficiency is then adjusted according to a modified equation proposed by Chen et al. [86]:

$$\eta_{mix(n)} = \eta_{mix(n-1)} \cdot \left( 1 - 1.1 \cdot \frac{P_{cond} - P_{d(n-1)}}{P_{d(n-1)}} \right) \quad (4.46)$$

Figure 4.3 presents a flowchart representing the calculation procedure in model 2. The Matlab script for model 2 can be seen in appendix C.

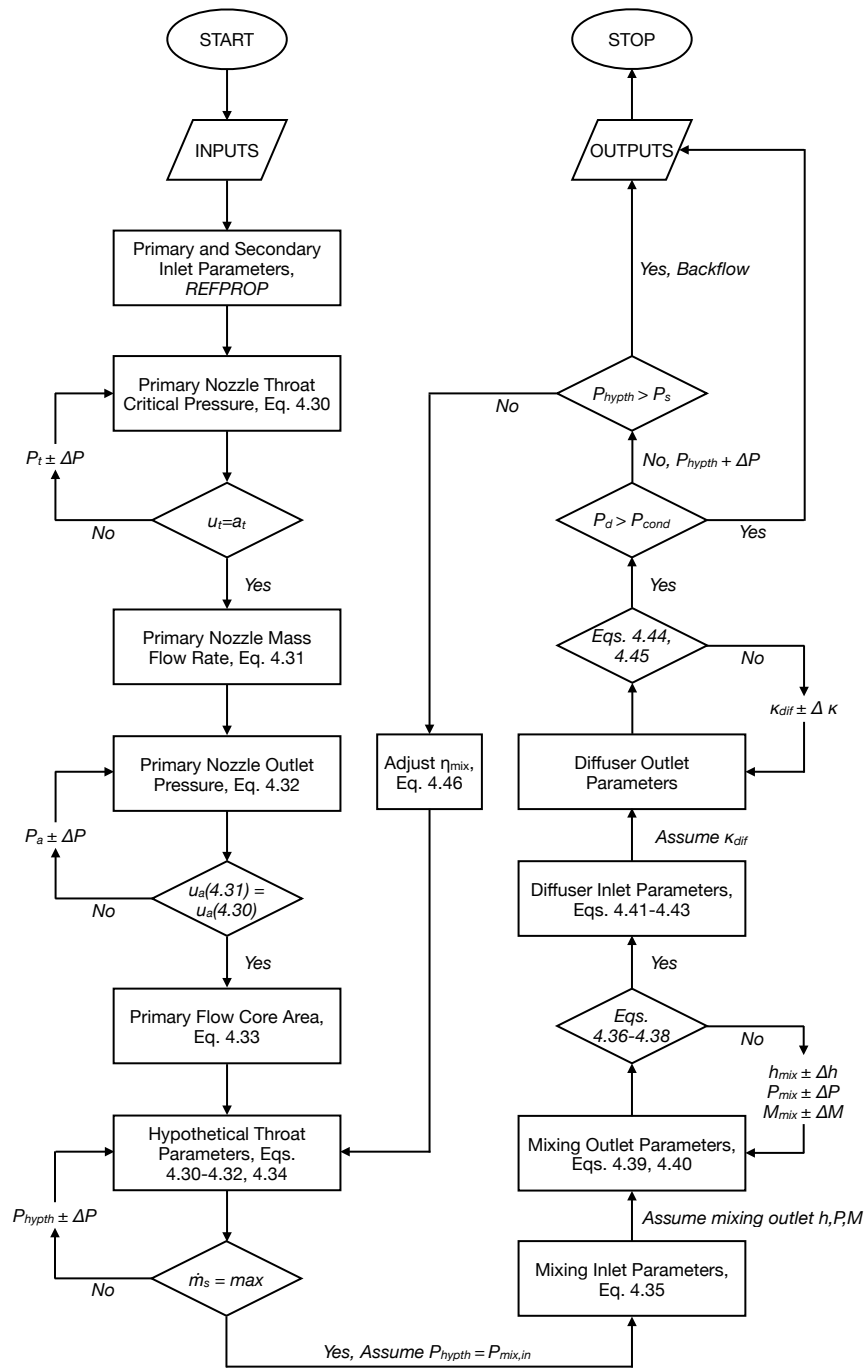


Figure 4.3: Ejector model 2 flowchart.

### 4.3.2 Ejector Model 2 Validation

In this subsection, model 2 will be validated by comparing its diffuser outlet conditions and entrainment ratio prediction to experimental studies. The partial efficiencies used in model 2 of the ejector are  $\eta_p = 0.97$ ,  $\eta_a = 0.93$ ,  $\eta_s = 0.45$ ,  $\eta_{mix} = 0.93$  and  $\eta_d = 0.92$ .

#### Diffuser Outlet Conditions

The results presented in table 4.3 provide a comparative validation of model 2 ( $m_2$ ) against experimental data from Garcia del Valle et al. [81]. The table includes key parameters such as throat diameter ( $D_t$ ), primary nozzle outlet diameter ( $D_a$ ), mixing area diameter ( $D_{mix}$ ), diffuser outlet diameter ( $D_d$ ), and the experimental ( $T_{d,sat,exp}$ ) and modeled ( $T_{d,sat,m2}$ ) saturation temperatures. The error ( $T_{d,sat,m2} - T_{d,sat,exp}$ ) quantifies the deviation between the modeled results and experimental measurements. Across the evaluated cases, the error ranges from  $-0.46^\circ\text{C}$  to  $1.05^\circ\text{C}$  for all entries, indicating agreement between model 2 and experimental data. The overall trends demonstrate that model 2 can predict outlet flow saturation temperatures well under the specified conditions. These results support the applicability of model 2 in representing the performance of an ejector.

$D_t$ (mm)	$D_a$ (mm)	$D_{mix}$ (mm)	$D_d$ (mm)	$T_p$ ( $^\circ\text{C}$ )	$T_s$ ( $^\circ\text{C}$ )	$T_{d,sat,exp}$ ( $^\circ\text{C}$ )	$T_{d,sat,m2}$ ( $^\circ\text{C}$ )	Error ( $^\circ\text{C}$ )
2	3	4.8	10	89.37	17	28.95	28.63	-0.31
2	3	4.8	10	89.37	20	29.41	29.21	-0.20
2	3	4.8	10	94.39	17	31.68	31.42	-0.46
2	3	4.8	10	94.39	20	32.48	32.14	-0.34
2	3	4.8	10	99.15	15	32.02	33.07	1.05
2	3	4.8	10	99.15	17	34.11	33.93	-0.18
2	3	4.8	10	99.15	20	35.41	34.73	-0.68

Table 4.3: Comparison model 2 to 2014 experiments by Garcia del Valle et al. [81].

Building on the validation of Model 2 ( $m_2$ ) against Garcia del Valle et al. [81], table 4.4 presents a comparison with experimental data from Jia and Wenjian [82]. In this dataset, errors range from  $-2.56^\circ\text{C}$  to  $2.22^\circ\text{C}$ , demonstrating that model 2 performs consistently within an acceptable margin of deviation from experimental measurements. Notably, positive errors dominate in cases with higher outlet pressures, whereas negative errors occur in cases with lower pressures. This trend suggests a potential sensitivity of model 2 to pressure variations, which aligns with observations from the previous validation. Combined with the earlier results, this comparison strengthens the case for model 2's applicability across diverse experimental datasets. It should be noted that compared to model 1, model 2 shows improved accuracy predicting the outlet conditions of the experiments by Jia and Wenjian [82], which could be attributed to the fact that model 2 does not require a known diffuser outlet diameter ( $D_d$ ).

$D_t$ (mm)	$D_a$ (mm)	$D_{mix}$ (mm)	$D_d$ (mm)	$T_p$ ( $^{\circ}C$ )	$T_s$ ( $^{\circ}C$ )	$T_{d,sat,exp}$ ( $^{\circ}C$ )	$T_{d,sat,m2}$ ( $^{\circ}C$ )	Error ( $^{\circ}C$ )
2.5	4.1	4.8	-	68.57	12.00	33.05	31.40	-1.65
2.5	4.1	4.8	-	68.57	10.00	33.05	30.80	-2.25
2.5	4.1	4.8	-	68.57	8.03	33.05	30.49	-2.56
2.5	4.1	5.1	-	74.73	12.00	31.76	33.21	1.45
2.5	4.1	5.1	-	74.73	10.00	31.76	32.56	0.80
2.5	4.1	5.1	-	74.73	8.03	31.76	32.27	0.51
2.2	3.8	4.8	-	77.58	12.00	30.00	32.22	2.22
2.2	3.8	4.8	-	77.58	10.00	30.00	31.93	1.93
2.2	3.8	4.8	-	77.58	8.03	30.00	31.30	1.30

Table 4.4: Comparison model 2 to 2012 experiments by Jia and Wenjian [82].

### Entrainment Ratio Prediction

As explained in section 3.1.2, the entrainment ratio is an important figure for the performance of an ejector. table 4.5 presents the validation of model 2 ( $m_2$ ) for predicting the entrainment ratio ( $\gamma$ ) against experimental data from Garcia del Valle et al. [81]. the experimental entrainment ratio ( $\gamma_{exp}$ ) and the modeled values ( $\gamma_{m2}$ ) are compared, with the relative error calculated as  $(\gamma_{m2} - \gamma_{exp})/\gamma_{exp} \cdot 100$ . Across the cases, errors range from  $-24.62\%$  to  $-30.77\%$ , indicating a consistent underprediction of entrainment by model 2.

$D_t$ (mm)	$D_a$ (mm)	$D_{mix}$ (mm)	$D_d$ (mm)	$T_p$ ( $^{\circ}C$ )	$T_s$ ( $^{\circ}C$ )	$\gamma_{exp}$	$\gamma_{m2}$	Error (%)
2.0	3.0	4.8	10.0	89.37	17.0	0.422	0.307	-27.25
2.0	3.0	4.8	10.0	89.37	20.0	0.494	0.356	-27.94
2.0	3.0	4.8	10.0	94.39	17.0	0.342	0.256	-25.15
2.0	3.0	4.8	10.0	94.39	20.0	0.398	0.300	-24.62
2.0	3.0	4.8	10.0	99.15	15.0	0.273	0.189	-30.77
2.0	3.0	4.8	10.0	99.15	17.0	0.297	0.213	-28.28
2.0	3.0	4.8	10.0	99.15	20.0	0.339	0.252	-25.66

Table 4.5: Comparison entrainment prediction Model 2 to 2014 experiments by Garcia del Valle et al. [81].

Following the entrainment ratio validation for the Garcia del Valle et al. dataset, table 4.6 compares model 2 predictions to the experimental data from Jia and Wenjian [82]. The results exhibit a broader range of errors compared to the Garcia del Valle dataset, spanning from  $-45.45\%$  to  $16.28\%$ . At lower pressures, the model predominantly underpredicts the entrainment ratio, with the largest error observed at  $T_p = 68.57^{\circ}C$  and  $T_s = 10.00^{\circ}C$ . Conversely, slight overpredictions occur in specific cases at higher pressures, such as  $T_p = 74.73^{\circ}C$  and  $T_s = 8.03^{\circ}C$ .

$D_t$ (mm)	$D_a$ (mm)	$D_{mix}$ (mm)	$D_d$ (mm)	$T_p$ ( $^{\circ}C$ )	$T_s$ ( $^{\circ}C$ )	$\gamma_{exp}$	$\gamma_{m2}$	Error (%)
2.5	4.1	4.8	-	68.57	12.00	0.276	0.178	-35.51
2.5	4.1	4.8	-	68.57	10.00	0.220	0.120	-45.45
2.5	4.1	4.8	-	68.57	8.03	0.140	0.080	-42.86
2.5	4.1	5.1	-	74.73	12.00	0.302	0.251	-16.89
2.5	4.1	5.1	-	74.73	10.00	0.254	0.224	-11.81
2.5	4.1	5.1	-	74.73	8.03	0.172	0.200	16.28
2.2	3.8	4.8	-	77.58	12.00	0.403	0.289	-28.29
2.2	3.8	4.8	-	77.58	10.00	0.318	0.260	-18.24
2.2	3.8	4.8	-	77.58	8.03	0.215	0.233	8.37

Table 4.6: Comparison entrainment prediction model 2 to 2012 experiments by Jia and Wenjian. [82].

For the specific case of ejector refrigeration cycles, the effect of outlet conditions on the entrainment ratio in the ejector are critically important as explained in sections 3.1.2 and 3.4.2. The results in table 4.7 summarize the performance of model 2 in predicting the entrainment ratio ( $\gamma$ ) for ejector refrigeration cycles under fixed outlet (condenser) saturation temperatures. The table compares experimental data from Mastrowski et al. [45] with the corresponding predictions of model 2. The errors between the experimental and modeled entrainment ratios are provided in percentage terms. Overall, the model demonstrates consistent accuracy in the critical operation region, with minimal deviation from the experimental results at lower outlet temperatures.

$D_t$ (mm)	$D_a$ (mm)	$D_{mix}$ (mm)	$D_d$ (mm)	$T_p$ ( $^{\circ}C$ )	$T_s$ ( $^{\circ}C$ )	$T_{cond}$ ( $^{\circ}C$ )	$\gamma_{exp}$	$\gamma_{m2}$	Error (%)
27.9	42	53.55	178	70.00	19.30	23.00	0.2400	0.2406	0.25
27.9	42	53.55	178	70.00	19.30	23.20	0.2400	0.2406	0.25
27.9	42	53.55	178	70.00	19.30	24.00	0.2400	0.2406	0.25
27.9	42	53.55	178	70.00	19.30	24.50	0.2400	0.2406	0.25
27.9	42	53.55	178	70.00	19.30	25.20	0.2280	0.2406	5.53
27.9	42	53.55	178	70.00	19.30	26.40	0.2100	0.2300	9.52
27.9	42	53.55	178	70.00	19.30	27.65	0.1640	0.1946	18.66
27.9	42	53.55	178	70.00	19.30	28.20	0.1240	0.1200	-3.23
27.9	42	53.55	178	70.00	19.30	30.10	0.0720	0.0635	-11.81
27.9	42	53.55	178	70.00	19.30	31.00	0.0340	0.0000	-100.00

Table 4.7: Comparison Entrainment Prediction Model 2 to 2024 Experiments by Mastrowski et al. [45].

As the outlet saturation temperature increases, the model exhibits a noticeable shift in predictive performance. For example, errors increase in the subcritical region, particularly near the transition point at  $T_s = 27.65^{\circ}C$ , where the deviation reaches 18.66%. This indicates that while the model captures the general trends in entrainment behavior, predictive accuracy in the transitional zones is reduced. Beyond the critical region, the model diverges, as evidenced by the increased error values. The failure to predict entrainment at the highest temperature ( $T_s = 31.00^{\circ}C$ ) indicates a slightly over predicted negative relation between increased outlet pressures and entrainment ratio.

Figure 4.4 illustrates the comparison between experimental and modeled entrainment ratios across the fixed outlet (condenser) temperature range. The horizontal plateau at lower temperatures corresponds to the critical operation region, where entrainment remains stable and the system operates efficiently. The subsequent decline represents the subcritical operation region, characterized by a gradual reduction in entrainment as the outlet pressure increases. Finally, the failure region is marked by a steep decline, indicating that the ejector fails to sustain secondary flow at these conditions.

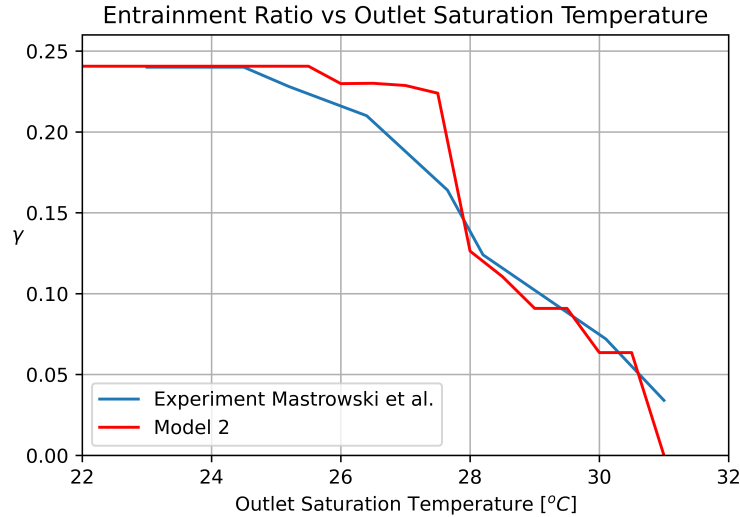


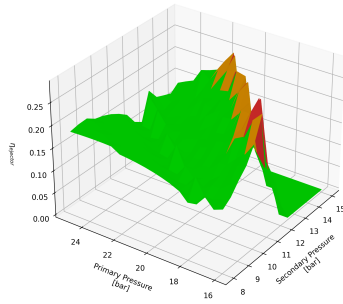
Figure 4.4: Entrainment ratio prediction model 2 versus outlet saturation temperature.

The overall ejector efficiency, defined in equation 3.1 in section 3.2.1 that is put out by the second thermodynamic ejector model is analyzed in section 4.3.3.

### 4.3.3 Efficiency Analysis Ejector Model 2

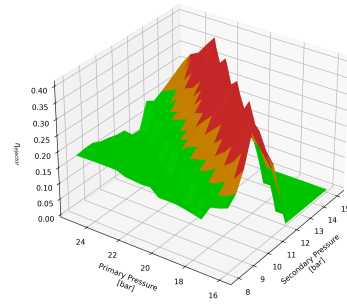
As stated in the parameter identification in section 4.1.1, the overall efficiency of the ejector  $\eta_{ejector}$  can be used to verify realistic output by the ejector model. In figure 4.5, surface plots of  $\eta_{ejector}$  as a function of the primary and secondary pressure can be seen. The primary pressure on the y-axis varies between 16 and 25 bar, while the secondary pressure on the x-axis varies between 8 and 15 bar. The four graphs present the value of  $\eta_{ejector}$  for four different values of pressure lift ( $P_d - P_s$ ). Values below 0.2 are indicated by a green color, values between 0.2 and 0.25 are displayed in orange and values above 0.25 are shown in red. It can be seen that if the primary and secondary pressure get too close, unrealistically high overall efficiencies are put out by the thermodynamic model before the ejector fails, indicated by an ejector efficiency of zero in the rightmost corner of each surface graph. This is especially pronounced at a pressure lift ( $P_d - P_s$ ) of 2 and 3 bar (figures 4.5b and 4.5c). Dynamic primary pressure limits are integrated into the second ejector model to ensure realistic ejector performance output.

$\eta_{ejector}$  vs  $P_s$  and  $P_p$  for 1 bar of Pressure Lift



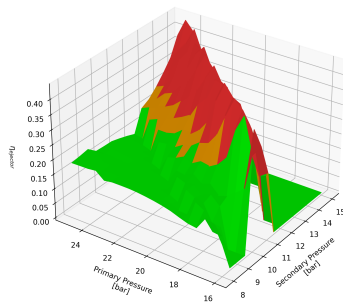
(a) 1 bar

$\eta_{ejector}$  vs  $P_s$  and  $P_p$  for 2 bar of Pressure Lift



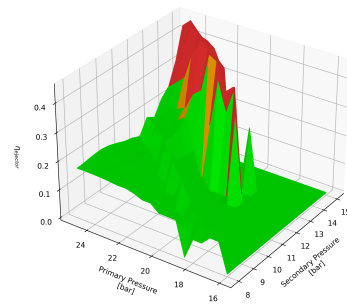
(b) 2 bar

$\eta_{ejector}$  vs  $P_s$  and  $P_p$  for 3 bar of Pressure Lift



(c) 3 bar

$\eta_{ejector}$  vs  $P_s$  and  $P_p$  for 4 bar of Pressure Lift



(d) 4 bar

Figure 4.5:  $\eta_{ejector}$  vs  $P_s$  and  $P_p$  for different pressure lifts.

The similarity in shape between the experimental and modeled curves, and expected curve shape introduced in figure 3.2 indicates the ability of model 2 to replicate the characteristic operational modes of the ejector within the limit introduced by the difference between the primary and secondary inlet pressure. In this research, model 2 is therefore used to conduct further simulations.

## 4.4 Modeling Methods

In this section a short explanation of certain general approaches and modeling techniques in the modeling of the ejector can be read.

### 4.4.1 Speed of Sound in Two-Phase Flow

As mentioned before, the local speed of sound in both models is obtained from NIST Refprop [87]. Since Refprop does not allow the calculation of local speed of sound in two-phase flow, another method of obtaining the speed of sound is needed in case of liquid-vapor two-phase flow inside the ejector. In this research, a 1981 relation presented by Nguyen et al. [80] is used. This relates the speed of sound to the volume fractions, densities and speeds of sound of both the liquid and vapor phase in the flow. The relation essentially models the interface of one phase as an elastic wall of the other phase. The relation by Nguyen et al. is experimentally verified for both high (cavitation flow) and low (condensing flow) vapor volume fractions.

$$u_{sonic,2-phase} = \frac{1}{(1-\alpha)\sqrt{\frac{1-\alpha}{u_l^2} + \frac{\alpha\rho_l}{\rho_v u_v^2}} + \alpha\sqrt{\frac{\alpha}{u_v^2} + \frac{(1-\alpha)\rho_v}{\rho_l u_l^2}}} \quad (4.47)$$

In figure 4.6 the experimental validation of the relation for single-component systems to 1971 experiments by Henry et al. [88] can be seen, showing good agreement.

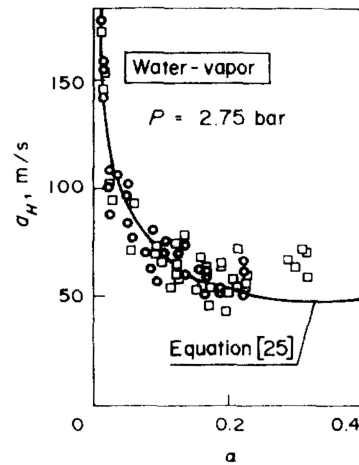


Figure 4.6: Experimental validation of relation by Nguyen et al. [80].

#### 4.4.2 Iterating procedure

To determine the pressure in each section of the ejector, an iterative procedure is needed as described earlier. For the iteration in the thermodynamic ejector model, the bisection method is used. The bisection method is based on the intermediate value theorem. The intermediate value theorem states that if  $f(x)$  is a continuous function between  $a$  and  $b$  and  $f(a)$  and  $f(b)$  are real and of opposite sign, there must be a  $c$  for which  $f(c) = 0$  that lies between  $a$  and  $b$ . The bisection method uses this theorem iteratively to find roots. In the case of the ejector model the pressure or velocity for which the mass, momentum and energy balances correspond. First, an upper and lower bound for the factor that adjusts the pressure from one section to the next is set. The midpoint between these bounds forms the next lower or upper bound based on the difference in the mass, momentum or energy equation that needs to be balanced. The adjustment of the lower or upper bound halves the interval each iteration, until the midpoint is a root of the system of equations [89]. A visual representation of the bisection method can be seen in figure 4.7, where the initial and adjusted bounds  $a$  and  $b$  are represented by the blue and green/orange dots, respectively to arrive at the root represented by the red dot. The advantages of the bisection method are its simplicity and the fact that convergence and the error in the solution are guaranteed. Disadvantages of the bisection method are the relatively slow convergence rate compared to for example Newton-Raphson and its inability to detect multiple roots [90]. In this research, the bisection method is used for iterative calculation procedures because of its ease of implementation.

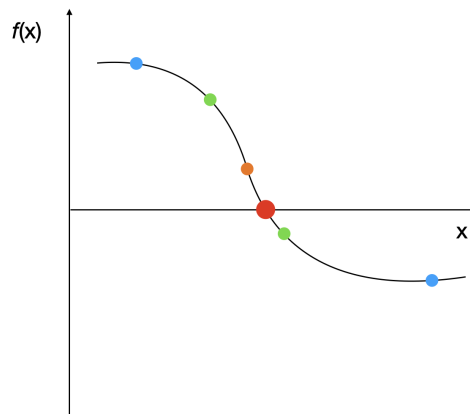


Figure 4.7: Visual representation of the bisection method.

# Ejector Refrigeration Cycles

With the model for the ejector established, different ejector refrigeration cycles can be simulated thermodynamically. In this chapter, a systematical analysis of different possible configurations of ejector refrigeration cycles is presented, highlighting their advantages and limitations. The cycles will be presented in the form of a schematic drawing, explanation and COP calculation. For the list of symbols used in the schematic drawings, see appendix D. For two of the three presented ejector refrigeration cycles, a simulation and optimization flowchart is included.

## 5.1 Hybrid Ejector Refrigeration Cycle 1

The first ejector refrigeration cycle is called a hybrid refrigeration cycle since the ejector works in tandem with a compressor or booster. A similar design has been proposed first by Sokolov and Hershgal in 1990 [14], and numerically tested by Cheng et al. in 2021 [91].

### 5.1.1 Configuration

A schematic drawing of the first hybrid ejector refrigeration cycle can be seen in figure 5.1. The pressure of the evaporator outlet (point 1) is increased by the booster and the ejector, respectively. The booster increases the pressure to a level where the ejector, can lift the pressure of the combined streams of points 2 and 6, enough to overcome the back pressure or condenser pressure in point 3. This pressure is determined by the condenser temperature and working fluid. The minimum condenser temperature is limited by the ambient (outside) temperature. This limitation is explained by the second law of thermodynamics, stating that spontaneous flow of heat occurs from regions of higher temperature to regions of lower temperature [92]. The condenser temperature thus has to be higher than the ambient temperature. In this research, the temperature difference between the condenser and the ambient is fixed at 5 K, as explained in section 3.4.2.

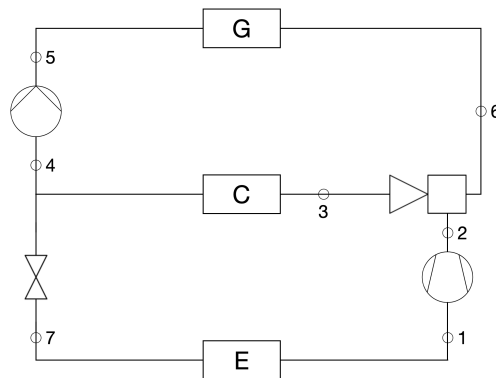


Figure 5.1: Schematic drawing of hybrid 1.

### 5.1.2 Coefficient of Performance Hybrid 1

The coefficient of performance is defined as the cooling power divided by the (electrical) power input. In the case of hybrid 1 this is the cooling power of the evaporator, divided by the sum of the power consumption of the booster and pump. By taking the points of figure 5.1 and using the entrainment ratio  $\gamma$  to account for difference in mass flow, the COP can be calculated using equation 5.1:

$$COP_{H1} = \frac{\gamma(h_1 - h_7)}{\gamma(h_2 - h_1) + (h_5 - h_4)} \quad (5.1)$$

The simulation and optimization of hybrid 1 is visualized in the flowchart in figure 5.2. Herein,  $P_{Tsat+SH}$  is the upper limit for the generator pressure, that is the pressure that guarantees evaporation and subsequent superheating in the generator (between point 5 and 6). The Matlab script for the modeling of hybrid 1 can be seen in appendix E.1.

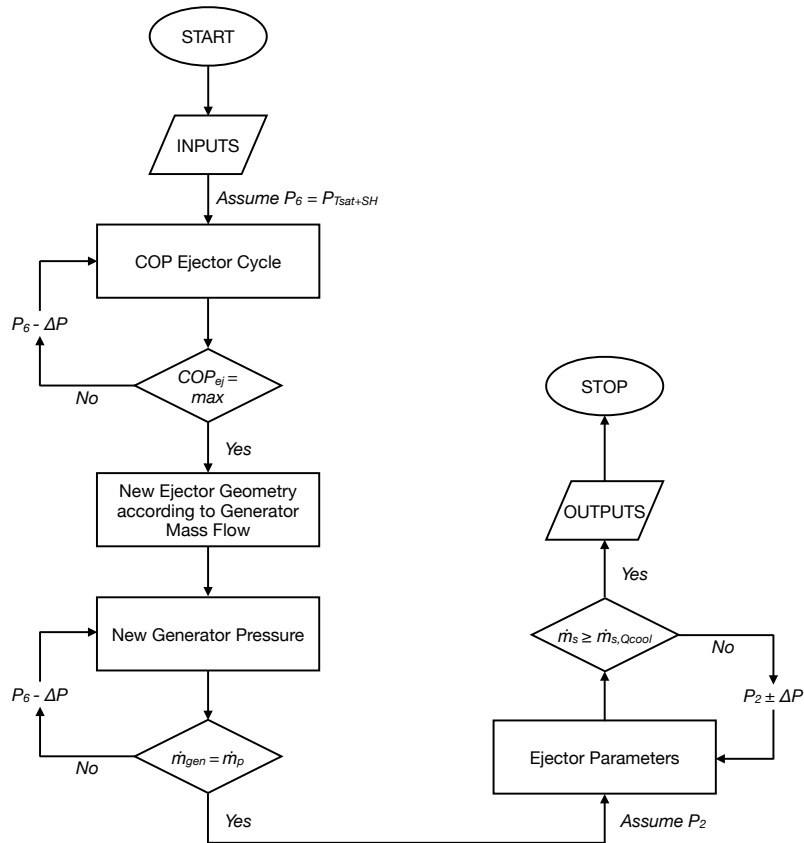


Figure 5.2: Hybrid 1 simulation flowchart.

## 5.2 Hybrid Ejector Refrigeration Cycle 2

The second ejector refrigeration cycle is similar to the cycle presented in section 5.1, apart from the placement of the ejector. In this cycle, the ejector is placed before the booster. This cycle was proposed by Yan et al. in 2016 [93].

### 5.2.1 Configuration

A schematic drawing of the second hybrid ejector refrigeration cycle can be seen in figure 5.3. In hybrid 2, the order of the ejector and booster is different to hybrid 1. The pressure of the evaporator outlet (point 1) is increased by the ejector and the booster, respectively. The ejector lifts the pressure with the help of the primary flow (point 6). Subsequently, the booster increases the pressure to the condensing pressure. For an explanation on the condensing pressure, see section 5.1.1.

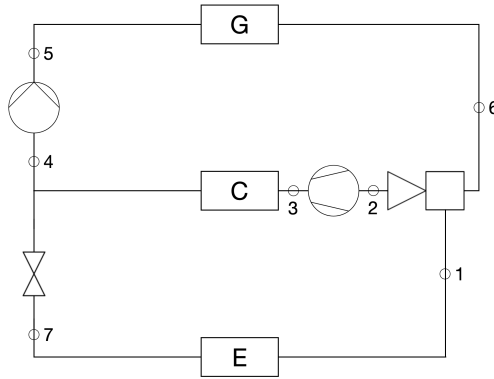


Figure 5.3: Schematic drawing of hybrid 2.

### 5.2.2 Coefficient of Performance Hybrid 2

In the case of hybrid 2 the COP is again calculated as the cooling power of the evaporator, divided by the sum of the power consumption of the booster and pump. Because of the different configuration, the equation for the COP is different from equation 5.1:

$$COP_{H2} = \frac{\gamma(h_1 - h_7)}{(h_3 - h_2)(\gamma + 1) + (h_5 - h_4)} \quad (5.2)$$

From equation 5.2 it is clear that the COP of hybrid 2 is limited by the fact that the entire mass flow is compressed by the booster, regardless of how much of that mass flow actually contributes to cooling effect through evaporation. This creates two key inefficiencies:

- Only a fraction of the total mass flow participates in the evaporation and thus contributes to the cooling effect (useful work).
- Since compression work is proportional to the mass flow rate, compressing the entire flow increases the booster's power input. This directly reduces the COP.

Based on the inherently lower COP of hybrid 2 compared to hybrid 1, it is excluded from the performance analysis.

### 5.3 Mechanical Sub-Cooling Cycle

A schematic drawing of the mechanical sub-cooling cycle can be seen in figure 5.4. In the MSC, the ejector cycle is coupled to a conventional refrigeration cycle, explained in section 3.4.1. In this configuration, the ejector refrigeration cycle performs mechanical sub-cooling.

The MSC comprises a generator (G), an ejector, two condensers (C1 & C2), an evaporator (E), a heat exchanger (HEX), a pump and a compressor. Heat is extracted in the evaporator, where the working fluid absorbs heat from the cooled space, evaporating into a low-pressure vapor (state point 1). This vapor is compressed by the compressor (state points 1 to 2), increasing its pressure and temperature. The vapor is condensed (or cooled in case of transcritical operation) in condenser C1, the vapor or liquid in point 3 is then mechanically sub-cooled by the upper cycle. The upper cycle is a standard ejector refrigeration cycle as presented in section 3.4.2. This cycle was proposed by Llopis et al. [94] in 2018 and numerically evaluated in 2021 by Yadav and Sarkar [57] (see section 3.5.4). The Matlab script for the modeling of the MSC can be seen in appendix E.2.

#### 5.3.1 Configuration

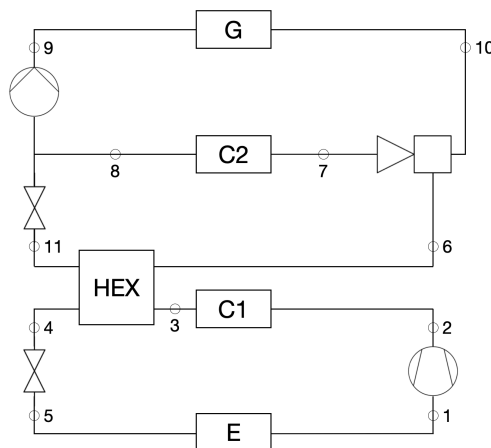


Figure 5.4: Schematic drawing of MSC.

#### 5.3.2 Coefficient of Performance MSC

In the case of the MSC, the COP is calculated as the cooling load of the evaporator of the lower refrigeration cycle, over the power consumption of the compressor in the lower cycle and pump in the upper cycle:

$$COP_{H3} = \frac{\dot{m}_{vc}(h_1 - h_5)}{\dot{m}_{vc}(h_2 - h_1) + \dot{m}_{ec}(\gamma + 1)^{-1}(h_9 - h_8)} \quad (5.3)$$

where  $\dot{m}_{vc}$  is the mass flow through the vapor compression cycle and  $\dot{m}_{ec}$  and  $\gamma$  are the mass flow and entrainment ratio of the ejector cycle, respectively.

Potential benefits of the mechanical sub-cooling cycle are:

- Possibility of higher temperature for inlet of the secondary flow in the ejector cycle (point 6 in figure 5.4).
- Possibility of different working fluids in each cycle enhancing their fit-for-purpose.

Figure 4.3 presents a flowchart representing the calculation and optimization procedure in the MSC. Again,  $P_{T_{sat}+SH}$  is the upper limit for the generator pressure i.e. the pressure that guarantees evaporation and superheating between point 9 and 10.

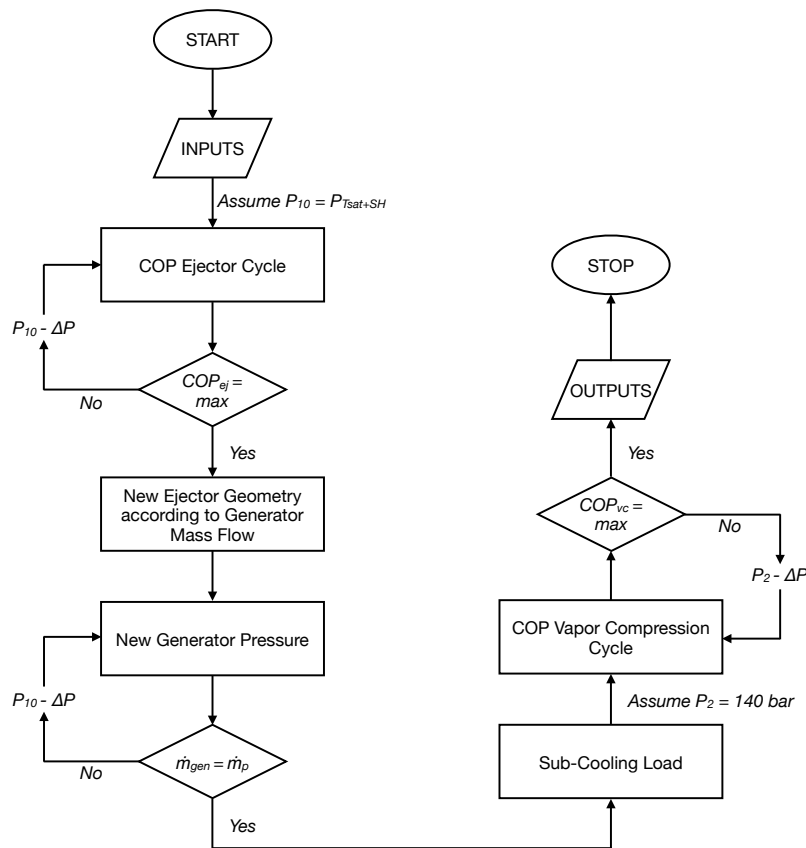


Figure 5.5: Mechanical sub-cooling cycle simulation flowchart.

## 5.4 Multi Ejector Design

In this section, the method for determining the number of ejectors and their geometries in a multi-ejector system can be read.

The heat and thus mass flow in a solar ejector cycle is dictated by the combination of the inlet temperature, (target) outlet temperature and area of the solar collector, area of the solar collector  $A_{solar}$ , solar irradiance  $G$  and thermal efficiency of the solar collector  $\eta_{sc}$  as explained in section 3.6. To ensure steady ejector operation and performance under varying (primary) mass flow, an array of ejectors could be used, resulting in range of effective ejector throat areas. A visualization of such an array of ejectors can be seen in figure 5.6.

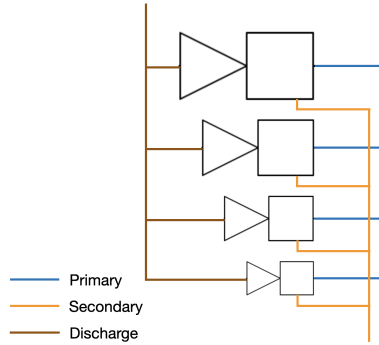


Figure 5.6: Visualization of an array of 4 ejectors.

A script is developed to determine an optimal array of throat diameters  $D_t$  for the ejectors, ensuring the best coverage of effective areas within a specified range. The range is defined by the minimum area, corresponding to the throat of the smallest ejector, and the maximum area, representing the sum of all throat areas in the ejector array. To find the optimal array of throat diameters, candidate diameters are generated based on the target range, and all possible combinations of the ejectors are evaluated for a given number of ejectors in the array. The process begins by dynamically generating candidate diameters based on the target area range, ensuring coverage from the smallest to the largest effective area. All possible combinations of the candidate diameters are evaluated for a fixed number of ejectors,  $n$ . For each combination, the unique effective area is computed as:

$$A_{t,effective} = \frac{\pi}{4} \sum_{i=1}^n D_{t,i}^2 \quad (5.4)$$

The script evaluates the cumulative coverage of the combined effective areas for each combination and identifies the optimal set of diameters that provides the widest coverage whilst meeting the constraints of the target range. The different combinations are evaluated based on the standard deviation of the gaps between consecutive unique effective areas. A lower standard deviation indicates a more uniform distribution of achievable areas, ensuring a finer resolution across the target range. The optimal combination is selected by identifying the set of diameters that results in the smallest standard deviation of gaps while covering the entire specified range from the minimum to the maximum effective area. This approach guarantees that the distribution of achievable areas is as uniform as possible, minimizing the gaps between effective ejector throat areas. The script used to find the set of throat diameters can be seen in appendix F.

## 5.5 Seasonal Performance Evaluation and Economic Analysis

To obtain the seasonal performance of each refrigeration cycle, weather data from the *Photovoltaic Geographical Information System* (or *PVGIS*) of the European Commission [95] is combined with thermodynamic models created for the cycles presented in sections 5.1 and 5.3. The performance of the ejector therein is calculated by model 2 presented in section 4.3. The used weather data comprises solar irradiance and air temperature. Solar irradiance is the power per unit area (or surface power density) received from the sun in the form of electromagnetic radiation [96]. Solar irradiance is measured in SI units in watts per square meter ( $\frac{W}{m^2}$ ). The air temperature provided by the *PVGIS* is measured in degrees centigrade ( $^{\circ}C$ ) and thus has to be converted to Kelvin for calculations.

The air temperature dictates both the efficiency of the solar thermal collectors as explained in section 3.6 and the lower limit of the condenser temperature in the refrigeration cycle as explained in section 3.4.2. Results will be presented for 4 geographical locations representing 4 of the 5 Köppen climate types: tropical, arid, temperate and continental [97]. The fifth climate type (polar) is omitted because of lack of relevance for residential refrigeration. The 4 geographical locations are:

- Georgetown, Guyana. Classification 'Af': tropical rainforest
- Niamey, Niger. Classification 'BWs': hot semi-arid
- Palermo, Italy. Classification 'Csa': hot-summer subtropical
- Sapporo, Japan. Classification 'Dfa': humid continental

In figure 5.7, world map with the locations highlighted can be seen. It is important to note that all locations are in the northern hemisphere, ensuring ease of comparison across seasonal data.

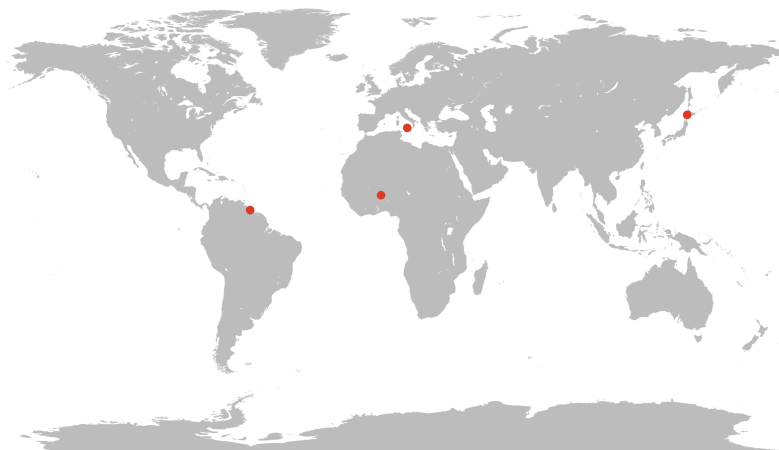


Figure 5.7: World map with reviewed locations.

The wide spread of the locations and their climate aids in the general evaluation of the refrigeration cycles. Table 5.1 provides insight into the mean daily temperature, mean maximum temperature and mean sunshine hours of the four locations. Table 5.2 presents the mean temperature and mean nonzero solar irradiance in the weather datasets retrieved from *PVGIS*.

Location	Ref.	Mean Daily Temperature ( $^{\circ}C$ )	Mean Maximum Temperature ( $^{\circ}C$ )	Mean Sunshine Hours
Georgetown	[98]	27.3	30.5	2531
Niamey	[99]	29.9	36.6	3179
Palermo	[100]	18.9	22.0	2968
Sapporo	[101]	9.2	32.7	1718

Table 5.1: Mean daily and maximum temperature and sunshine hours 1991-2020 for reviewed locations.

Location	Mean Temperature ( $^{\circ}C$ )	Maximum Temperature ( $^{\circ}C$ )	Mean Nonzero Solar Irradiance ( $\frac{W}{m^2}$ )
Georgetown	27.30	32.76	490.64
Niamey	30.00	44.30	562.14
Palermo	18.00	41.29	467.96
Sapporo	14.09	31.28	375.84

Table 5.2: Mean and maximum temperature and mean nonzero solar irradiance 2023 for reviewed locations. Data: [95].

To aid in comparison, a baseline will be created to develop a general idea of the performance and energy consumption of a conventional vapor compression cycle (explained in section 3.4.1) paired with photovoltaic panels. For the development of the baseline in each of the four locations, a hypothetical cooled space is assumed to have the following parameters:

- (Roof) area for the solar thermal collectors or photovoltaic panels is  $25 m^2$ .
- The total wall and roof surface area is  $105 m^2$ , based on a home size of  $50 m^2$  [102].
- Share of window surface area is 20%.
- The total surface area of  $105 m^2$  has an average U value of  $2 \frac{W}{m^2 \cdot K}$ , based on window surface area [103].
- Air conditioning is turned on when ambient temperatures are above  $21 ^{\circ}C$ .

Based on the stated assumptions the daily and total electrical power consumption of an air conditioning system based on a vapor compression cycle is calculated. Herein, the cooling load per hour is assumed to consist only of heat transfer by conduction. This heat transfer and thus cooling load is calculated in the following way:

$$Q_{cool} = U \cdot A \cdot \Delta T \quad (5.5)$$

where  $\Delta T$  is equal to the difference between the outside temperature  $T_{air}$  minus the fixed assumed inside temperature of  $19.5 ^{\circ}C$ , and  $U$  and  $A$  are equal to the values assumed above.

The economic analysis will comprise the capital expenses (CAPEX) and operational expenses (OPEX) of the proposed refrigeration cycles, in order to assess their economic feasibility. For the CAPEX, a combination of equations and estimates is used to determine the individual component costs. The cost of the compressor is estimated by an equation proposed by Yadav and Sarkar in 2021 [57]:

$$CAPEX_{compressor} = \frac{573 \cdot \dot{m}_{comp}}{0.8896 - \eta_{is}} \cdot \frac{P_{out}}{P_{in}} \cdot \ln\left(\frac{P_{out}}{P_{in}}\right) \quad (5.6)$$

where  $\dot{m}_{comp}$  is the (maximum) mass flow through the compressor,  $\eta_{is}$  is the isentropic efficiency of the compressor and  $P_{in}$  and  $P_{out}$  are the pressure at the inlet and outlet of the compressor, respectively. For the condenser and evaporator cost, 2004 equations proposed by Selbaş et al. [104] are used:

$$CAPEX_{condenser} = 516.62 \cdot A_c + 268.45 \quad (5.7)$$

$$CAPEX_{evaporator} = 309.14 \cdot A_e + 231.92 \quad (5.8)$$

where  $A_c$  and  $A_e$  are the condenser and evaporator area in  $m^2$ , respectively. The areas will be calculated through the LMTD method for counter-current heat exchangers (equations 3.10 and 3.12 in section 3.7). The chemical engineering plant cost index or CEPCI [105] will be used to convert the 2021 and 2004 component costs to present day values. Scaling component costs is done according to the six-tenth rule [106]. This results in the following set of equations:

$$CAPEX_{new} = CAPEX_{old} \cdot \frac{CEPCI_{new}}{CEPCI_{old}} \quad (5.9)$$

$$CAPEX_A = CAPEX_B \cdot \left(\frac{Size_A}{Size_B}\right)^{0.6} \quad (5.10)$$

The assumptions for the other individual component prices can be seen in table 5.3. The price of valves, piping and controlling equipment is considered to be negligible.

Component	Ref.	Unit Price (EUR)
2 $m^2$ Solar Thermal Collector Panel	[107]	225
Multi-Ejector Design with 7 ejectors	[24]	235
Generator Pump	[108]	305

Table 5.3: Assumed component prices 2023 for reviewed locations.

For the OPEX, the energy consumption of the refrigeration cycle is multiplied by the electricity price in EUR per  $kWh$ . In table 5.4, the price of 1  $kWh$  of electricity can be seen for the reviewed locations.

Location	Ref.	Electricity Price ( $\frac{EUR}{kWh}$ )
Georgetown	[109]	0.31
Niamey	[110]	0.12
Palermo	[111]	0.16
Sapporo	[112]	0.20

Table 5.4: Electricity prices 2023 for reviewed locations.

# 6

## Results

---

In this chapter, the results of the seasonal simulations as well as multi-ejector model and economic analysis will be presented. Section 6.1 presents the results of the simulation of a conventional air conditioner paired with photovoltaic panels, detailing the variation in cooling load and electricity generation. Section 6.2 presents the results of hybrid 1, split up between single case (COP) calculations and the results of the seasonal simulations (SCOP). A statistical analysis of the ejector performance in the seasonal simulations is also included. Section 6.3 presents the results of the mechanical sub-cooling cycle analogously to the results of hybrid 1. Section 6.4 presents the selection of the optimal combination of ejector diameters in the multi-ejector system consisting of 4 to 7 ejectors. The chapter concludes with the results of the economic analysis in section 6.5. As mentioned in section 5.2, hybrid 2 is not included in the performance analysis, due to its inherently lower COP compared to hybrid 1, as explained in section 5.2.2.

## 6.1 Vapor Compression Cycle with PV Panels

In figure 6.1, a simulation of 2023 for Georgetown (6.1a), Niamey (6.1b), Palermo (6.1c) and Sapporo (6.1d) can be seen. In table 6.1, the total energy consumption of the air conditioning system can be seen, as well as the total power generation of the photovoltaic panels.

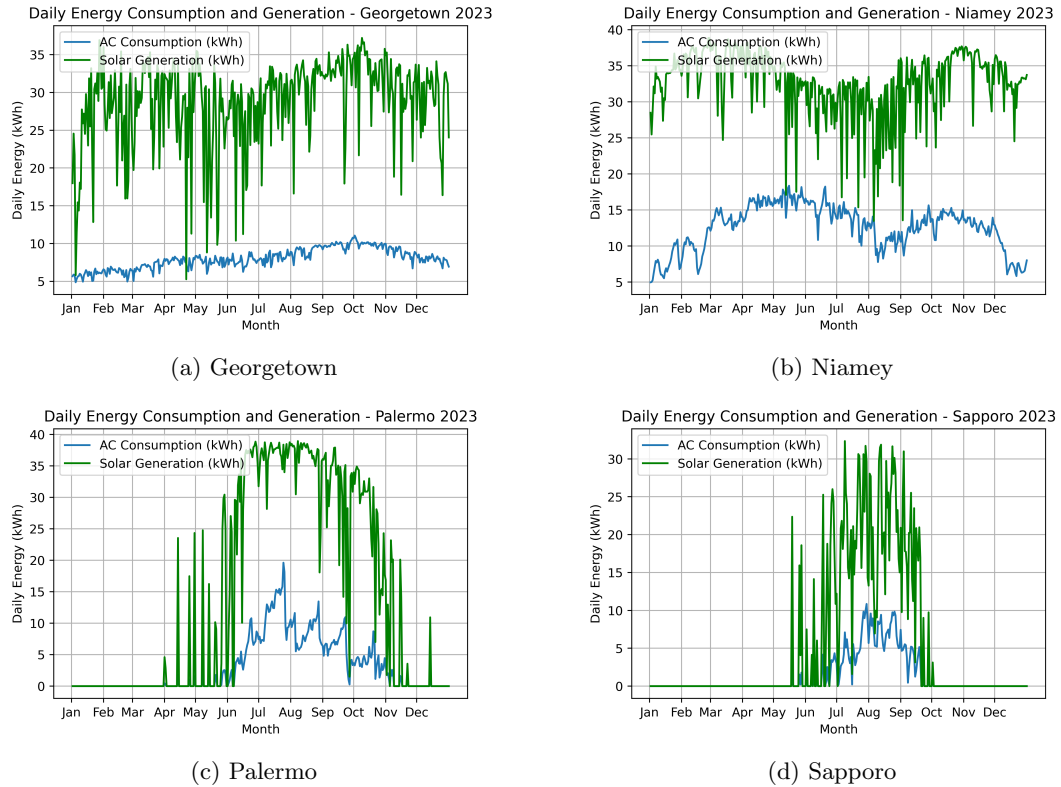


Figure 6.1: Seasonal simulation vapor compression cycle with PV panels. Data: [95].

To create the graphs in figure 6.1, a cutoff temperature (also stated in the assumptions in section 5.5) was used. The total energy generation by the solar panels in table 6.1 includes only the energy that is generated while the air conditioner is running.

Location	Cooling Energy Consumption ( <i>kWh</i> )	Solar Energy Generation ( <i>kWh</i> )	Percentage Generated (%)
Georgetown	4608.88	10511.88	228.12
Niamey	6691.85	11905.03	178.01
Palermo	1305.24	5227.51	400.65
Sapporo	505.13	1944.02	385.05

Table 6.1: Seasonal energy data for refrigeration and solar generation for reviewed locations.

In table 6.1 it can be seen that for the assumed conditions and area of solar panels, photovoltaic panels can supply about two to four times the energy consumed by the air conditioning system.

## 6.2 Hybrid 1

In this section, the results of both single point and seasonal analysis of hybrid 1 can be seen. Sections 6.2.1 and 6.2.2 cover general results, while sections 6.2.4 and 6.2.5 cover the results of the seasonal simulations for all four geographical locations. The results presented in this section achieved with propane or R290 as the working fluid in both hybrid 1 and reference cycles, unless mentioned otherwise. All results are achieved through a 7 ejector design, except for table 6.6 that presents the SCOP with a 4 ejector system for comparison. The multi-ejector design will be detailed in section 6.4. The solar thermal collectors are modeled with the efficiency parameters of the SUN600.20 by Lacaze Energies (table 3.4). The collector efficiency  $\eta_{sc}$  is calculated by assuming that the solar collector temperature is equal to the average of its superheated outlet temperature and the saturation temperature. The compressor and pump are assumed to have a constant isentropic efficiency of 0.8.

### 6.2.1 Influence Secondary Pressure on COP Hybrid 1

In figure 6.2, the relationship between the secondary or suction flow pressure ( $P_s$ ) and the coefficient of performance (COP) of the refrigeration cycle is illustrated. The plot illustrates the role of the secondary pressure in determining the performance of the system. For a given set of operating conditions (ambient temperature  $T_{air}$ , solar irradiance  $G$ , primary inlet pressure  $P_p$ ) and fixed system size (ejector size and solar panel area  $A_{solar}$ ), the secondary pressure directly influences the efficiency of the cycle. As depicted in the figure, the COP decreases as the secondary pressure increases.

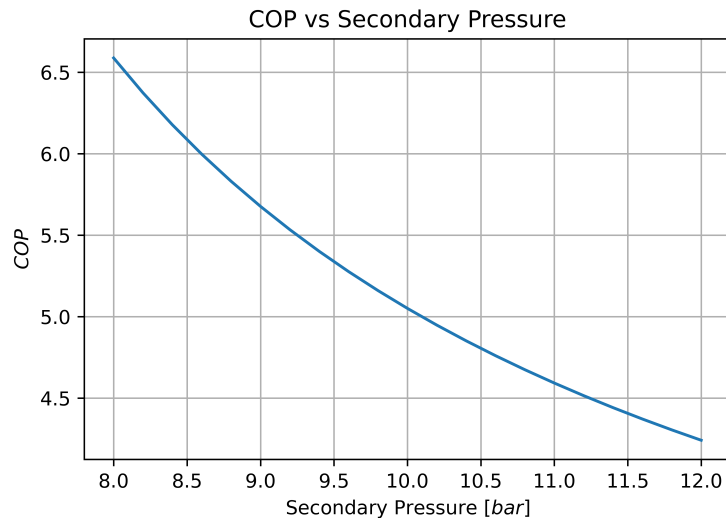


Figure 6.2: COP hybrid 1 vs secondary inlet pressure.

The exact values of the COP for different secondary pressures between 8 and 12 bar can be seen in table 6.2. The primary inlet pressure for the ejector, which is the generator pressure in hybrid 1 is fixed at 1.7 times the condenser pressure for all ambient temperatures. From both the shape of figure 6.2 and table 6.2 it can be seen that the the secondary inlet pressure and COP of the cycle have a nonlinear inverse relationship.

$P_s$ (bar)	$COP_{H1}$	$P_s$ (bar)	$COP_{H1}$
8.0	6.59	10.0	5.05
8.2	6.37	10.2	4.95
8.4	6.18	10.4	4.85
8.6	5.99	10.6	4.76
8.8	5.83	10.8	4.67
9.0	5.68	11.0	4.59
9.2	5.53	11.2	4.51
9.4	5.40	11.4	4.44
9.6	5.28	11.6	4.37
9.8	5.16	11.8	4.30
10.0	5.05	12.0	4.24

Table 6.2: COP hybrid 1 at different values of secondary pressure  $P_s$  with fixed proportional primary pressure, ambient temperature and solar irradiance.

### 6.2.2 Influence Ambient Temperature on COP Hybrid 1

As explained in section 3.4, the ambient temperature dictates the lower limit of the pressure in the condenser. In figures 6.3 through 6.5, the COP of hybrid 1 can be seen in relation to the ambient temperature, for three levels of solar irradiance ( $G = 600, 900$  and  $1200 \frac{W}{m^2}$ , respectively).

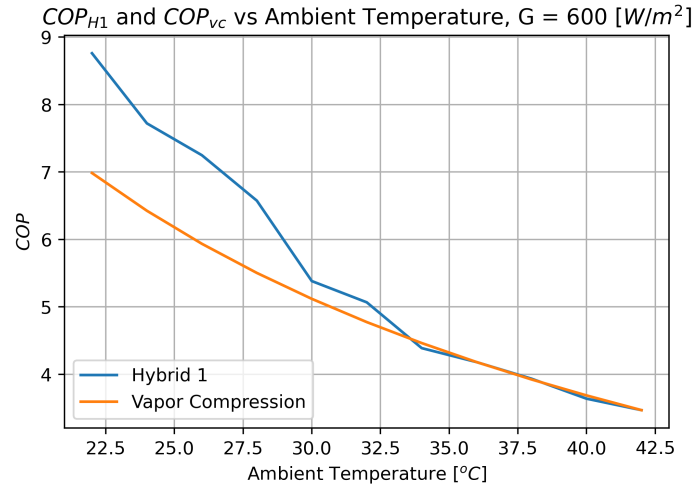


Figure 6.3:  $COP_{H1}$  and  $COP_{vc}$  vs ambient temperature,  $G = 600 [W/m^2]$ .

Figure 6.3 shows the COP of hybrid 1 versus the ambient temperature with a constant solar irradiance of  $600 \frac{W}{m^2}$  and the COP of a vapor compression cycle for reference. The difference in COP between hybrid 1 and the reference cycle can be seen to decrease for increasing ambient temperature between 22 and 42 °C. At an ambient temperature of 34 °C, the COP of hybrid 1 decreases below the value of the reference cycle. For ambient temperatures of 36 °C and higher, the COP of the reference cycle and hybrid 1 are equal.

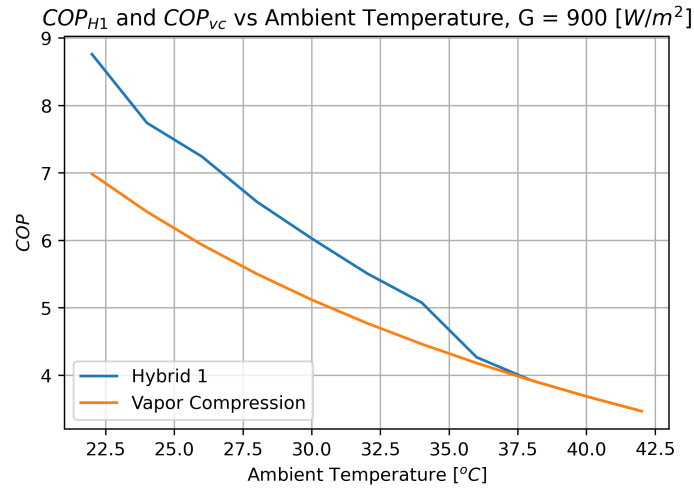


Figure 6.4:  $COP_{H1}$  and  $COP_{vc}$  vs ambient temperature,  $G = 900 [W/m^2]$ .

Figure 6.4 shows the COP of hybrid 1 versus the ambient temperature with a constant solar irradiance of  $900 \frac{W}{m^2}$  and the COP of a vapor compression cycle for reference. The difference between the COP of hybrid 1 and the COP of the reference cycle can be seen to decrease for increasing ambient temperature. At ambient temperatures of  $38 \text{ }^\circ\text{C}$  and higher, the COP of hybrid 1 matches that of the reference cycle.

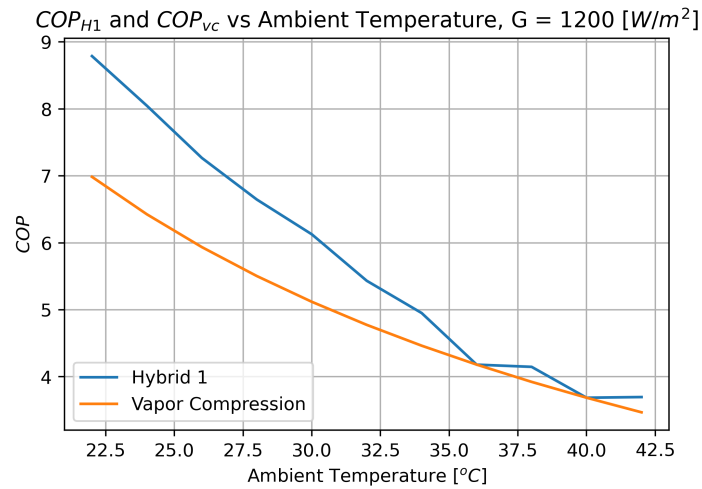


Figure 6.5:  $COP_{H1}$  and  $COP_{vc}$  vs ambient temperature,  $G = 1200 [W/m^2]$ .

Figure 6.5 shows the COP of hybrid 1 versus the ambient temperature with a constant solar irradiance of  $1200 \frac{W}{m^2}$  and the COP of a vapor compression cycle for reference. The difference between the COP between hybrid 1 and the reference cycle decreases for increasing ambient temperature. This decrease in COP difference is largest between  $22$  and  $36 \text{ }^\circ\text{C}$ . At an ambient

temperatures of 36 °C, the COP of hybrid 1 rises above the reference COP again. At 40 °C, the COPs are equal again and at  $T_{air} = 42$  °C, the COP of hybrid 1 is higher than the COP of the vapor compression cycle.

$T_{air}$ (°C)	$COP_{vc}$	$COP_{H1}$ $G = 600 \frac{W}{m^2}$	$COP_{H1}$ $G = 900 \frac{W}{m^2}$	$COP_{H1}$ $G = 1200 \frac{W}{m^2}$
22	6.99	8.76	8.76	8.79
24	6.43	7.72	7.74	8.05
26	5.94	7.25	7.24	7.27
28	5.50	6.57	6.57	6.65
30	5.12	5.38	6.03	6.13
32	4.77	5.07	5.51	5.43
34	4.46	4.39	5.08	4.95
36	4.18	4.18	4.27	4.18
38	3.92	3.93	3.92	4.15
40	3.69	3.64	3.69	3.69
42	3.47	3.47	3.47	3.70

Table 6.3: Comparison of COPs hybrid 1 for different ambient temperatures and solar irradiance.

In table 6.3 the values of the COPs of hybrid 1 for the different ambient temperatures and solar irradiance can be seen, the COP of the reference cycle is also included for each value of  $T_{air}$ . Regardless of the solar irradiance, hybrid 1 is achieve a COP higher than 8.5 for the lowest tested ambient temperature, and achieves a higher COP than the vapor compression cycle up until an ambient temperature of 34 °C. For ambient temperatures of 26 °C and higher, the COP of hybrid 1 with  $G = 600 \frac{W}{m^2}$  decreases below the values achieved by the same cycle at higher solar irradiance, except for the ambient temperature of 32 °C, for which it achieves the highest COP across all solar irradiances. At an ambient temperature of 42 °C, only a solar irradiance of  $G = 1200 \frac{W}{m^2}$  results in a COP higher than the vapor compression COP.

### 6.2.3 Hourly Coefficient of Performance Hybrid 1

Figures 6.6a through 6.6d display the hourly COP achieved by hybrid 1 and the reference vapor compression cycle for all four locations. The displayed COPs are found during hours that the ambient temperature and solar irradiance are above the threshold value, this is explained in more detail in section 6.2.5.

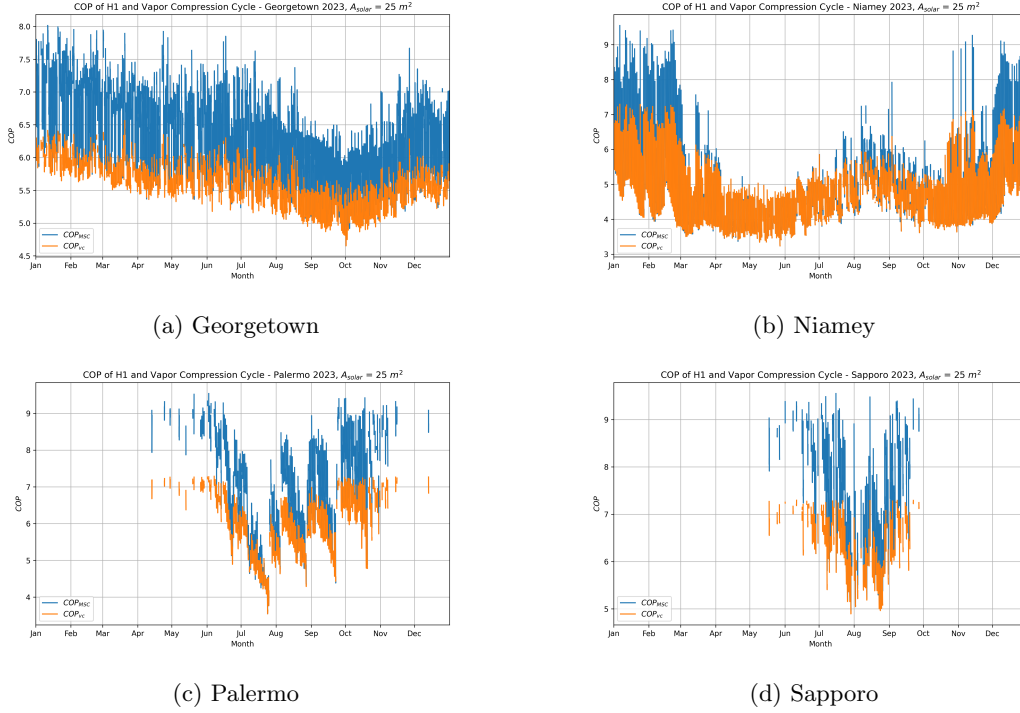


Figure 6.6: Hourly COP in hybrid 1 for all four locations.

Figure 6.6a shows the hourly COPs achieved by hybrid 1 in Georgetown in 2023. It can be seen that Georgetown requires refrigeration (or has conditions above the thresholds) throughout the whole year, with the COP of hybrid 1 being higher than that of the reference cycle virtually all of the hours. Figure 6.6b shows the hourly COPs achieved by hybrid 1 in Niamey in 2023. Similarly to Georgetown, Niamey requires refrigeration throughout the whole year. The COP of hybrid 1 is higher in the months of January, February, and December, while all other months display similar or equal COPs for the reference cycle and hybrid 1. Figure 6.6c displays the hourly COPs achieved by hybrid 1 in Palermo in 2023. Palermo requires most refrigeration between April and November. Except for the month of July, hybrid 1 shows a higher COP than the reference cycle in Palermo. Figure 6.6d shows the hourly COPs achieved by hybrid 1 in Sapporo in 2023. Sapporo displays operation of the refrigeration cycle between May and October, showing a higher COP of hybrid 1 compared to the reference cycles for the entire refrigeration period.

Location	Average COP <sub>vc</sub>	Average COP <sub>H1</sub>	Highest COP <sub>H1</sub>	Lowest COP <sub>H1</sub>
Georgetown	5.55	6.20	8.01	4.79
Niamey	4.53	4.81	9.55	3.24
Palermo	5.85	6.91	9.54	3.55
Sapporo	6.24	7.21	9.55	4.95

Table 6.4: Average COP vapor compression and average, highest and lowest COP hybrid 1.

In table 6.4, the average COP of the reference vapor compression cycle for all four locations, along with the average, highest and lowest COPs achieved by Hybrid 1 in all four locations is displayed. The average COP of Hybrid 1 is higher than the average reference COP in all locations, with Palermo showing the biggest absolute difference (1.06). The highest COP achieved by hybrid 1 in Niamey, Palermo and Sapporo is the same at 8.82. The highest achieved COP in Georgetown is lower at 8.01.

#### 6.2.4 Seasonal Coefficient of Performance Hybrid 1

The seasonal coefficient of performance of a refrigeration cycle is defined as the total amount of cooling in kilowatts divided by the total electrical power input in a year [113]. The SCOP of hybrid 1 in the four geographical locations can be seen in table 6.5 and figure 6.7.

Location	SCOP <sub>vc</sub>	SCOP <sub>H1</sub>	
		A <sub>solar</sub> = 10 m <sup>2</sup>	A <sub>solar</sub> = 15 m <sup>2</sup>
Georgetown	5.47	5.57 (+1.8%)	5.84 (+6.76%)
Niamey	4.22	4.24 (+0.47%)	4.29 (+1.66%)
Palermo	5.33	5.62 (+5.44%)	5.91 (+10.9%)
Sapporo	5.89	6.16 (+4.85%)	6.46 (+9.84%)
Location	SCOP <sub>H1</sub>		
	A <sub>solar</sub> = 20 m <sup>2</sup>	A <sub>solar</sub> = 25 m <sup>2</sup>	A <sub>solar</sub> = 50 m <sup>2</sup>
Georgetown	6.11 (+11.7%)	6.21 (+13.5%)	6.78 (23.9%)
Niamey	4.35 (+3.08%)	4.42 (+4.74%)	4.64 (+9.95%)
Palermo	6.13 (+13.1%)	6.31 (+18.4%)	6.86 (+28.7%)
Sapporo	6.80 (+15.4%)	6.99 (+18.7%)	7.81 (+32.6%)

Table 6.5: Seasonal coefficient of performance hybrid 1

The results presented in table 6.5 summarize the SCOP for 5 different configurations and the 4 geographical locations. The relative percentage increase in SCOP, compared to the vapor compression cycle is shown in parentheses. As mentioned before, the SCOP is calculated by summing the evaporative cooling load throughout the year, and dividing this by the total energy consumption throughout the year. Since hybrid 1 is dependent on ambient conditions and therefore does not function all of the hours that cooling is required, the SCOPs in table 6.5 consist of the COPs of the complete ejector cycle for the hours that it functions, and the COPs of the vapor compression cycle that is integrated in hybrid 1 for the hours where the ejector part of the cycle does not function, or would be less efficient to use (i.e. when the compressor increases the pressure of the secondary flow to a pressure above the one in a vapor compression cycle, or hybrid 1 fails to match the calculated cooling duty). The conditions for failure and rate of

success of the different configurations are detailed in section 6.2.5. The SCOP for hybrid 1 with a multi-ejector design consisting of 4 instead of 7 ejectors is presented in table 6.6. A decrease in SCOP is visible for all configurations and locations with respect to the 7 ejector design.

Location	SCOP <sub>vc</sub>	SCOP <sub>H1</sub>	
		A <sub>solar</sub> = 10 m <sup>2</sup>	A <sub>solar</sub> = 15 m <sup>2</sup>
Georgetown	5.47	5.50 (+0.55%)	5.52 (+0.91%)
Niamey	4.22	4.22 (+0.00%)	4.25 (+0.71%)
Palermo	5.33	5.44 (+2.06%)	5.44 (+2.06%)
Sapporo	5.89	6.04 (+2.55%)	6.09 (+3.40%)
Location	SCOP <sub>H1</sub> A <sub>solar</sub> = 20 m <sup>2</sup>	SCOP <sub>H1</sub> A <sub>solar</sub> = 25 m <sup>2</sup>	SCOP <sub>H1</sub> A <sub>solar</sub> = 50 m <sup>2</sup>
Georgetown	5.70 (+4.20%)	5.86 (+7.13%)	6.36 (+16.3%)
Niamey	4.27 (+1.18%)	4.34 (+2.84%)	4.60 (+9.00%)
Palermo	5.79 (+8.63%)	6.00 (+12.6%)	6.58 (+23.5%)
Sapporo	6.26 (+6.28%)	6.48 (+10.0%)	7.25 (+23.1%)

Table 6.6: Seasonal coefficient of performance hybrid 1 with 4 ejectors.

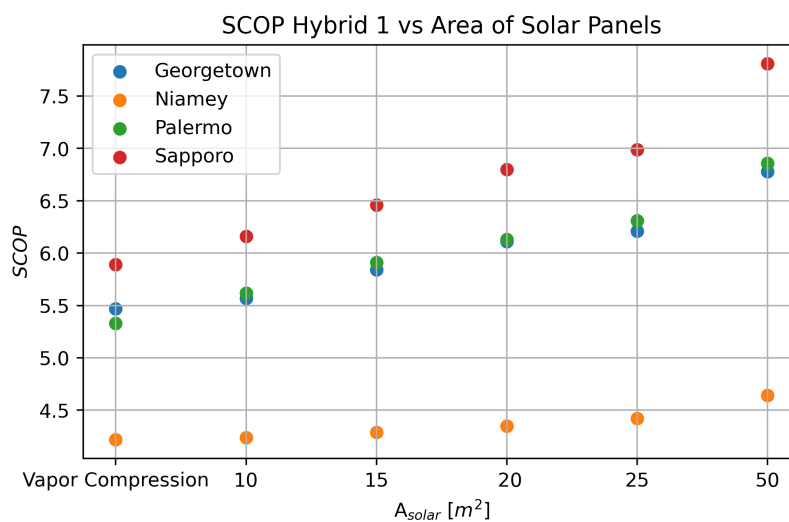


Figure 6.7: SCOP hybrid 1 vs area of solar panels.

The evolution of the SCOP in all four locations, for the different areas of solar panels is visualized in figure 6.7. For Sapporo, the SCOP increases very little between solar panel areas of 10 and 25 m<sup>2</sup>, showing a larger increase in SCOP between 25 and 50 m<sup>2</sup> of solar panel area. The SCOP of Palermo has a similar trajectory, where the difference in SCOP between 10 and 25 m<sup>2</sup> is small compared to the difference in SCOP between 25 and 50 m<sup>2</sup>. In Niamey the SCOP varies little between 10 and 50 m<sup>2</sup> of solar panel area (between 4.39 and 4.51). Georgetown displays a constant increase in SCOP for an increasing A<sub>solar</sub>.

## 6.2.5 Rate of Success Hybrid 1

To determine the performance of hybrid 1 across the four climates, the rate of success for the refrigeration cycle should be determined. Table 6.7 gives insight into how many of the hours that cooling is required, the ejector is successful. The ejector cycle is considered to fail when:

- The secondary inlet pressure has to be increased to a pressure equal to or beyond the condenser pressure. This is considered a failure because a vapor compression cycle has an inherently higher COP at this point, omitting the work done by the pump while achieving the same cooling duty in the evaporator.
- The final cooling load achieved by the cycle is lower than the required cooling load as calculated with the assumptions presented in section 5.5.
- The outlet temperature of the generator is higher than 80 °C, which is considered not to be realistic with solar thermal collectors (see section 3.6).

In the second upper column, the amount hours there are where conditions are above the set thresholds ( $T_{air} > 21^{\circ}C$ ,  $G > 300 \frac{W}{m^2}$ ) can be seen.

Location	Hours Above Threshold	Hours Successful $A_{solar} = 10 m^2$	Hours Successful $A_{solar} = 15 m^2$
Georgetown	2793	1263 (45.2%)	1814 (64.9%)
Niamey	3032	428 (14.1%)	1158 (38.2%)
Palermo	1309	719 (54.9%)	983 (75.1%)
Sapporo	579	239 (41.3%)	384 (66.3%)
Location	Hours Successful $A_{solar} = 20 m^2$	Hours Successful $A_{solar} = 25 m^2$	Hours Successful $A_{solar} = 50 m^2$
Georgetown	2282 (81.7%)	2418 (86.6%)	2659 (95.2%)
Niamey	1366 (45.1%)	1660 (54.7%)	2573 (84.9%)
Palermo	1093 (83.5%)	1179 (90.1%)	1269 (96.9%)
Sapporo	456 (78.8%)	494 (85.3%)	551 (95.2%)

Table 6.7: Successful cooling hours.

Table 6.7 presents the successful cooling hours for the four geographical locations analyzed across varying solar collector areas ( $A_{solar}$ ). The percentage of successful hours increases with larger collector areas for all locations. For the smallest solar area,  $A_{solar} = 10 m^2$ , Palermo is the only location where the ejector cycle is successful more than 50% of the time, while Georgetown, Niamey and Sapporo show a success rate of 45.2%, 14.1% and 41.3%, respectively. As the collector area increases to  $50 m^2$ , the success rate approaches 100% in Sapporo (95.2%), Palermo (96.9%) and Georgetown (95.2%). Niamey displays a lower success rate of 84.9% at the largest tested solar collector area.

## 6.2.6 Ejector Performance Hybrid 1

The ejector performance is defined by the entrainment ratio  $\gamma$  and the overall ejector efficiency  $\eta_{ejector}$  as presented in equation 3.1 in section 3.2. In figure 6.8, the distribution of the ejector efficiencies achieved by the ejector in hybrid 1 in the four geographical locations can be seen.

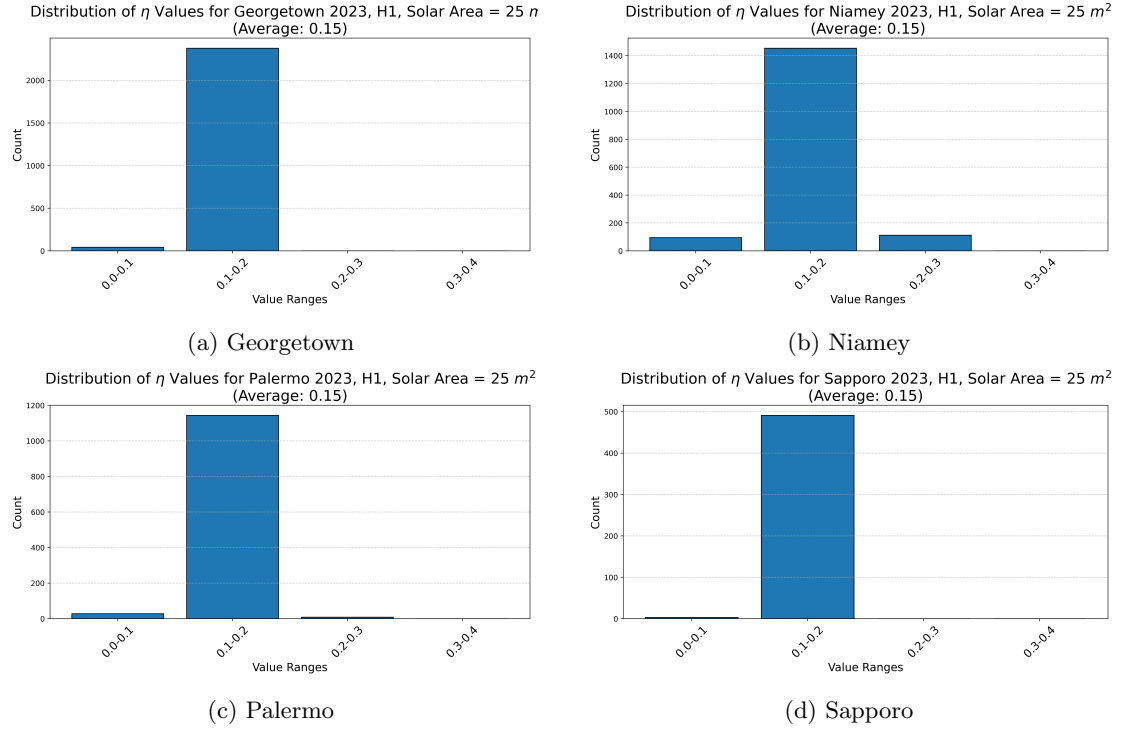


Figure 6.8: Distribution and average of achieved ejector efficiencies  $\eta_{ejector}$  in hybrid 1 for all four locations.

All of the locations have the majority of their ejector efficiencies in the value range between 0.1 and 0.2 (or 10 and 20%) and some efficiencies between 0.2 and 0.3. Georgetown (figure 6.8a), Niamey (figure 6.8b) and Palermo (figure 6.8c) also have efficiency values between 0 and 0.1, while Sapporo (figure 6.8d) does not. In table 6.8, the average, highest and lowest achieved ejector efficiency can be seen for the fixed solar panel area of 25  $m^2$ .

Location	Average $\eta_{ejectorH1}$	Highest $\eta_{ejectorH1}$	Lowest $\eta_{ejectorH1}$
Georgetown	0.155	0.192	0.072
Niamey	0.151	0.248	0.032
Palermo	0.145	0.234	0.049
Sapporo	0.149	0.189	0.078

Table 6.8: Average, highest and lowest  $\eta_{ejector}$  hybrid 1.

Figure 6.9 displays the distributions and averages of the entrainment ratios achieved in the ejector in hybrid 1.

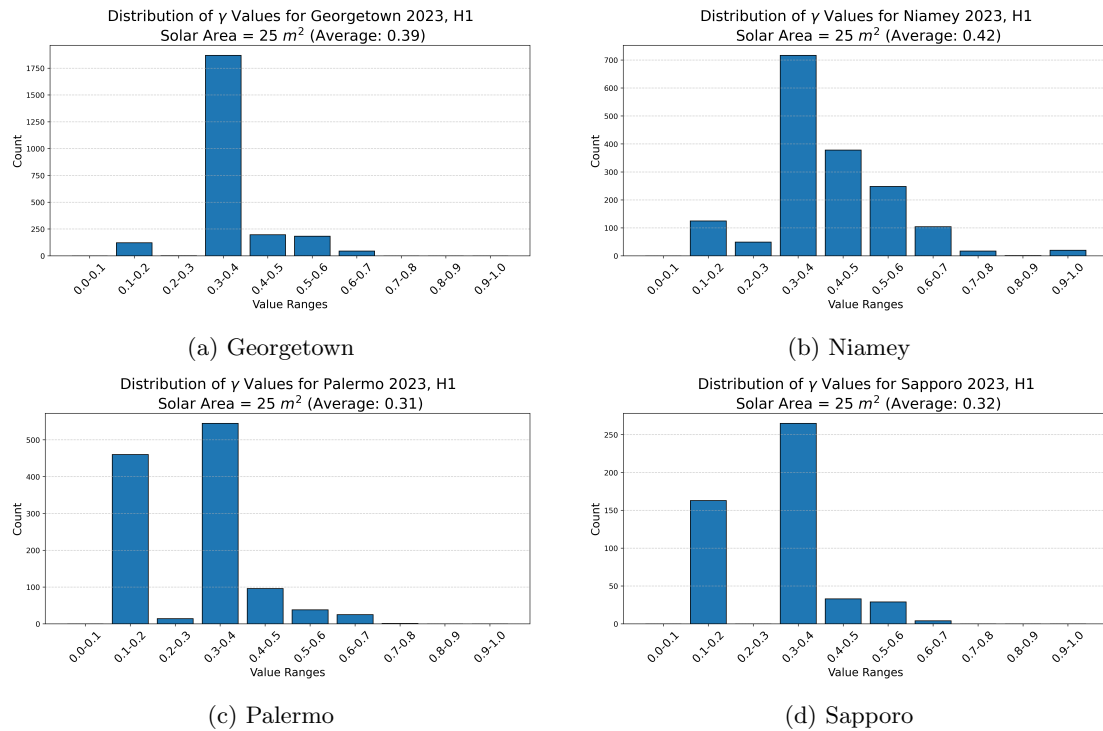


Figure 6.9: Distribution and average of  $\gamma$  in hybrid 1.

In all four locations, the majority of the entrainment values achieved by the ejector are in the 0.3-0.4 range. Georgetown (figure 6.9a) and Sapporo (figure 6.9d) have all of the achieved entrainment ratios between 0.1 and 0.7, while Niamey (figure 6.9b) has  $\gamma$  values between 0.1 and 1. Palermo (figure 6.9c) displays a large share of its entrainment ratios in the 0.1-0.2 range. Table 6.9 displays the average, highest and lowest value  $\gamma$  for each of the four locations. In Niamey, displaying the highest average entrainment ratio, a maximum entrainment ratio of 0.998 is achieved. The other locations show a maximum entrainment between 0.673 and 0.714.

Location	Average $\gamma$	Highest $\gamma$	Lowest $\gamma$
Georgetown	0.386	0.686	0.119
Niamey	0.423	0.998	0.118
Palermo	0.306	0.714	0.133
Sapporo	0.322	0.673	0.146

Table 6.9: Average, highest and lowest  $\gamma$  hybrid 1.

## 6.3 Mechanical Sub-Cooling Cycle

In this section, the results of both single point and seasonal analysis of the mechanical sub-cooling cycle or MSC can be seen. Section 6.3.1 covers general results, while sections 6.3.3 through 6.3.5 present the results of the seasonal simulations for all four geographical locations. The results presented for the MSC are achieved with propane or R290 as the working fluid in the ejector or mechanical sub-cooling part of cycle, and  $CO_2$  or R744 as the working fluid in the vapor compression cycle inside the MSC unless mentioned otherwise. The reference vapor compression cycle also uses R744 as the working fluid. In the ejector cycle, the evaporator or internal heat exchanger outlet temperature is fixed at  $20\text{ }^\circ C$ . All results except table 6.12 are achieved through a 7 ejector design, which is detailed in section 6.4. The solar thermal collectors, compressor and pump are modeled analogously to hybrid 1.

For both the reference cycle and the vapor compression sub-cycle of the mechanical sub-cooling cycle, the compressor outlet and thus gas-cooler inlet pressure are optimized with respect to the  $COP$ , as shown in figure 5.5. The influence of the gas-cooler pressure on the  $COP$  of a R744 vapor compression cycle can be seen in appendix G.

### 6.3.1 Influence Ambient Temperature on COP MSC

In figures 6.10 through 6.12, the  $COP$  of the MSC can be seen in relation to the ambient temperature, for three levels of solar irradiance ( $G = 600, 900$  and  $1200\text{ } \frac{W}{m^2}$ , respectively). To attain these results, the area of solar panels was fixed at  $20\text{ } m^2$  and the cooling load was fixed at  $5\text{ } kW$ . As mentioned before, the pressure in the gas-cooler was optimized.

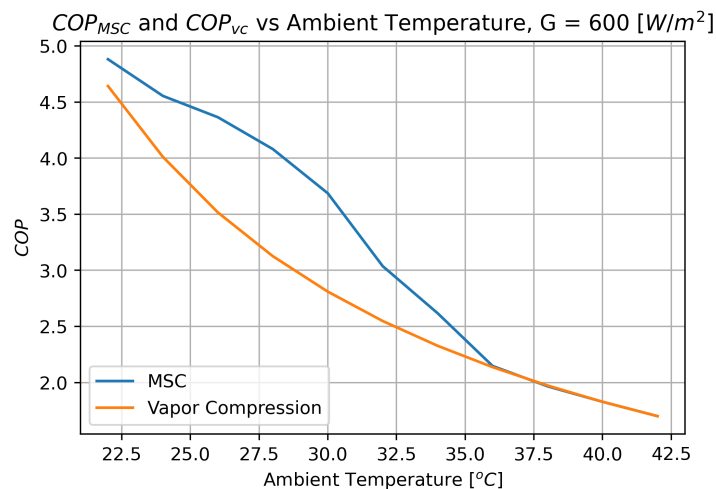


Figure 6.10:  $COP_{MSC}$  and  $COP_{vc}$  vs ambient temperature,  $G = 600\text{ } [W/m^2]$ .

Figure 6.10 displays the  $COP$  of the MSC versus the ambient temperature with a constant solar irradiance of  $600\text{ } \frac{W}{m^2}$  and the  $COP$  of a vapor compression cycle for reference. Between an ambient temperature of  $22$  and  $36\text{ } ^\circ C$ , the difference between the  $COP$  of the MSC and the reference cycle can be seen to increase and decrease again. At temperatures of  $36\text{ } ^\circ C$  and higher, the  $COP$  of the MSC is equal to the reference  $COP$ .

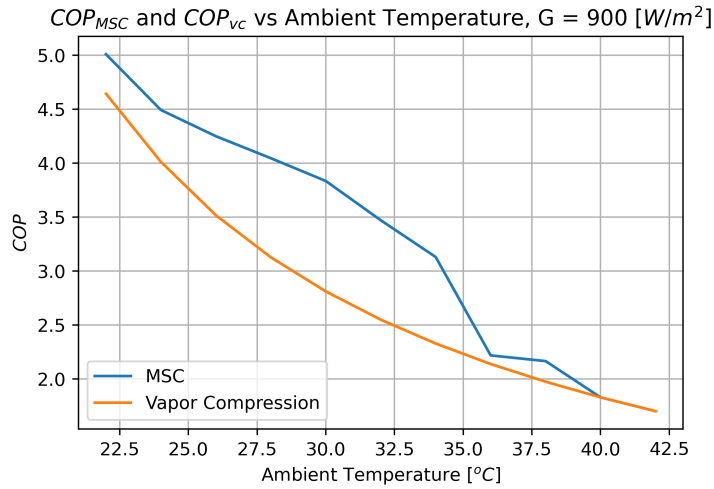


Figure 6.11:  $COP_{MSC}$  and  $COP_{vc}$  vs ambient temperature,  $G = 900 [W/m^2]$ .

Figure 6.11 shows the COP of the MSC versus the ambient temperature with a constant solar irradiance of  $900 \frac{W}{m^2}$  and the COP of a vapor compression cycle for reference. The COP of the MSC remains higher than the reference COP up until  $T_{air} = 38 \text{ }^\circ C$ , thereafter it decreases and becomes equal to the reference COP for increasing ambient temperature.

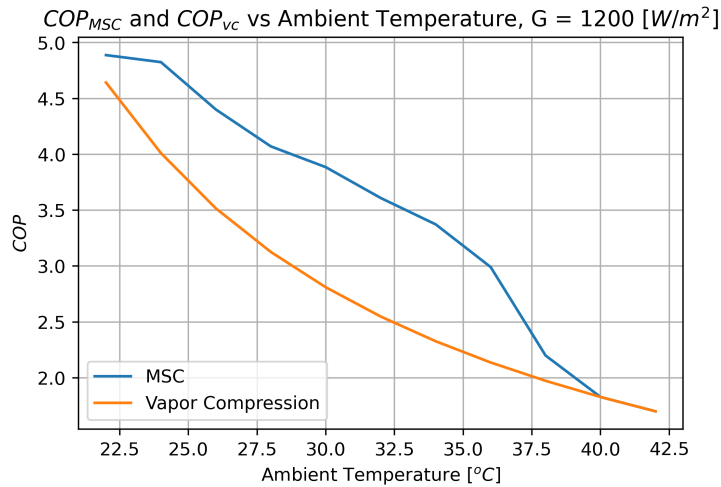


Figure 6.12:  $COP_{MSC}$  and  $COP_{vc}$  vs ambient temperature,  $G = 1200 [W/m^2]$ .

Figure 6.12 shows the COP of the MSC versus the ambient temperature with a constant solar irradiance of  $1200 \frac{W}{m^2}$  and the COP of a vapor compression cycle for reference. The difference between the COPs of the cycles increases for increasing ambient temperature, up until an ambient temperature of  $40 \text{ }^\circ C$ . At  $T_{air} = 40$  and  $42 \text{ }^\circ C$  the COP of the MSC is equal to the reference COP.

### 6.3.2 Hourly Coefficient of Performance MSC

The hourly coefficient of performance of the mechanical sub-cooling cycle for the four locations can be seen in figures 6.13a through 6.13d. The COPs were calculated for a fixed solar panel area of  $20 \text{ m}^2$  and cooling load of  $5 \text{ kW}$ .

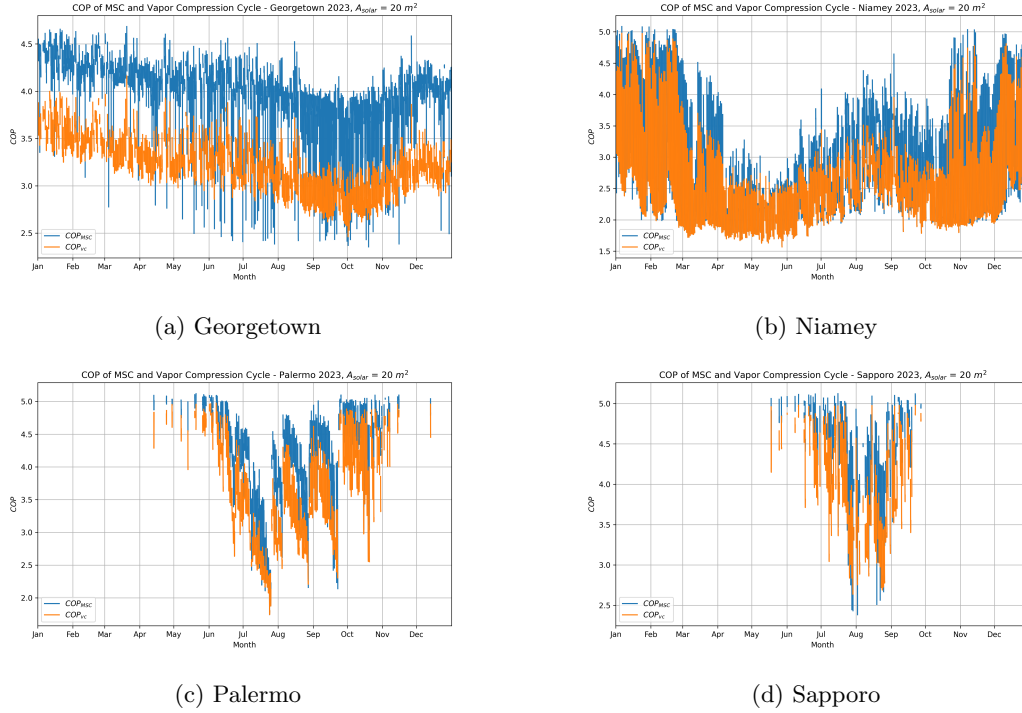


Figure 6.13: Hourly COP in MSC for all four locations.

Opposite to the results found for hybrid 1, the MSC displays COPs below the reference COP for some hours. This occurs in all four locations, but is most pronounced in Georgetown (figure 6.13a) between May and November. In all locations, the MSC shows a higher COP than the reference COP in the majority of the hours. Table 6.10 provides insight into the average COP of both the reference cycle and the MSC, and the highest and lowest COP achieved by the MSC for all locations.

Location	Average $COP_{vc}$	Average $COP_{MSC}$	Highest $COP_{MSC}$	Lowest $COP_{MSC}$
Georgetown	3.18	3.98	4.68	2.35
Niamey	2.42	2.80	5.08	1.57
Palermo	3.50	4.15	5.12	1.74
Sapporo	3.85	4.42	5.12	2.38

Table 6.10: Average COP vapor compression and average, highest and lowest COP MSC.

### 6.3.3 Seasonal Coefficient of Performance MSC

The SCOP of the MSC in the four geographical locations can be seen in table 6.11 and figure 6.14. An increase in SCOP for increasing solar panel area can be seen across all of the locations between  $A_{solar} = 5$  and  $50 \text{ m}^2$ . A decrease in SCOP is visible between  $A_{solar} = 2$  and  $5 \text{ m}^2$  for all locations.

Location	$SCOP_{vc}$	$SCOP_{MSC}$ $A_{solar} = 2 \text{ m}^2$	$SCOP_{MSC}$ $A_{solar} = 5 \text{ m}^2$
Georgetown	3.15	3.19 (+1.27%)	3.04 (-3.49%)
Niamey	2.30	2.31 (+0.43%)	2.30 (+0%)
Palermo	3.34	3.40 (+1.80%)	3.38 (+1.20%)
Sapporo	3.75	3.84 (+2.40%)	3.81 (+1.60%)
Location	$SCOP_{MSC}$ $A_{solar} = 10 \text{ m}^2$	$SCOP_{MSC}$ $A_{solar} = 20 \text{ m}^2$	$SCOP_{MSC}$ $A_{solar} = 50 \text{ m}^2$
Georgetown	3.48 (+10.5%)	3.94 (+25.1%)	4.28 (+35.6%)
Niamey	2.34 (+1.74%)	2.56 (+11.3%)	2.90 (+26.1%)
Palermo	3.68 (+10.2%)	4.01 (+20.1%)	4.27 (+27.8%)
Sapporo	4.06 (+8.27%)	4.36 (+16.3%)	4.54 (+21.1%)

Table 6.11: Seasonal coefficient of performance MSC

Table 6.12 displays the SCOP of the MSC with a multi-ejector design consisting of 4 instead of 7 ejectors. A decrease in SCOP with respect to the corresponding SCOP of the 7 ejector design is visible for all values.

Location	$SCOP_{vc}$	$SCOP_{MSC}$ $A_{solar} = 2 \text{ m}^2$	$SCOP_{MSC}$ $A_{solar} = 5 \text{ m}^2$
Georgetown	3.15	3.22 (+2.22%)	3.24 (+2.86%)
Niamey	2.30	2.31 (+0.43%)	2.31 (+0.43%)
Palermo	3.34	3.46 (+3.59%)	3.48 (+4.19%)
Sapporo	3.75	3.93 (+4.80%)	4.00 (+6.67%)
Location	$SCOP_{MSC}$ $A_{solar} = 10 \text{ m}^2$	$SCOP_{MSC}$ $A_{solar} = 20 \text{ m}^2$	$SCOP_{MSC}$ $A_{solar} = 50 \text{ m}^2$
Georgetown	3.12 (-0.95%)	3.18 (+0.95%)	4.02 (+27.6%)
Niamey	2.30 (+0.00%)	2.34 (+1.74%)	2.57 (+11.7%)
Palermo	3.38 (+1.20%)	3.54 (+5.99%)	4.03 (+20.7%)
Sapporo	4.04 (+7.73%)	3.93 (+4.80%)	4.41 (+17.6%)

Table 6.12: Seasonal coefficient of performance MSC with 4 ejectors

In figure 6.14, the evolution of the SCOP can be seen, showing the initial decrease and subsequent increase in SCOP for increasing areas of solar panels. An increase of the SCOP with respect to the reference vapor compression cycle is also visible. The SCOPs of the MSC for Georgetown, Palermo and Sapporo all fall between 3.15 and 4.54, while Niamey shows lower SCOPs for the MSC across all values for  $A_{solar}$ , falling between 2.30 and 2.90.

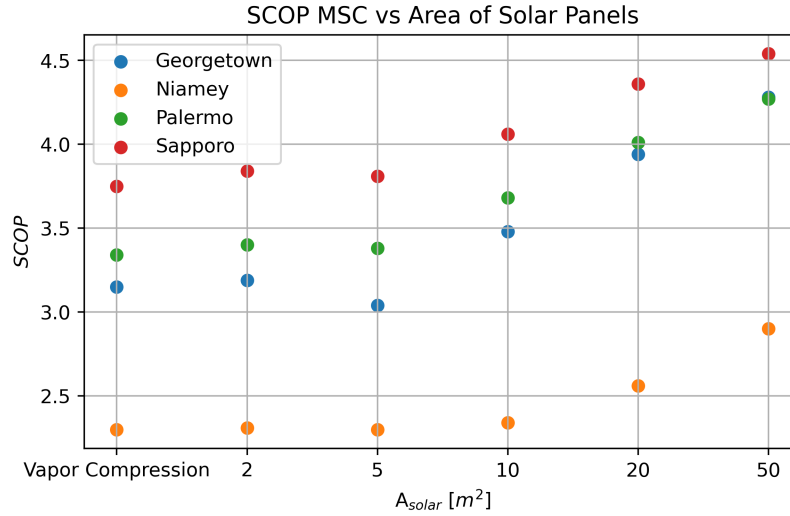


Figure 6.14: SCOP MSC vs area of solar panels.

### 6.3.4 Cooling Surplus MSC

Opposite to the results of hybrid 1 presented in section 6.2.5, the MSC has a success rate of 100% since its ability to cool is not dependent on ambient conditions. Its configuration however can lead to a surplus of cooling in the mechanical sub-cooling heat exchanger. In this case, heat from the  $CO_2$  in the vapor compression cycle is extracted by evaporation in the ejector cycle until it reaches the limit for effective heat transfer (see section 3.4). Table 6.13 gives insight into how many of the operating hours of the MSC, this limit is reached.

Location	Hours Above Threshold	Hours Surplus $A_{solar} = 2 m^2$	Hours Surplus $A_{solar} = 5 m^2$
Georgetown	2793	0 (0%)	0 (0%)
Niamey	3032	0 (0%)	0 (0%)
Palermo	1309	0 (0%)	0 (0%)
Sapporo	579	0 (0%)	0 (0%)
Location	Hours Surplus $A_{solar} = 10 m^2$	Hours Surplus $A_{solar} = 20 m^2$	Hours Surplus $A_{solar} = 50 m^2$
Georgetown	0 (0%)	0 (0%)	1638 (58.7%)
Niamey	0 (0%)	2 (0.07%)	511 (16.9%)
Palermo	0 (0%)	85 (6.49%)	803 (61.3%)
Sapporo	8 (1.38%)	21 (3.63%)	308 (53.2%)

Table 6.13: Hours ejector cycle provides surplus of cooling.

Between values of 2 and 5  $m^2$  for  $A_{solar}$ , no hours occur wherein the cooling capacity generated by the upper cycle exceeds the thermal load that the lower cycle is capable of absorbing. For  $A_{solar} = 10 m^2$ , Sapporo shows 8 hours where the ejector cycle produces a surplus of cooling. For 50  $m^2$  of solar panel area, all locations display hours with a cooling surplus.

### 6.3.5 Ejector Performance MSC

In figure 6.15, the distribution and average of the ejector efficiencies achieved by the MSC in the four geographical locations can be seen.

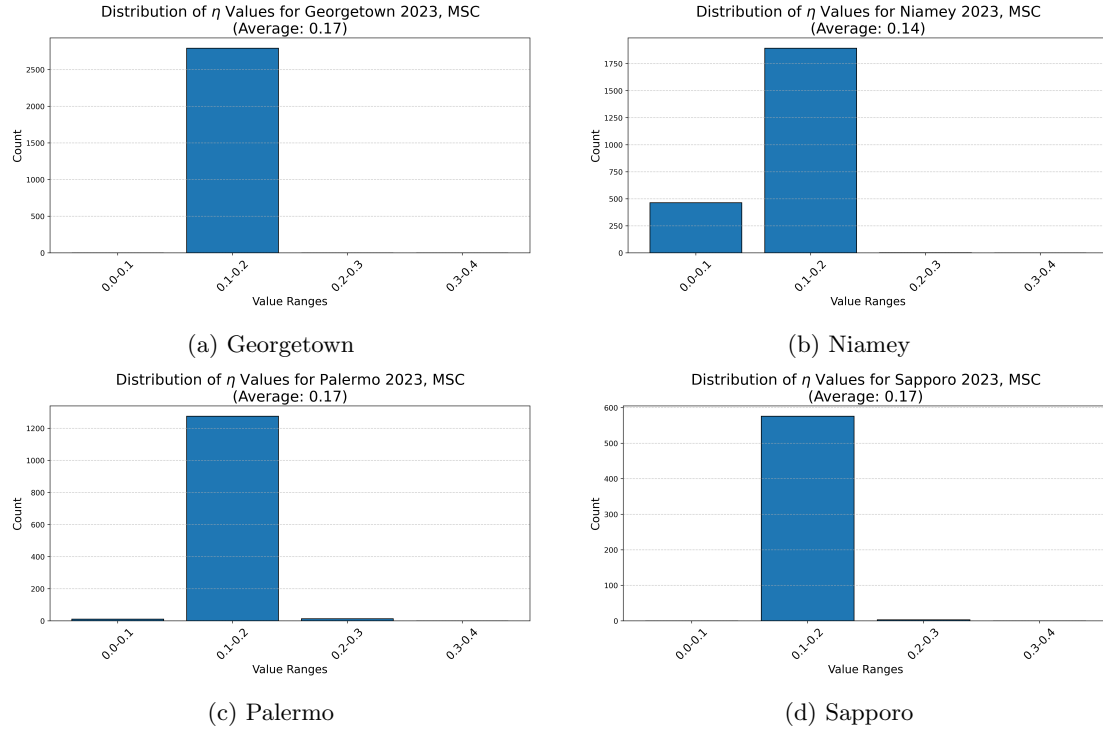


Figure 6.15: Distribution and average of achieved ejector efficiencies  $\eta_{ejector}$  in MSC for all four locations.

From figure 6.15 it can be seen that that the overall ejector efficiencies  $\eta_{ejector}$  fall between 0 and 0.3 for all locations. For Georgetown (figure 6.15a), all achieved efficiencies are in the range between 0.1 and 0.2. Sapporo (figure 6.15d) has all achieved efficiencies are between 0.1 and 0.3. Niamey (figure 6.15b) shows the most even spread between efficiencies that fall into the 0-0.1 and 0.1-0.2 range. Palermo (6.15c) shows efficiencies in all three ranges (0-0.1, 0.1-0.2, 0.2-0.3). Table 6.14 provides insight into the average, highest and lowest value of  $\eta_{ejector}$  in the four seasonal simulations. As can be seen in table 6.14, the maximum achieved ejector efficiency close to 0.2 for all locations. The averages of Georgetown, Palermo and Sapporo are all close to 0.17.

Location	Average $\eta_{ejectorMSC}$	Highest $\eta_{ejectorMSC}$	Lowest $\eta_{ejectorMSC}$
Georgetown	0.167	0.198	0.144
Niamey	0.144	0.203	0.090
Palermo	0.165	0.209	0.095
Sapporo	0.168	0.206	0.140

Table 6.14: Average, highest and lowest  $\eta_{ejector}$  MSC.

In figure 6.16, the distribution and average of the entrainment ratios  $\gamma$  can be seen for the four geographical locations.

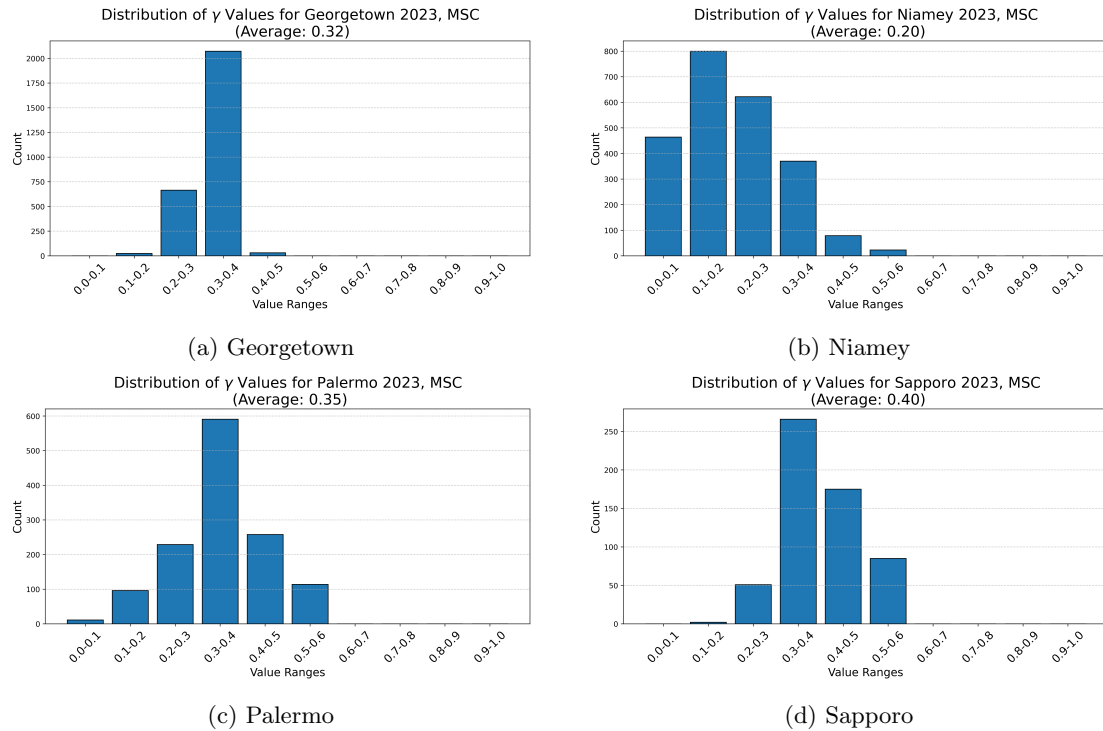


Figure 6.16: Distribution and average of  $\gamma$  in MSC.

Figure 6.16 displays a spread of entrainment ratios between 0 and 0.6 for Niamey and Palermo (figures 6.16b and, 6.16c), this range is smaller for Georgetown (figure 6.16a) and Sapporo (figure 6.16d) at 0.1-0.5 and 0.1-0.6, respectively. The largest share of values for  $\gamma$  falls in the 0.1-0.2 range for Niamey, whilst Georgetown, Palermo and Sapporo display the highest share of  $\gamma$  values between 0.3 and 0.4. Table 6.15 shows the average, highest and lowest values for  $\gamma$  across the four locations. The highest entrainment ratio across the four locations is 0.542, displayed in Palermo and Sapporo. Sapporo shows the highest average entrainment ratio at 0.401, conversely Niamey has the lowest average entrainment ratio at 0.203.

Location	Average $\gamma$	Highest $\gamma$	Lowest $\gamma$
Georgetown	0.322	0.465	0.161
Niamey	0.203	0.532	0.068
Palermo	0.353	0.542	0.073
Sapporo	0.401	0.542	0.171

Table 6.15: Average, highest and lowest  $\gamma$  MSC.

## 6.4 Multi Ejector Design

In table 6.16, the optimized throat diameters, maximum achievable throat area and number of possible unique areas (combinations) can be seen for an array of 4, 5, 6 and 7 ejectors. It is important to note that the geometry of all ejectors is the same in the sense that the ratio between  $D_t$  and all other relevant dimensions ( $D_a$ ,  $D_{mix}$ ,  $L_{mix}$ ,  $D_d$ ) is the same across all ejectors in the array. In this research  $\frac{D_a}{D_t}$  is 1.5,  $\frac{D_{mix}}{D_t}$  is 1.8,  $\frac{D_d}{D_t}$  is 4 and  $\frac{L_{mix}}{D_{mix}}$  is 10.

Number of Ejectors	Optimized Ejector Throat Diameters $D_t$ (mm)	Maximum Area (mm <sup>2</sup> )	Combinations
4	0.50, 1.52, 2.34, 3.35	15.13	15
5	0.50, 1.11, 1.52, 2.34, 3.15	15.08	31
6	0.50, 0.71, 1.11, 1.52, 2.34, 3.15	15.50	63
7	0.50, 0.71, 0.91, 1.32, 1.73, 2.54, 3.56	19.95	127

Table 6.16: Ejector configurations and achievable effective throat areas.

In figure 6.17 the distribution of all achievable area's can be seen for the array of 4, 5, 6 and 7 ejectors. For 4 through 6 ejectors, larger gaps between the achievable areas are visible, while using 7 ejectors results in a more dense spread of the effective ejector throat areas.

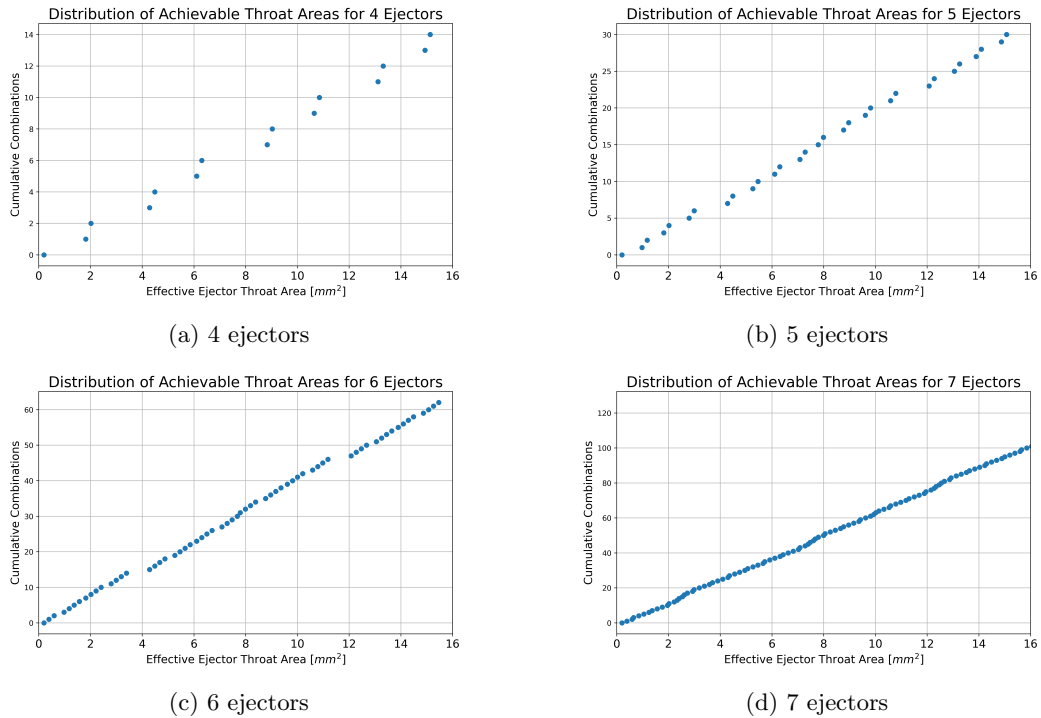


Figure 6.17: Distribution of achievable ejector throat areas for 4, 5, 6 and 7 ejectors in parallel.

## 6.5 Economic Analysis

In this section, the results of the economic analysis can be seen for both cycles. The economic analysis includes a conventional vapor compression cycle with R290 as the working fluid, hybrid 1 with a solar panel area of  $25 \text{ m}^2$  and R290 as the working fluid, a R744 vapor compression cycle and the MSC with a solar panel area of  $20 \text{ m}^2$  and a combination of R290 and R744.

### 6.5.1 Capital Costs

The capital costs for the 4 cycles in the economic analysis can be seen in table 6.17. The required size of the individual components is based on the maximum across the reviewed locations.

Component	R290 Conventional (EUR)	Hybrid 1 $A_{solar} = 25 \text{ m}^2$ (EUR)	R744 Conventional (EUR)	MSC $A_{solar} = 20 \text{ m}^2$ (EUR)
Compressor	735	735	1286	1286
Evaporator	805	805	805	805
Condenser	4500	9700	5100	11000
Solar Thermal Collectors	0	2813	0	2250
Pump	0	305	0	305
Multi- Ejector	0	235	0	235
Internal Heat Exchanger	0	0	0	1220
<b>Total</b>	<b>6045</b>	<b>14593 (+8548)</b>	<b>7191</b>	<b>16201 (+9010)</b>

Table 6.17: 2023 capital costs of two reference cycles, hybrid 1 and the MSC.

### 6.5.2 Operational Costs

As explained in section 5.5, the operational costs are calculated by multiplying the seasonal energy consumption with the electricity prices. Table 6.18 presents the 2023 operational cost of the 4 refrigeration cycles across the four locations. The annual savings in EUR achieved by hybrid 1 and the MSC can be seen in parentheses.

Location	R290 Vapor Compression (EUR)	Hybrid 1 $A_{solar} = 25 \text{ m}^2$ (EUR)	R744 Vapor Compression (EUR)	MSC $A_{solar} = 20 \text{ m}^2$ (EUR)
Georgetown	475	443 (-32)	1375	1099 (-276)
Niamey	259	252 (-7)	791	711 (-80)
Palermo	118	105 (13)	314	261 (-53)
Sapporo	59	54 (-5)	154	132 (-22)

Table 6.18: 2023 operational costs of two reference cycles, hybrid 1 and the MSC for reviewed locations.

---

In this chapter, the different aspects and results of this research will be evaluated and discussed. The discussion is divided between the developed ejector models, the conventional air conditioning baseline, the two simulated refrigeration cycles, the multi-ejector design and finally the technoeconomic analysis.

## 7.1 Ejector Model

Two thermodynamic ejector models were created based on conservation laws (model 1) and a combination of conservation laws and mach relations (model 2). Model 1 was created based on a 2016 ejector model presented by Ma et al. [44]. The validation of model 1 in section 4.2.2 showed good agreement to experiments by Garcia del Valle et al. [81] (maximum absolute error 1.57 °C) but relatively large absolute errors compared to experiments by Jia and Wenjian [82] (up to 27.68 °C). As stated in the validation, these large errors might be attributed to the lack of diffuser diameter in the experiments by Jia and Wenjian. A big limitation of the first ejector model is the requirement of the mass entrainment ratio  $\gamma$ , to resolve this limitation, the second ejector model was created, based on a 2024 ejector model presented by Mastrowski et al. [45]. The second model was validated in section 4.3.2, showing improved agreement with regard to diffuser outlet pressure for both experimental datasets. The second model was able to capture the relation between the diffuser outlet pressure and the mass entrainment ratio well, compared to experiments by Mastrowski et al. (average error 5.86%). This absolute average error of 5.86%, is slightly higher than the error of "less than 4%" in mass entrainment ratio prediction presented by Kumar and Ooi [46]. The maximum error of 18.11% is in line with the the accuracy of the model by Mastrowski et al. which had reported errors between 14.2% and 26.1%. The second ejector model can however output unrealistic ejector efficiencies, a short analysis on this was presented in section 4.3.3. These unrealistic results might be explained by the way that the second ejector model treats the relationship between the entrainment ratio and the hypothetical throat pressure. The adjustment of the hypothetical throat pressure based on the diffuser outlet pressure has no physical physical fundament other than the relation between the hypothetical throat pressure and the entrainment and ejector outlet pressure. This therefore should be viewed as a correlation instead of a physical mechanism. Within the bounds of this correlation, the model yields usable results. Outside these limits, the ejector model reports unrealistically high overall efficiencies up to 0.40, 60% higher than values found in literature as reported in section 3.2. This limits the applicability of the ejector model to conditions where the primary pressure is high compared to the secondary pressure.

## 7.2 Vapor Compression Cycle with PV Panels

The seasonal simulation of a vapor compression cycle air conditioner paired with photovoltaic panels was created to function as a baseline, and put the results of the solar ejector refrigeration cycles into perspective. Through the seasonal solar energy generation and air conditioner energy consumption, these results also give insight to the solar irradiance and temperature throughout the season in the four locations. In Georgetown, a high solar irradiance can be seen throughout

the year with moderate temperatures. Niamey shows high solar irradiance and high temperatures. Palermo shows very high solar irradiance with moderate temperature with high temperature spikes and Sapporo displays moderate solar irradiance and temperatures. These varying results are in line with expectations based on weather data for the locations as presented in section 5.5. This data simplifies interpreting the results of the simulations of the solar ejector refrigeration cycles and therefore is a vital part of the research. The result that solar panels can generate sufficient or more electrical energy than consumed by the air conditioning system is in line with findings in literature [114], however, the surplus of energy is very large (1 to 3 times the air conditioner energy consumption). This might be caused by the assumptions for the insulation of the cooled space and neglecting the implications of short term energy storage, which is shown to have an effect on a PV-driven air conditioning system in real life [115].

### 7.3 Hybrid 1

In section 6.2.1, the COP of hybrid 1 was found to decrease for increasing secondary flow pressure. This is explained by the working of the compressor. At higher secondary inlet pressures, the compressor puts in more work, and thus consumes more energy. The cooling load however is not directly increased for an increased secondary pressure. Therefore, the lowest secondary pressure that still allows sufficient entrainment for operation in the ejector corresponds to the highest COP. The indication that the compressor work is critical for the COP is in line with expectations. In section 6.2.2 the influence of the ambient temperature on the COP of hybrid 1 was presented for three different values of solar irradiance. In line with expectations and the reference cycle, the COP decreased for increasing ambient temperatures, explained by the increased condenser pressure and resulting compressor work. Instances where the COP of hybrid 1 is below that of the reference cycle can be explained by a combination of solar irradiance and ambient temperature that results in decreased compressor work in hybrid 1, but higher total work input as a result of the pump. At the highest reported temperature (42 °C), only the highest value of solar irradiance ( $1200 \frac{W}{m^2}$ ) results in a COP higher than that of the reference cycle. This result is expected as a cooling load lower than required results in failure of the ejector refrigeration cycle. At higher solar irradiance, the generator allows more mass flow, which allows the high evaporative cooling load that needs to be achieved for high ambient temperatures.

In the seasonal simulation of hybrid 1, the average COPs found for the reference vapor compression cycle show good agreement to values found in literature. Average reference COPs between 4.53 and 6.24 were found, against values between 4.1 and 5.3 in literature [116]. The hourly COPs show a similar evolution as the reference COP, displaying high values in months with relatively low ambient temperatures and a sharp decrease in COP in hot months. The SCOP values are lower than the average COP. This is to be expected as the contribution of the hourly COP to the average is equal for every hour, whereas the contribution to the SCOP is weighted by the cooling load of the corresponding hour. The increase in SCOP for increasing solar panel area could be explained by the increase in primary mass flow, resulting in more hours where hybrid 1 can match the cooling duty. This explanation is supported by the success rate of hybrid 1 which is shown to increase for increasing  $A_{solar}$ . Validating the values for COP and SCOP is difficult since no similar cycles that use R290 are found in literature.

In a configuration with  $A_{solar} = 25 m^2$ , using an array of 4 instead of 7 ejectors showed an average decrease in SCOP value of 0.31 or 5.3%. This substantial decrease is in line with expectations and literature. A seasonal COP decrease of 5.6% between 7 and 4 ejectors in a multi-ejector

system was reported by Aligolzadeh et al. in 2019 [117]. A decrease in SCOP with less ejectors might be caused by the relatively big gaps between effective throat areas. Since the ejector selection is based on maximizing the generator mass flow, the generator and primary pressure has to be decreased, resulting in less pressure lift by the ejector. This increases the booster work and decreases the success rate, both negatively affecting the SCOP. The success rate of hybrid 1 increases with declining ambient temperature, from Niamey (highest average temperature) to Sapporo (lowest). This trend might be due to the generator's pressure limit and the elevated lower limit of condenser pressure at higher temperatures. Model 2 validation experiments confirm that diffuser outlet pressure depends on primary pressure. Since primary pressure is constrained, ejector failure hours increase in hotter climates due to insufficient refrigerant pressurization in the condenser.

Regarding the ejector performance in the seasonal simulations of hybrid 1, the entrainment ratios and ejector efficiencies are mostly in line with results found and accepted in literature, presented in section 3.2. Entrainment ratios never go above 0.714 for 3 out of 4 locations. Overall efficiencies are all below 0.2 on average, showing a maximum of 0.248, below the maximum of 0.25 found by Chen et al. in 2014 [30]. The average efficiency values of around 0.15 are below the constant value of 0.20 assumed by Hafner et al. for a multi-ejector refrigeration system [31]. The highest achieved entrainment ratio of 0.998 is higher than the highest experimental value of 0.741 reported by Huang et al. for a R141b ejector [34]. The corresponding ejector efficiencies however are below 0.05, indicating very little pressure lift in these instances. This means the hypothetical throat pressure is very low compared to the secondary pressure, resulting in high entrainment. Also, the share of these high entrainment ratio is less than 1.3%, limiting their influence on the SCOP calculations. The combination of the similarity to efficiency values found in literature and small influence of deviating entrainment ratios indicates plausible results for the hourly calculations and therefore seasonal results.

The results of hybrid 1 were created without considering the implications of a varying mass flow and outlet pressure in the compressor. As explained in section 3.8, inverter compressors can vary their mass throughput and pressure between a certain range. For hybrid 1, the compressor power is considered to be ideal, meaning a x-fold decrease in mass throughput or pressure increase leads to a x-fold decrease in energy used by the compressor. In actuality, the efficiency of inverter compressors is nonlinear [118]. Also, the minimum cooling load in the simulations is dictated by the difference between a fixed indoor temperature, while in actuality, the indoor temperature comfort range is dependent on the outdoor temperature [119]. Another remark regarding the cooling load is the simplicity of its calculation. The cooling load per hour was calculated assuming only heat transfer through conduction result from the temperature difference between the cooled space and the ambient. Determining the cooling load more accurately could yield improved accuracy, in particular in the success rate of hybrid 1.

## 7.4 Mechanical Sub-Cooling Cycle

The results of the single case simulations of the mechanical sub-cooling cycle, presented in section 6.3.1, show decreasing COPs for increasing ambient temperature and increasing COPs for increasing solar irradiance, in line with findings by Yadav and Sarkar [57]. This might be explained by the condenser pressure, which is coupled to both the ambient temperature and the total evaporative cooling load in the internal heat exchanger (HEX). The evaporative cooling load is dictated by the mass flow, which in turn dictated by the solar irradiance. The SCOPs of

the MSC are lower than the average COPs, explained by the same mechanism as in hybrid 1. In all locations, the SCOP of the MSC is found to increase for increasing solar panel area, except for the solar panel area of  $5 \text{ m}^2$ . This could be caused by the fact that  $A_{solar} = 5$  leads to hours where the sub-cooling achieved by the ejector cycle is outweighed by the power consumption of the pump, resulting in a lower COP.  $A_{solar} = 2$  does not present a decrease in SCOP with respect to the vapor compression cycle, indicating that the relation between the evaporative cooling load in the heat exchanger and the power consumption of the pump is nonlinear. In literature, values between 30% and 50% are reported for the increase in COP for transcritical R744 cycles with dedicated mechanical sub-cooling [120]. The results of the MSC simulation are in line with these findings, showing a maximum increase of 35.6%.

Regarding the solar panel area effect on the SCOP,  $10 \text{ m}^2$  leads to the highest increase in SCOP divided by the area of solar panels in square meters, for Palermo and Sapporo. This optimum lies at  $20 \text{ m}^2$  for Georgetown and Niamey. Combining this with the weather data presented in table 5.2, indicates a higher  $A_{solar}$  is beneficial in hotter climates. This is to be expected because of the increased  $\Delta T$  and thus heat transfer in the internal heat exchanger (HEX) at higher ambient temperatures. The fact that no location displays the optimum at  $50 \text{ m}^2$  could be explained by the share of hours of cooling surplus, which ranges between 16.9% and 61.3% for  $A_{solar} = 50 \text{ m}^2$ , indicating a high share of hours where part of the energy consumption of the pump is not translated to enhanced cooling in the evaporator. The effect of using an array of 4 ejectors instead of 7 ejectors is higher in the MSC, compared to hybrid 1. For a solar panel area of  $20 \text{ m}^2$ , an average decrease of 0.47 or 12.6% was reported. This might be explained by the fact that the generator pressure is lowered as a result of the ejector selection. The COP of the sub-cooling cycle decreases for decreasing generator pressure, finally resulting in a decreased SCOP of the MSC. This suggests an imbalance between the two sub-cycles, which is expected for a decrease in COP of the sub-cooling cycle. The findings regarding the design with fewer ejectors indicate the critical implications of the varying mass flow associated with a solar thermal collector.

The ejector performance in the simulations conducted for the MSC shows good agreement to values found in literature, with the highest average value for the overall ejector efficiency being below 0.17. Also, the highest maximum value found in the simulations is below 0.22 found by Nakagawa et al. [29] and Lucas and Köhler [28]. Furthermore, the entrainment ratios achieved in the mechanical sub-cooling cycle show accordance with literature, displaying average values below 0.45, similar to values found in literature [121].

In the MSC simulations, a fixed secondary inlet temperature of  $20 \text{ }^\circ\text{C}$  is assumed in the ejector cycle. In reality, this would be dictated by the heat transfer in the heat exchanger between the sub-cycles. In this research the subsequent assumption is made that if the evaporation in the ejector cycle has a higher heat capacity than the heat rejection by vapor compression cycle, evaporation of the working fluid in the ejector cycle is ensured by heat from the ambient, because the thermodynamic ejector model requires and therefore assumes complete evaporation. As stated in section 3.4, a temperature difference between the refrigerant and the ambient of 5 K is maintained throughout this research, consistent with previous research by Cheng et al. [91]. This however might be too small of a difference to ensure sufficient heat transfer in the heat exchangers, evaporators and condensers under real-world circumstances.

Comparing the two solar ejector refrigeration cycles leads to notable findings, particular regarding the reported SCOPs. A solar panel area of  $20 \text{ m}^2$  for the MSC resulted in lower SCOPs than a solar panel area of  $5 \text{ m}^2$  for every location. Compared to the R290 vapor compression (reference)

cycle for hybrid 1, the MSC with  $A_{solar} = 20 \text{ m}^2$  achieved a 42.9% lower SCOP on average. The highest tested solar panel area for the MSC ( $50 \text{ m}^2$ ) also displayed lower SCOPs than the R290 reference cycle and hybrid 1 paired with the smallest solar panel area. Although the cooling load of hybrid 1 varies per hour and the cooling load of the MSC is fixed at  $5 \text{ kW}$ , these results are still comparable because of the way the SCOP is defined.

## 7.5 Multi Ejector Design

Regarding the multi ejector design presented in section 5.4 with its results shown in section 6.4, uncertainty arises from the combination of high pressures and small ejector diameters. Although, as mentioned in section 3.1.3, ejectors with a throat diameter of 0.5 millimeters exist, no ejectors with such a throat diameter currently exist with a pressure rating above 5 bar [24]. Also the splitting and subsequent mixing of the inlet and outlet flows in the ejector array of ejectors is assumed to have no effect on the ejector operation and inlet and outlet states. Instead, it is modeled as a single ejector with geometry corresponding to the effective throat area achieved by a combination of ejectors. In the simulations of both cycles, the ejector selection is based on an iterative process where the primary mass flow, which is dictated by the ejector size and pressure, is used to calculate the optimum ejector size. In a real refrigeration cycle, the ejector size could only be controlled by the primary inlet conditions and mass flow. This could result in less optimal ejector selection compared to the process used to attain the results in this research.

## 7.6 Economic Analysis

From the economic analysis, it can be concluded that neither hybrid 1 nor the MSC are economically viable in the way they are presented in this research. Break-even times would be multiple hundred years, far beyond the typical lifespan of residential refrigeration systems [122]. Changing the solar thermal collectors to PVT panels, would bring this down considerably, virtually omitting operational costs. This would however decrease the SCOP because of the lower thermal efficiency of PVT panels compared to the flat plate collectors used in the simulations, as indicated in section 3.6.4. Changing the heat source of the generator to geothermal heat or process waste heat could also increase the economic viability.

For both the capital and operational costs, assumptions were made to attain the results. For the operational costs, electricity prices were informed by historical data. Electricity prices are known to be subject to geopolitical dynamics, economic trends, policy changes, and market behaviors, and therefore a large uncertainty stems from assuming a fixed electricity price in the operational costs calculation, since sudden drops or spikes are to be expected. For the capital costs, the largest uncertainty stems from the LMTD area calculations. For the evaporator, the hot side temperature is assumed to decrease from  $12 \text{ }^\circ\text{C}$  to  $7 \text{ }^\circ\text{C}$ , based on chilled water systems in literature [123]. The evaporating refrigerant is at a constant  $0 \text{ }^\circ\text{C}$  and the U value is assumed to be  $800 \frac{\text{W}}{\text{m}^2 \cdot \text{K}}$  [124]. For the air-cooled condenser and gas-cooler, the U value is assumed to be  $150 \frac{\text{W}}{\text{m}^2 \cdot \text{K}}$  [124]. In the condenser, the refrigerant is assumed to be constant at 5 K above the ambient. In the gas-cooler, a temperature decrease of 2 K is assumed. The condenser is assumed to increase the air temperature by 1 K. Also, the CEPCI is used to adjust prices between 2004 and 2023, while The CEPCI is recommended for use in spans of 5 years or less due to "changes in technology, construction practices, labor efficiency, and formulation of the index" [105]. These factors decrease the accuracy of the economic analysis substantially.

# Conclusion and Recommendations

---

## Conclusion

This research presented two main objectives in chapter 2; to develop a steady-state thermodynamic ejector model, and to develop and optimize a sustainable solar ejector refrigeration cycle. The sub-topics of the first research objective were to examine the effects of varying geometry and back pressure on the thermodynamic ejector model. For the optimization and development of the ejector refrigeration cycles, the 3 sub-topics were; testing ejector refrigeration cycles with different configurations, study the feasibility of using R744 or similar sustainable refrigerants in the proposed cycles and analyzing their thermodynamic performance.

Regarding the development of the thermodynamic ejector, multiple conclusions can be drawn from this research. Comparing the first and second developed ejector model, it can be concluded that a known and pre-defined entrainment ratio simplifies calculations, but severely limits applicability. Calculating the entrainment ratio based on in- and outlet leads to increased accuracy in predictions, and enables application outside conditions tested in experiments. An ejector model that requires no entrainment ratio as input is therefore more suited to be used in the simulating of refrigeration cycles. The effect of varying geometry was found to have little influence on the absolute error of the diffuser outlet pressure prediction. The entrainment ratio prediction was found to be better for  $D_{mix}$  that were larger compared to  $D_a$ . The effect of varying back pressure on the model is an important topic, because of the the inverse relation between the diffuser outlet pressure (or back pressure) and the entrainment ratio  $\gamma$ . The correlation between the outlet pressure and entrainment ratio that was integrated in the second model, lead to a mean error of 5.86% in prediction of the entrainment ratio in relation to the diffuser outlet pressure compared to experiments. Varying the back pressure thus had an inverse effect on the entrainment ratio, in line with expectations and literature. The efficiency analysis showed that the ejector model developed in this research has severe limitations in terms of inputs, and should only be used within the bounds of the model.

The development and optimization of ejector refrigeration cycles was split between the presentation of the three cycles, and subsequent optimizing and testing of 2 of those cycles in both single case and seasonal simulations. As for the tested hybrid ejector refrigeration cycle, hybrid 1, the refrigerant R290 presented SCOP increases between 4.7% and 18.7% for a solar panel area of 25  $m^2$ , indicating such a solar ejector refrigeration system would reduce energy consumption compared to a conventional vapor compression cycle with R290 as the working fluid, with a realistic area of solar panels. The largest SCOP increases were reported in Palermo and Sapporo (18.4% and 18.7%, respectively), both locations that need refrigeration only in certain months of the year. The heating that is done in the rest of the year in these locations, make solar thermal collectors suited for these locations, adding to the benefit of a solar ejector refrigeration system. The simulation of hybrid 1 proofs that with a booster-ejector configuration, a multi-ejector system can enhance the seasonal thermodynamic performance of a residential refrigeration system through the use of low-grade heat ( $< 75^\circ C$  in this research). Most importantly, the hybrid 1 simulation results validate that a booster-assisted solar ejector refrigeration cycle can operate well under real-world circumstances, using R290. This low-GWP, zero-ODP refrigerant complies with current and future regulatory standards for refrigerants.

Regarding the mechanical sub-cooling cycle, the combination of R290 and R744 presented SCOP increases between 11.3% and 25.1% for a solar panel area of  $20\text{ m}^2$ , indicating significant increase in seasonal performance achieved with a solar panel area that is attainable in real life. The mechanical sub-cooling cycle's SCOP values showed that the relation between SCOP and area of solar panels is counter-intuitive and thus should be decided based on location and weather. The use of R744 and R290 in the seasonal simulations indicates that using a sustainable refrigerant is feasible, but also highlight the low SCOPs associated with transcritical R744 refrigeration cycles. Although the dedicated mechanical sub-cooling cycle raises the COP significantly, a conventional vapor compression cycle with R290 attains a 42.9% higher SCOP across the four locations. Regarding the average increase in SCOP of 18.2% achieved by the MSC with  $20\text{ m}^2$ , it can be concluded that solar ejector refrigeration cycles are suitable for application as mechanical sub-coolers without the need for unrealistically large areas of solar panels.

Taking the results of multi-ejector design, simulation of the solar thermal collectors and literature on existing ejectors together, an important conclusion is that with currently existing ejectors, the complete solar ejector refrigeration system, in both hybrid 1 and the MSC, would have to be scaled up, in order to allow sufficiently large ejectors that allow operation at the elevated pressures in the system. This scale-up requirement limits the applicability of solar ejector refrigeration systems for residential refrigeration. Another important conclusion regarding the multi-ejector design is that the high variance in mass flow that is inherent to solar thermal collectors severely limits performance in a multi-ejector refrigeration cycle, as indicated by the SCOP decrease between the use of 7 and 4 ejectors in both hybrid 1 and the MSC.

Summarizing this concluding chapter, this research shows that thermodynamic ejector modeling with limited input parameters is complex but achievable, resulting in an ejector model that, within its limits, captures the relation between entrainment ratio and back pressure well and is usable for the simulation of refrigeration cycles. The resulting simulations of solar ejector refrigeration, both as direct source of refrigeration and as a dedicated sub-cooling cycle highlighted the feasibility and potential of such cycles, with the use of sustainable refrigerants R290 and R744. The comparative study with relevant conventional refrigeration cycles conveyed high increase in seasonal coefficient of performance and high success rates, whilst also shining light on the limitations inherent to solar ejector refrigeration including the availability of ejectors, inverter compressors, and mismatch between an ejector system and the varying mass flow characteristic of solar thermal collectors. The technoeconomic analysis proved ejector refrigeration cycles for residential space cooling require very high electricity prices to be economically viable. Taking this together, solar ejector refrigeration cycles can not be considered fit-for-purpose with respect to residential refrigeration. Instead, they show high potential and feasibility in applications where there is a constant, sustainable source of (waste) heat (e.g. process or geothermal heat), and little constraint on system size. The findings of this research justify further research into ejector refrigeration cycles for more compatible conditions.

## Recommendations

The final conclusion allows for, and leads to a number of recommendations for future research on the topic of solar ejector refrigeration cycles. The recommendations are presented in the order of topics in this research.

The thermodynamic modeling of ejectors represents a promising field of research, but it remains an underdeveloped and challenging area. Current models often struggle to accurately predict real-world performance due to significant deviations between theoretical predictions and experimental results. These discrepancies become especially pronounced when the models are applied outside the range of operating conditions or geometries for which they were initially validated. In such cases, the models can become unreliable and even unusable, especially in the absence of experimental studies conducted under similar circumstances. This absence highlights the critical need for extensive experimental research to better understand ejector performance under conditions relevant to practical, real-world refrigeration applications. Laboratory experiments that mimic operating conditions, including variations in temperature, pressure, and ejector geometry, are essential for refining existing models. The most important recommendations regarding the thermodynamic modeling of ejectors are:

- Expand experimental datasets on ejectors; by creating expansive datasets of ejector performance, future research could benefit from increased calibration and validation, ultimately increasing the accuracy and applicability of thermodynamic ejector models. Experimental studies can also shed light on phenomena that are difficult to capture in theoretical models, such as the effects of flow irregularities, turbulence, and non-ideal fluid behavior. These factors often play a significant role in ejector performance but are not (fully) accounted for in simplified thermodynamic models like the ones used in this paper. Addressing these complexities through empirical data will enable the development of more sophisticated models through for example increasingly accurate isentropic efficiencies. Specifically recommended for the field of solar ejector systems would be to intensify experimental investigations into ejector performance in conditions associated with solar-driven refrigeration systems. This could include studying the impact of varying solar thermal collector mass flow on the ejector performance.
- Improve integration of ejector model limits; in this research, outputs of the thermodynamic ejector model deemed unrealistic in terms of overall component efficiency are filtered out by means of a cut-off. In this research, this cut-off is related to the inlet pressures, which is in turn based on efficiency values found in literature. Future ejector models could benefit from integrated limits that ensure realistic output regardless of the inputs.

Regarding the seasonal simulations of hybrid 1 and the MSC, the following general recommendations could be made:

- Study dynamic behavior; by studying the dynamic behavior under changing ambient conditions, real-world performance predictions could be improved. The accuracy of the assumed performance of the solar thermal collectors, evaporator and condenser could be improved by using software like Aspen Plus, enhancing the accuracy in simulation of the complete cycle. Specifically for the MSC, dynamically adjusting the evaporator outlet temperature in the ejector cycle, based on the ambient temperature and generator pressure, would improve the results of the MSC simulation in terms of accuracy and realism.

- Use R744 or other sustainable refrigerants in the ejector cycle; in this research, the ejector cycle has been modeled with R290 exclusively. Alternative sustainable refrigerants could improve overall performance and therefore are worth exploring, especially R744, because of its zero ODP and GWP of 1. Specifically for the MSC it could yield interesting results to do simulations with one type of refrigerant instead of two. This would allow conclusions on whether a (hybrid) ejector refrigeration cycle is more suited as a direct source of refrigeration, or as a sub-cooler.
- Integrate realistic modeling of inverter compressor; as mentioned in the discussion, the realism of the compressor parameters could be improved by incorporating a model that calculates its energy consumption instead of assuming it.
- Integration of other heat sources; by modeling the ejector refrigeration cycles with different generator heat sources like photovoltaic thermal panels, or geothermal or waste heat, the performance of the ejector refrigeration cycles could improve, both in a thermodynamic and economic sense. In the case of geothermal or waste heat comparing performance with absorption refrigerators is also recommended.
- Improvement of cooling duty calculation; by expanding the calculation of the required hourly evaporative cooling load, the calculation of the success rate of hybrid 1 could be improved in terms of realism. Ideally this would include humidity effects.
- Experimental validation; through the creation of a prototype, simulation accuracy could be verified for both cycles.

Research into the implications associated with a multi-ejector design could be improved by the following recommendations:

- Research losses associated with using a multitude of ejectors instead of a single ejector; in this research, the multi-ejector is modeled as a single ejector with a throat area equal to the sum of throat areas of the selected ejectors. An experimental study could verify whether this assumption is realistic.
- Research performance with single and variable geometry ejector; a constant generator heat source could eliminate the need for a multi-ejector system and thereby decrease the complexity of the system, enhancing its viability. Variable geometry ejectors could be an alternative approach to enhance operating flexibility.

Future economic analysis of solar ejector refrigeration cycles could be improved with respect to this research, by incorporating the following recommendations:

- Realistic modeling of heat exchanger components; instead of assuming LMTD temperatures and U values, software like Aspen Plus could be used to determine the required size and resulting component costs of heat exchangers.
- Investigate effect of electricity and generator heat source on capital and operational costs; by determining the effect of using a different generator heat source or alternative source of electricity, the accuracy of the economic analysis of ejector refrigeration cycles could be improved.

In line with the conclusion of this research, the key recommendation is to intensify research into ejector refrigeration cycles operating with a continuous, sustainable source of heat for the generator. Based on this research, it would be expected that this enhances the performance of the cycles both in a thermodynamic and economic sense, but future research is needed to verify this.

# References

---

- [1] Environmental Protection Network. *Comment on Proposed Revision to Controls on Hydrofluorocarbons (HFCs)*. Sept. 2018. URL: <https://www.environmentalprotectionnetwork.org/hfc-comments/>.
- [2] NASA - GISS. “GISS Surface Temperature Analysis”. In: *GISS Surface Temperature Analysis (GISTEMP)* (2022).
- [3] E. Di Lorenzo. “Climate science: The future of coastal ocean upwelling”. In: *Nature* 518 (Feb. 2015), pp. 310–1. DOI: [10.1038/518310a](https://doi.org/10.1038/518310a).
- [4] International Energy Agency. “The Future of Cooling”. In: *The Future of Cooling - IEA* (Mar. 2018). DOI: [10.1787/9789264301993-en](https://doi.org/10.1787/9789264301993-en).
- [5] International Energy Agency. *Global Air Conditioner Stock, 1990-2050*. IEA, Paris. Licence: CC BY 4.0. 2020. URL: <https://www.iea.org/data-and-statistics/charts/global-air-conditioner-stock-1990-2050>.
- [6] International Renewable Energy Agency. “Power to heat and cooling: Status”. In: *IRENA - Power to heat and cooling* (2022). URL: <https://www.irena.org/Innovation-landscape-for-smart-electrification/Power-to-heat-and-cooling/Status>.
- [7] P. Sherman, H. Lin, and M. McElroy. “Projected global demand for air conditioning associated with extreme heat and implications for electricity grids in poorer countries”. In: *Energy and Buildings* 268 (Sept. 2022), p. 112198. DOI: [10.1016/j.enbuild.2022.112198](https://doi.org/10.1016/j.enbuild.2022.112198).
- [8] “Montreal protocol on substances that deplete the ozone layer”. In: *Documents in International Environmental Law* (May 2004), pp. 82–124. DOI: [10.1017/cbo9781139171380.010](https://doi.org/10.1017/cbo9781139171380.010).
- [9] R. J. Salawitch et al. “Twenty Questions and Answers About the Ozone Layer: 2018 Update”. In: *Scientific Assessment of Ozone Depletion: 2018* (2018), p. 84.
- [10] Council of European Union. *Council regulation (EU) no 2024/573*. <https://eur-lex.europa.eu/eli/reg/2024/573/oj>. 2024.
- [11] Ellehammer Marine Ejectors. *Ejector A-Type*. 2024. URL: <https://ironpump.com/products/ejectors>.
- [12] A. Salgado et al. “Thermal Energy Storage”. In: *Innovation Outlook* (2020). URL: <https://www.irena.org/Publications/2020/Nov/Innovation-outlook-Thermal-energy-storage>.
- [13] G. Besagni, R. Mereu, and F. Inzoli. “Ejector refrigeration: A comprehensive review”. In: *Renewable and Sustainable Energy Reviews* 53 (Jan. 2016), pp. 373–407. DOI: [10.1016/j.rser.2015.08.059](https://doi.org/10.1016/j.rser.2015.08.059).
- [14] M. Sokolov and D. Hershgal. “Enhanced ejector refrigeration cycles powered by low grade heat. Part 1. Systems characterization”. In: *International Journal of Refrigeration* 13.6 (1990), pp. 351–356. ISSN: 0140-7007. DOI: [https://doi.org/10.1016/0140-7007\(90\)90023-P](https://doi.org/10.1016/0140-7007(90)90023-P).
- [15] J. Galindo et al. “Numerical Evaluation of a solar-assisted jet-ejector refrigeration system: Screening of Environmentally Friendly Refrigerants”. In: *Energy Conversion and Management* 210 (Apr. 2020), p. 112681. DOI: [10.1016/j.enconman.2020.112681](https://doi.org/10.1016/j.enconman.2020.112681).
- [16] B. Tashtoush and Y. Nayfeh. “Energy and economic analysis of a variable-geometry ejector in solar cooling systems for residential buildings”. In: *Journal of Energy Storage* 27 (Feb. 2020), p. 101061. DOI: [10.1016/j.est.2019.101061](https://doi.org/10.1016/j.est.2019.101061).

- [17] O. Saeid et al. “Performance assessment of ammonia base solar ejector cooling system emphasizing ejector geometries: A detailed CFD analysis”. In: *Energy* 301 (Aug. 2024), p. 131770. DOI: [10.1016/j.energy.2024.131770](https://doi.org/10.1016/j.energy.2024.131770).
- [18] E. Nehdi, L. Kairouani, and M. Elakhdar. “A solar ejector air-conditioning system using environment-friendly working fluids”. In: *International Journal of Energy Research* 32.13 (Oct. 2008), pp. 1194–1201. DOI: [10.1002/er.1413](https://doi.org/10.1002/er.1413).
- [19] Advancedvacuum.se. *Steam ejectors*. URL: <https://www.advancedvacuum.se>.
- [20] Fox Venturi Products. *Venturi Ejectors for Air and Gas Applications*. 2025. URL: <https://www.foxvalve.com/air-gas-steam-vacuum-ejectors/introduction-to-air-steam-and-gas-ejectors>.
- [21] R. Yapıcı and C.C. Yetişen. “Experimental study on ejector refrigeration system powered by low grade heat”. In: *Energy Conversion and Management* 48.5 (Mar. 2007), pp. 1560–1568. DOI: [10.1016/j.enconman.2006.11.015](https://doi.org/10.1016/j.enconman.2006.11.015).
- [22] K. Chunnanond and S. Aphornratana. “Ejectors: Applications in refrigeration technology”. In: *Renewable and Sustainable Energy Reviews* 8.2 (Apr. 2004), pp. 129–155. DOI: [10.1016/j.rser.2003.10.001](https://doi.org/10.1016/j.rser.2003.10.001).
- [23] B. M. Tashtoush, M. A. Al-Nimr, and M. A. Khasawneh. “A comprehensive review of ejector design, performance, and applications”. In: *Applied Energy* 240 (2019), pp. 138–172. ISSN: 0306-2619. DOI: <https://doi.org/10.1016/j.apenergy.2019.01.185>.
- [24] Riegler & Co. KG. *Basic Ejector SBP - Silencer, nozzle size 0.5 mm*. 2024. URL: <https://www.riegler.de/de/en/basic-ejector-sbp-silencer-nozzle-size-0-5-mm-108378-1.html>.
- [25] X. Yang, X. Long, and X. Yao. “Numerical investigation on the mixing process in a steam ejector with different nozzle structures”. In: *International Journal of Thermal Sciences* 56 (2012), pp. 95–106. ISSN: 1290-0729. DOI: <https://doi.org/10.1016/j.ijthermalsci.2012.01.021>.
- [26] A. Gutiérrez and N. León. “Conceptual Development and CFD Evaluation of a High Efficiency – Variable Geometry Ejector for Use in Refrigeration Applications”. In: *Energy Procedia* 57 (2014). 2013 ISES Solar World Congress, pp. 2544–2553. ISSN: 1876-6102. DOI: <https://doi.org/10.1016/j.egypro.2014.10.265>.
- [27] J. Köhler et al. “Experimental and theoretical study of a CO<sub>2</sub> ejector refrigeration cycle”. In: *Vortrag, VDA Winter Meeting, Saalfelden*. 2007.
- [28] C. Lucas and J. Koehler. “Experimental investigation of the COP improvement of a refrigeration cycle by use of an ejector”. In: *International Journal of Refrigeration* 35.6 (2012), pp. 1595–1603. ISSN: 0140-7007. DOI: <https://doi.org/10.1016/j.ijrefrig.2012.05.010>.
- [29] M. Nakagawa, A. R. Marasigan, and T. Matsukawa. “Experimental analysis on the effect of internal heat exchanger in transcritical CO<sub>2</sub> refrigeration cycle with two-phase ejector”. In: *International Journal of Refrigeration* 34.7 (2011). Ejector Technology, pp. 1577–1586. ISSN: 0140-7007. DOI: <https://doi.org/10.1016/j.ijrefrig.2010.03.007>.
- [30] J. Chen, H. Havtun, and B. Palm. “Parametric analysis of ejector working characteristics in the refrigeration system”. In: *Applied Thermal Engineering* 69.1 (2014), pp. 130–142. ISSN: 1359-4311. DOI: <https://doi.org/10.1016/j.applthermaleng.2014.04.047>.
- [31] A. Hafner, S. Försterling, and K. Banasiak. “Multi-ejector concept for R-744 supermarket refrigeration”. In: *International Journal of Refrigeration* 43 (2014), pp. 1–13. ISSN: 0140-7007. DOI: <https://doi.org/10.1016/j.ijrefrig.2013.10.015>.

- [32] A.F.A. Elbarghthi et al. “An experimental study of an ejector-boosted transcritical R744 refrigeration system including an exergy analysis”. In: *Energy Conversion and Management* 238 (2021), p. 114102. ISSN: 0196-8904. DOI: <https://doi.org/10.1016/j.enconman.2021.114102>.
- [33] F. Liu and E. A. Groll. “Study of ejector efficiencies in refrigeration cycles”. In: *Applied Thermal Engineering* 52.2 (Apr. 2013), pp. 360–370. DOI: [10.1016/j.applthermaleng.2012.12.001](https://doi.org/10.1016/j.applthermaleng.2012.12.001).
- [34] B.J. Huang et al. “A 1-D analysis of Ejector Performance”. In: *International Journal of Refrigeration* 22.5 (Aug. 1999), pp. 354–364. DOI: [10.1016/S0140-7007\(99\)00004-3](https://doi.org/10.1016/S0140-7007(99)00004-3).
- [35] E. Ksayer. “Study and design of systems with improved energy efficiency operating with CO2 as refrigerant”. In: (Nov. 2007). URL: <https://pastel.hal.science/pastel-00625025>.
- [36] F. Liu. “Review on Ejector Efficiencies in Various Ejector Systems”. In: *International Refrigeration and Air Conditioning Conference* (2014). URL: <https://api.semanticscholar.org/CorpusID:32269694>.
- [37] N. H. Aly, A. Karameldin, and M.M. Shamloul. “Modelling and simulation of steam jet ejectors”. In: *Desalination* 123.1 (Sept. 1999), pp. 1–8. DOI: [10.1016/S0011-9164\(99\)00053-3](https://doi.org/10.1016/S0011-9164(99)00053-3).
- [38] D. Li and E. A. Groll. “Transcritical CO2 refrigeration cycle with ejector-expansion device”. In: *International Journal of Refrigeration* 28.5 (2005), pp. 766–773. ISSN: 0140-7007. DOI: <https://doi.org/10.1016/j.ijrefrig.2004.10.008>.
- [39] Y. Zhu et al. “Simplified ejector model for control and optimization”. In: *Energy Conversion and Management* 49.6 (June 2008), pp. 1424–1432. DOI: [10.1016/j.enconman.2007.12.025](https://doi.org/10.1016/j.enconman.2007.12.025).
- [40] S. Fangtian and M. Yitai. “Thermodynamic analysis of transcritical CO2 refrigeration cycle with an ejector”. In: *Applied Thermal Engineering* 31.6 (2011), pp. 1184–1189. ISSN: 1359-4311. DOI: <https://doi.org/10.1016/j.applthermaleng.2010.12.018>.
- [41] F. E. Manjili and M.A. Yavari. “Performance of a new two-stage multi-intercooling transcritical CO2 ejector refrigeration cycle”. In: *Applied Thermal Engineering* 40 (2012), pp. 202–209. ISSN: 1359-4311. DOI: <https://doi.org/10.1016/j.applthermaleng.2012.02.014>.
- [42] C. Vereda et al. “Study of an ejector-absorption refrigeration cycle with an adaptable ejector nozzle for different working conditions”. In: *Applied Energy* 97 (2012), pp. 305–312. ISSN: 0306-2619. DOI: <https://doi.org/10.1016/j.apenergy.2011.12.070>.
- [43] J. Chen, H. Havtun, and B. Palm. “Investigation of ejectors in refrigeration system: Optimum Performance Evaluation and Ejector Area Ratios Perspectives”. In: *Applied Thermal Engineering* 64.1–2 (Mar. 2014), pp. 182–191. DOI: [10.1016/j.applthermaleng.2013.12.034](https://doi.org/10.1016/j.applthermaleng.2013.12.034).
- [44] Z. Ma, H. Bao, and A.P. Roskilly. “Thermodynamic modelling and parameter determination of ejector for ejection refrigeration systems”. In: *International Journal of Refrigeration* 75 (Dec. 2016), pp. 117–128. DOI: [10.1016/j.ijrefrig.2016.12.005](https://doi.org/10.1016/j.ijrefrig.2016.12.005).
- [45] M. Mastrowski et al. “Experimental validation of the theoretical ejector model in a low-grade waste heat refrigeration system using R1233zdE as a working fluid”. In: *Applied Thermal Engineering* 236 (2024), p. 121716. ISSN: 1359-4311. DOI: <https://doi.org/10.1016/j.applthermaleng.2023.121716>.
- [46] N.S. Kumar and K.T. Ooi. “One dimensional model of an ejector with special attention to Fanno flow within the mixing chamber”. In: *Applied Thermal Engineering* 65.1 (2014), pp. 226–235. ISSN: 1359-4311. DOI: <https://doi.org/10.1016/j.applthermaleng.2013.12.055>.

- [47] J. Chen. “Investigation of Vapor Ejectors in Heat Driven Ejector Refrigeration Systems”. In: *KTH Energy Engineering* (2014). URL: <https://www.diva-portal.org/smash/record.jsf?pid=diva2%3A764519>.
- [48] S. Singh and S. Dhingra. “Thermal performance of a vapour adsorption refrigeration system: an overview”. In: *Journal of Physics: Conference Series* 1240.1 (July 2019), p. 012024. DOI: [10.1088/1742-6596/1240/1/012024](https://doi.org/10.1088/1742-6596/1240/1/012024).
- [49] W. Pridasawas and P. Lundqvist. “An exergy analysis of a solar-driven ejector refrigeration system”. In: *Solar Energy* 76.4 (2004), pp. 369–379. ISSN: 0038-092X. DOI: <https://doi.org/10.1016/j.solener.2003.11.004>.
- [50] M. Chandrashekar. “29 - HEAT PUMPS”. In: *Solar Energy Conversion II*. Ed. by A.F. Janzen and R.K. Swartman. Pergamon, 1981, pp. 447–468. ISBN: 978-0-08-025388-6. DOI: <https://doi.org/10.1016/B978-0-08-025388-6.50059-3>.
- [51] R. Ciconkov. “Refrigerants: There is still no vision for sustainable solutions”. In: *International Journal of Refrigeration* 86 (2018), pp. 441–448. ISSN: 0140-7007. DOI: <https://doi.org/10.1016/j.ijrefrig.2017.12.006>.
- [52] P. Maina and Z. Huan. “A review of carbon dioxide as a refrigerant in refrigeration technology”. In: *South African Journal of Science* 111.9/10 (July 2015), p. 10. DOI: [10.17159/sajs.2015/20140258](https://doi.org/10.17159/sajs.2015/20140258).
- [53] G. Lorentzen. “Revival of carbon dioxide as a refrigerant”. In: *International Journal of Refrigeration* 17.5 (1994), pp. 292–301. ISSN: 0140-7007. DOI: [https://doi.org/10.1016/0140-7007\(94\)90059-0](https://doi.org/10.1016/0140-7007(94)90059-0).
- [54] J. Sarkar, S. Bhattacharyya, and M. Ram Gopal. “Optimization of a transcritical CO<sub>2</sub> heat pump cycle for simultaneous cooling and heating applications”. In: *International Journal of Refrigeration* 27.8 (2004), pp. 830–838. ISSN: 0140-7007. DOI: <https://doi.org/10.1016/j.ijrefrig.2004.03.006>.
- [55] G. Grazzini, A. Milazzo, and F. Mazzelli. *Ejectors for Efficient Refrigeration: Design, Applications and Computational Fluid Dynamics*. Springer, 2018.
- [56] NASRC. *Projected Growth of CO<sub>2</sub> Refrigeration Systems*. 2023. URL: <https://nasrc.org/articles1/2023/10/18/new-nasrc-factsheet-projected-growth-of-co2-systems>.
- [57] V.K. Yadav and J. Sarkar. “Thermodynamic, economic, and environmental analyses of various novel ejector refrigeration subcooled transcritical CO<sub>2</sub> systems”. In: *International Journal of Energy Research* 45.11 (May 2021), pp. 16115–16133. DOI: [10.1002/er.6841](https://doi.org/10.1002/er.6841).
- [58] W. Weiss and M. Spörk-Dür. “Global Market Development and Trends 2023”. In: *Solar Heat Worldwide* (June 2024). DOI: [10.18777/ieashc-shww-2024-0001](https://doi.org/10.18777/ieashc-shww-2024-0001).
- [59] A. Sutur. *Newheat – flat plate collectors/industrial processes*. Aug. 2020. URL: <http://solarheateurope.eu/project/newheat-flat-plate-collectors-industrial-processes-2/>.
- [60] *Kingspan Environmental Thermomax - Hospital in Rome*. Aug. 2017. URL: <http://solarheateurope.eu/project/kingspan-environmental-thermomax-solar-heat-europe-hospital-rome/>.
- [61] M. A. Akrouh et al. “Advancements in cooling techniques for enhanced efficiency of solar photovoltaic panels: A detailed comprehensive review and innovative classification”. In: *Energy and Built Environment* (2023). ISSN: 2666-1233. DOI: <https://doi.org/10.1016/j.enbenv.2023.11.002>.
- [62] B. Perers and C. Bales. *A Solar Collector Model for TRNSYS Simulation and System Testing*. Dec. 2002. URL: <https://www.aee-intec.at/0uploads/dateien55.pdf>.

- [63] Ritter Energie. *CPC INOX Evacuated Tube Collectors - Spec Sheet*. Mar. 2023. URL: <https://ritter-energie.de/en/evacuated-tube-collector-cpc-inox/>.
- [64] Lacaze Energies. *FLAT-PLATE COLLECTOR SUN600 Technical datasheet Nr 95*. URL: <https://www.lacaze-energies.com/wp-content/uploads/2017/09/Datasheet-95-CH-Flat-plate-collector-SUN-600-1706.pdf>.
- [65] Abora. *FLAT-PLATE PVT COLLECTOR*. URL: [https://abora-solar.com/wp-content/uploads/2024/10/DS-panel\\_EN\\_v3\\_240619.pdf](https://abora-solar.com/wp-content/uploads/2024/10/DS-panel_EN_v3_240619.pdf).
- [66] G. Martinez-Rodriguez, A. L. Fuentes-Silva, and M. Picon-Nunez. “Targeting the Maximum Outlet Temperature of Solar Collectors”. In: *Chemical Engineering Transactions* 70 (Aug. 2018), pp. 1567–1572. DOI: [10.3303/CET1870262](https://doi.org/10.3303/CET1870262).
- [67] S. Salvi et al. “Technological Advances to Maximize Solar Collector Energy Output: A Review”. In: *Journal of Electronic Packaging* 140 (Aug. 2018). DOI: [10.1115/1.4041219](https://doi.org/10.1115/1.4041219).
- [68] S.Y. Alsadi and T. Foqha. “Mass flow rate optimization in solar heating systems based on a flat-plate solar collector: A case study”. In: *World Journal of Advanced Research and Reviews* 12.3 (Dec. 2021), pp. 061–071. DOI: [10.30574/wjarr.2021.12.3.0557](https://doi.org/10.30574/wjarr.2021.12.3.0557).
- [69] T. L. Bergman, A. Lavine, and F.P. Incropera. *Fundamentals of Heat and Mass Transfer*. John Wiley & Sons, Inc, 2019.
- [70] R. H. Perry, D. W. Green, and J. O. Maloney. *Perry’s Chemical Engineers’ handbook*. McGraw-Hill, 1997.
- [71] J. Oldřich. “Isentropic Efficiency of Centrifugal Compressor Working with Real Gas”. In: *Acta Polytechnica CTU Proceedings* 20 (Dec. 2018), pp. 65–72. DOI: [10.14311/APP.2018.20.0065](https://doi.org/10.14311/APP.2018.20.0065).
- [72] LG. *The Basics of a Rotary Compressor*. Apr. 2023. URL: <https://www.lg.com/global/business/compressor-motor/blog/the-basics-of-rotary-compressor>.
- [73] Atlas Copco. *Reciprocating and Rotary Compressor: What’s the Difference*. Aug. 2024. URL: <https://www.atlascopco.com/en-ae/compressors/air-compressor-blog/reciprocating-and-rotary-compressor-difference>.
- [74] C. Cuevas and J. Lebrun. “Testing and modelling of a variable speed scroll compressor”. In: *Applied Thermal Engineering* 29.2 (2009), pp. 469–478. ISSN: 1359-4311. DOI: <https://doi.org/10.1016/j.applthermaleng.2008.03.016>.
- [75] A. Guźda and N. Szmolke. “Compressors in Heat Pumps”. In: *Machine Dynamics Research* 39 (June 2016), pp. 71–83. URL: [https://www.researchgate.net/publication/313134829\\_Compressors\\_in\\_Heat\\_Pumps](https://www.researchgate.net/publication/313134829_Compressors_in_Heat_Pumps).
- [76] H. Gu et al. “Analysis, modeling and simulations of an innovative sliding vane rotary compressor with a rotating cylinder”. In: *Energy Conversion and Management* 230 (2021), p. 113822. ISSN: 0196-8904. DOI: <https://doi.org/10.1016/j.enconman.2020.113822>.
- [77] M. R. Islam. “Chapter 7 - Field guidelines”. In: *Reservoir Development*. Sustainable Oil and Gas Development Series (2022). Ed. by M. R. Islam, pp. 737–843. DOI: <https://doi.org/10.1016/B978-0-12-820053-7.00004-4>.
- [78] M. J. Moran et al. *Fundamentals of Engineering Thermodynamics*. John Wiley & Sons, Inc, 2018.
- [79] J.T. Munday and D.F. Bagster. “A new ejector theory applied to Steam Jet Refrigeration”. In: *Industrial and Engineering Chemistry Process Design and Development* 16.4 (Oct. 1977), pp. 442–449. DOI: [10.1021/i260064a003](https://doi.org/10.1021/i260064a003).

- [80] D.L. Nguyen, E.R.F. Winter, and M. Greiner. “Sonic velocity in two-phase systems”. In: *International Journal of Multiphase Flow* 7.3 (June 1981), pp. 311–320. DOI: [10.1016/0301-9322\(81\)90024-0](https://doi.org/10.1016/0301-9322(81)90024-0).
- [81] J. García del Valle et al. “An experimental investigation of a R-134a ejector refrigeration system”. In: *International Journal of Refrigeration* 46 (2014), pp. 105–113. ISSN: 0140-7007. DOI: <https://doi.org/10.1016/j.ijrefrig.2014.05.028>.
- [82] Y. Jia and C. Wenjian. “Area ratio effects to the performance of air-cooled ejector refrigeration cycle with R134a refrigerant”. In: *Energy Conversion and Management* 53.1 (2012), pp. 240–246. ISSN: 0196-8904. DOI: <https://doi.org/10.1016/j.enconman.2011.09.002>.
- [83] CHEMEUROPE. *Fanno Flow*. URL: [https://www.chemeurope.com/en/encyclopedia/Fanno\\_flow.html](https://www.chemeurope.com/en/encyclopedia/Fanno_flow.html).
- [84] H. Schlichting and K. Gersten. *Boundary-Layer Theory*. Springer, 2016.
- [85] Y. A. Çengel and J. M. Cimbala. *Fluid Mechanics: Fundamentals and Applications*. McGraw Hill, 2014.
- [86] W. Chen et al. “Theoretical analysis of ejector refrigeration system performance under overall modes”. In: *Applied Energy* 185 (2017). Clean, Efficient and Affordable Energy for a Sustainable Future, pp. 2074–2084. ISSN: 0306-2619. DOI: <https://doi.org/10.1016/j.apenergy.2016.01.103>.
- [87] E. W. Lemmon et al. *NIST Standard Reference Database 23: Reference Fluid Thermodynamic and Transport Properties-REFPROP, Version 10.0, National Institute of Standards and Technology*. 2018. DOI: <https://doi.org/10.18434/T4/1502528>.
- [88] R. E. Henry, M. A. Grolmes, and H. K. Fauske. *PRESSURE-PULSE PROPAGATION IN TWO-PHASE ONE- AND TWO-COMPONENT MIXTURES*. Tech. rep. Argonne National Lab., Ill., Jan. 1971. DOI: [10.2172/4043485](https://doi.org/10.2172/4043485). URL: <https://www.osti.gov/biblio/4043485>.
- [89] A. M. Bayen, Q. Kong, and T. Siau. *Python programming and numerical methods: A guide for engineers and scientists*. Academic Press - Elsevier, 2021. ISBN: 9780128195499.
- [90] Coochbehar Panchanan Barma University. *Physics: Bisection Method*. URL: [https://www.cbpbu.ac.in/userfiles/file/2020/STUDY\\_MAT/PHYSICS/NP%202.pdf](https://www.cbpbu.ac.in/userfiles/file/2020/STUDY_MAT/PHYSICS/NP%202.pdf).
- [91] Y. Cheng, M. Wang, and J. Yu. “Thermodynamic analysis of a novel solar-driven booster-assisted ejector refrigeration cycle”. In: *Solar Energy* 218 (Apr. 2021), pp. 85–94. DOI: [10.1016/j.solener.2021.02.031](https://doi.org/10.1016/j.solener.2021.02.031).
- [92] L. Boltzmann. “The Second Law of Thermodynamics”. In: *Theoretical Physics and Philosophical Problems: Selected Writings*. Ed. by B. McGuinness. Dordrecht: Springer Netherlands, 1974, pp. 13–32. ISBN: 978-94-010-2091-6. DOI: [10.1007/978-94-010-2091-6\\_2](https://doi.org/10.1007/978-94-010-2091-6_2).
- [93] G. Yan, T. Bai, and J. Yu. “Energy and Exergy efficiency analysis of solar driven ejector-compressor heat pump cycle”. In: *Solar Energy* 125 (Feb. 2016), pp. 243–255. DOI: [10.1016/j.solener.2015.12.021](https://doi.org/10.1016/j.solener.2015.12.021).
- [94] R. Llopis et al. “Subcooling methods for CO2 refrigeration cycles: A review”. In: *International Journal of Refrigeration* 93 (2018), pp. 85–107. ISSN: 0140-7007. DOI: <https://doi.org/10.1016/j.ijrefrig.2018.06.010>.
- [95] European Comission. *Photovoltaic Geographical Information System (PVGIS)*. URL: <https://joint-research-centre.ec.europa.eu/photovoltaic-geographical-information-system-pvgis.en>.

- [96] Solar Energy Technologies Office. *Solar Radiation Basics*. URL: <https://www.energy.gov/eere/solar/solar-radiation-basics>.
- [97] H. Beck, N. Zimmermann, and T. McVicar. “Present and future Köppen-Geiger climate classification maps at 1-km resolution”. In: *Scientific Data* 5 (2018), p. 180214. DOI: [10.1038/sdata.2018.214](https://doi.org/10.1038/sdata.2018.214).
- [98] NOAA National Centers for Environmental Information. *Guyana Weather Data - GT-BotanicalGardens (Station 81001)*. 2025. URL: [https://www.nodc.noaa.gov/archive/arc0216/0253808/2.2/data/0-data/Region-3-WMO-Normals-9120/Guyana/CSV/GTBotanicalGardens\\_81001.csv](https://www.nodc.noaa.gov/archive/arc0216/0253808/2.2/data/0-data/Region-3-WMO-Normals-9120/Guyana/CSV/GTBotanicalGardens_81001.csv).
- [99] NOAA National Centers for Environmental Information. *Niger Weather Data - Niamey Aero (Station 61052)*. 2025. URL: [https://web.archive.org/web/20240912090439/https://www.nodc.noaa.gov/archive/arc0216/0253808/4.4/data/0-data/Region-1-WMO-Normals-9120/Niger/CSV/Niamey\\_Aero\\_61052.csv](https://web.archive.org/web/20240912090439/https://www.nodc.noaa.gov/archive/arc0216/0253808/4.4/data/0-data/Region-1-WMO-Normals-9120/Niger/CSV/Niamey_Aero_61052.csv).
- [100] InfoClimat. *Climatological Normals and Records (1991-2020) for Palermo Punta Raisi*. 2025. URL: <https://www.infoclimat.fr/climatologie/normales-records/1991-2020/palermo-punta-raisi/valeurs/16405.html>.
- [101] Japan Meteorological Agency. *Weather Data from Sapporo, Japan*. 2025. URL: [https://www.data.jma.go.jp/obd/stats/etrn/view/rank\\_s.php?prec\\_no=14&block\\_no=47412&year=&month=13&day=&view=h0](https://www.data.jma.go.jp/obd/stats/etrn/view/rank_s.php?prec_no=14&block_no=47412&year=&month=13&day=&view=h0).
- [102] Buildworld. *The average home size in capital cities, based on local listings*. Jan. 2023. URL: <https://www.buildworld.co.uk/blog/archives/average-home-size-in-capital-cities?srsltid=AfmBOorcMbg2WUPhLQ1I1Q8RR15VIV8R4kwCOWX4vIB8bXogg0wryBV>.
- [103] Advanced Group. *Double Glazing U Values Explained*. June 2024. URL: <https://www.theadvancedgroup.co.uk/double-glazing-news/double-glazing-u-values-explained>.
- [104] R. Selbaş, Ö. Kızılkın, and A. Şencan. “Thermoeconomic optimization of subcooled and superheated vapor compression refrigeration cycle”. In: *Energy* 31.12 (2006), pp. 2108–2128. ISSN: 0360-5442. DOI: <https://doi.org/10.1016/j.energy.2005.10.015>.
- [105] University of Manchester. *Chemical Engineering Plant Cost Index (CEPCI)*. 2025. URL: <https://www.training.itservices.manchester.ac.uk/public/gced/CEPCI.html?reactors/CEPCI/index.html>.
- [106] M.A. Tribe and R.L.W. Alpine. “Scale economies and the “0.6 rule””. In: *Engineering Costs and Production Economics* 10.4 (1986), pp. 271–278. ISSN: 0167-188X. DOI: [https://doi.org/10.1016/S0167-188X\(86\)80025-8](https://doi.org/10.1016/S0167-188X(86)80025-8).
- [107] Sustainable.co.za. *2.0m<sup>2</sup> Vertical Flat Plate Solar Collector*. 2025. URL: <https://www.sustainable.co.za/collections/flat-plate-collectors/products/its-fp-2-0m-vertical-flat-plate-solar-collector>.
- [108] Grundfos. *UPS 25-80 180 Pump - Variant Specifications*. 2025. URL: <https://product-selection.grundfos.com/uk/products/up-ups-series-100/up-ups/ups-25-80-180-95906429?frequency=50&pumpssystemid=2587813397&tab=variant-specifications>.
- [109] International Trade Administration. *Guyana - Renewable Energy*. 2025. URL: <https://www.trade.gov/country-commercial-guides/guyana-renewable-energy>.
- [110] Global Climatescope. *Niger Market Overview*. 2025. URL: <https://www.global-climatescope.org/markets/niger>.
- [111] MOTIVA Project. *Electricity Prices in Palermo, Italy*. 2025. URL: <http://platform.motiva-project.eu/electricity-prices/italy/palermo>.

- [112] Tokyo Electric Power Company (TEPCO). *Standard Electricity Plan - Hokkaido Region*. 2025. URL: <https://www.tepco.co.jp/ep/private/plan/standard/hokkaido/index-j.html>.
- [113] Daikin UK. *What is seasonal efficiency (SCOP and SEER)*. July 2023. URL: [https://www.daikin.co.uk/en\\_gb/faq/what-is-seasonal-efficiency--scop-and-seer-.html](https://www.daikin.co.uk/en_gb/faq/what-is-seasonal-efficiency--scop-and-seer-.html).
- [114] N. Hartmann, C. Glueck, and F.P. Schmidt. “Solar cooling for small office buildings: Comparison of solar thermal and photovoltaic options for two different European climates”. In: *Renewable Energy* 36.5 (2011), pp. 1329–1338. ISSN: 0960-1481. DOI: <https://doi.org/10.1016/j.renene.2010.11.006>.
- [115] B.-J. Huang et al. “Design of direct solar PV driven air conditioner”. In: *Renewable Energy* 88 (2016), pp. 95–101. ISSN: 0960-1481. DOI: <https://doi.org/10.1016/j.renene.2015.11.026>.
- [116] D.M. Nasution et al. “Room air conditioning performance using liquid-suction heat exchanger retrofitted with R290”. In: *Case Studies in Thermal Engineering* 13 (2019), p. 100350. ISSN: 2214-157X. DOI: <https://doi.org/10.1016/j.csite.2018.11.001>.
- [117] F. Aligolzadeh and A. Hakkaki-Fard. “A novel methodology for designing a multi-ejector refrigeration system”. In: *Applied Thermal Engineering* 151 (Mar. 2019), pp. 26–37. DOI: [10.1016/j.applthermaleng.2019.01.112](https://doi.org/10.1016/j.applthermaleng.2019.01.112).
- [118] T.Q. Qureshi and S.A. Tassou. “Variable-speed capacity control in refrigeration systems”. In: *Applied Thermal Engineering* 16.2 (Feb. 1996), pp. 103–113. ISSN: 1359-4311. DOI: [https://doi.org/10.1016/1359-4311\(95\)00051-E](https://doi.org/10.1016/1359-4311(95)00051-E).
- [119] K.O. Amoabeng et al. “Analysis of indoor set-point temperature of split-type ACs on thermal comfort and energy savings for office buildings in hot-humid climates”. In: *Energy and Built Environment* 4.3 (2023), pp. 368–376. ISSN: 2666-1233. DOI: <https://doi.org/10.1016/j.enbenv.2022.02.006>.
- [120] R. Llopis et al. “Experimental evaluation of a CO2 transcritical refrigeration plant with dedicated mechanical subcooling”. In: *International Journal of Refrigeration* 69 (2016), pp. 361–368. ISSN: 0140-7007. DOI: <https://doi.org/10.1016/j.ijrefrig.2016.06.009>.
- [121] R. Fingas et al. “Experimental analysis of the R290 variable geometry ejector with a spindle”. In: *Applied Thermal Engineering* 258 (2025), p. 124632. ISSN: 1359-4311. DOI: <https://doi.org/10.1016/j.applthermaleng.2024.124632>.
- [122] J. Litardo et al. “Air-conditioning life cycle assessment research: A review of the methodology, environmental impacts, and areas of future improvement”. In: *Energy and Buildings* 296 (2023), p. 113415. ISSN: 0378-7788. DOI: <https://doi.org/10.1016/j.enbuild.2023.113415>.
- [123] A. Velthuisen. *Chilled Water Systems*. May 2019. URL: <https://www.heinenhopman.com/five-things-you-need-to-know-about-chilled-water-systems/>.
- [124] The Engineering ToolBox. *Heat Exchangers - Overall Heat Transfer Coefficients*. 2003. URL: [https://www.engineeringtoolbox.com/heat-transfer-coefficients-exchangers-d\\_450.html](https://www.engineeringtoolbox.com/heat-transfer-coefficients-exchangers-d_450.html).
- [125] CHEMEUROPE. *Absorption refrigerator*. URL: <https://preview.tinyurl.com/2hae7m4z>.
- [126] J. Sun, L. Fu, and S. Zhang. “A review of working fluids of absorption cycles”. In: *Renewable and Sustainable Energy Reviews* 16.4 (2012), pp. 1899–1906. ISSN: 1364-0321. DOI: <https://doi.org/10.1016/j.rser.2012.01.011>.
- [127] CIBSE. “Absorption refrigeration”. In: *CIBSE Journal* 10 (Sept. 2009). URL: <https://www.cibsejournal.com/cpd/modules/2009-11/#>.

- [128] V. Flores, J. Cerezo, and G. Montero. “Performance Analysis of Different Working Fluids for an Absorption Refrigeration Cycle”. In: *American Journal of Environmental Engineering* 4 (Jan. 2014). URL: <http://article.sapub.org/10.5923.s.ajee.201401.01.html>.
- [129] ASHRAE. *ASHRAE standard 34: Designation and Safety Classification of Refrigerants*. URL: <https://preview.tinyurl.com/mrxrczjp>.
- [130] Capital Electra by Siemens. *P&ID ISO Equipment*. URL: <https://radicasoftware.com/nl/>.

# A

## Absorption Refrigeration Cycles

Absorption coolers, also known as absorption chillers, are a type of refrigerator that operates by using heat to drive a refrigeration process. Absorption coolers are often implemented for commercial climate control and cooling of machinery. Absorptive refrigeration is also used to utilize waste heat for air conditioning of buildings [125]. An absorption cycle consists of four elements:

1. Evaporator: in the evaporator, the refrigerant (usually ammonia or water [126]) evaporates by absorbing heat, providing the cooling effect.
2. Absorber: in the absorber, the refrigerant vapor from the evaporator is absorbed by an absorbent (commonly water or a lithium bromide solution [126]). The absorption process creates a solution and releases heat that is dissipated into the environment via for example a condenser or cooling tower.
3. Generator: in the generator, the solution formed in the absorber is heated by an external heat source. The heating causes the refrigerant to separate from the absorbent. The refrigerant vapor is transported to the condenser, the absorbent is returned to the absorber. Together with the absorber, the generator forms the 'thermal compressor'.
4. Condenser: in the condenser, the refrigerant vapor from the generator condenses into a liquid and dissipates heat to the surroundings.

In figure A.1, a diagram of an absorption refrigeration cycle by CIBSE [127] can be viewed. The COP of Absorption refrigeration cycles lies between 0.1 and 0.7 for ammonia-water systems and between 0.5 and 0.85 for water-lithium bromide systems [128]. A limitation of the absorption system is that there exists a minimum heat source temperature  $T_{Q_{in}}$  of  $75^{\circ}C$  below which the system fails to function [18][48].

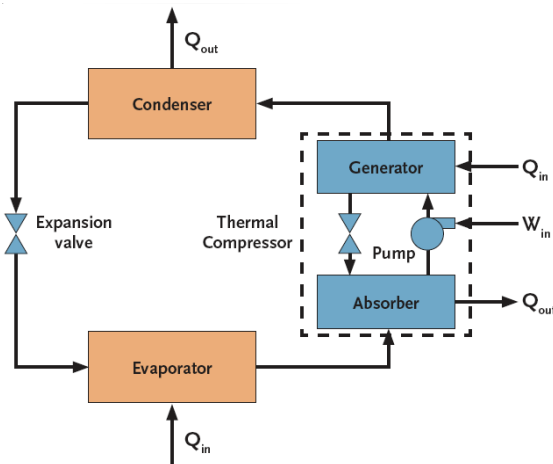


Figure A.1: Absorption refrigeration cycle. Image: [127].

# B

## Refrigerants

In table B.1, an overview of the refrigerants (denoted by their ASHRAE name) in this literature review can be read, along with their type, (common) name, GWP according to EU regulation 2024/573 [10], ODP and safety classification according to ASHRAE standard 34 [129]. In standard 34, the letter A indicates a lower toxicity, while the letter B indicates a higher toxicity. The numbers 1 through 3 indicate flammability, with 1 indicating a lower flammability and 3 a higher flammability. The addition of the letter L indicates a low burning velocity.

Refrigerant	Type	Name	GWP	ODP	ASHRAE Classification
R22	CFC	Chlorodifluoromethane	1810	Yes (High)	A1
R114	CFC	1,2-Dichlorotetrafluoroethane	10000	Yes (High)	A1
R32	HFC	Difluoromethane	675	No	A2L
R134a	HFC	1,1,1,2-Tetrafluoroethane	1430	Yes	A1
R152a	HFC	1,1-Difluoroethane	124	No	A2
R141b	HCFC	1,1-Dichloro-1-fluoroethane	725	Yes	A1
R1233zde	HFO	trans-1-chloro-3,3,3-trifluoropropene	1	No	A1
R1234ze	HFO	1,3,3,3-Tetrafluoropropene	7	No	A2L
R1234yf	HFO	2,3,3,3-Tetrafluoropropene	0.51	No	A2L
R290	HC	Propane	3	No	A3
R600a	HC	Isobutane	3	No	A3
R717	-	Hydrogen nitride (Ammonia)	0	No	B2L
R718	-	Hydrogen oxide (Water)	0	No	A1
R744	-	Carbon dioxide	1	No	A1

Table B.1: Overview of refrigerants.

## Matlab Script Ejector Model 2

In this section, the Matlab function for thermodynamic ejector model 2 can be seen.

```

1 function [pdifout, hdifout, mmn, msn] = Ejector_Function_2 (Dmnth,
    Dmnout, Dmix, Ddifout, pmnin, psn, hmnin, hsn, fluid, pcondsat)
2 %% isentropic efficiencies and settings
3
4
5 %efficiencies
6 etamn = .97; % efficiency primary nozzle
7 etamny = .93; % efficiency primary flow core
8 etasn = .45; % efficiency secondary nozzle
9 etamix = .94; % efficiency mixing
10 etadif = .93; % efficiency diffuser
11 %settings
12 fanno = 1; % fanno flow is used when equal to 1
13
14
15 %% inlet temperatures (p,s)
16
17
18 T_satmnin = refpropm('t', 'p', pmnin, 'q', 1, fluid); %
    temperature primary [Kelvin]
19 T_satsn = refpropm('t', 'p', psn, 'q', 1, fluid); % temperature
    primary [Kelvin]
20 Superheatingmn = refpropm('t', 'h', hmnin, 'p', pmnin, fluid)-
    T_satmnin;
21 Tmnin = T_satmnin + Superheatingmn; % sat temperature primary [
    Kelvin]
22 Superheatingsn = refpropm('t', 'h', hsn, 'p', psn, fluid)-T_satsn;
23 Tsn = T_satsn + Superheatingsn; % sat temperature secondary [
    Kelvin]
24 %% Conversion + Pressure calculation
25
26
27 % Areas
28 Amnth = pi*(Dmnth/1000)^2/4; % area throat [m^2]
29 Amnout = pi*(Dmnout/1000)^2/4; % area nozzle exit [m^2]
30 Amix = pi*(Dmix/1000)^2/4; % area mixing zone [m^2]
31 Addifout = pi*(Ddifout/1000)^2/4; % area diffuser [m^2]
32
33 % Calculate entropies
34 smnin = refpropm('s', 't', Tmnin, 'p', pmnin, fluid);
35 ssn = refpropm('s', 't', Tsn, 'p', psn, fluid);
36 kmnin=refpropm('K', 't', Tmnin, 'p', pmnin, fluid);
37 ksn=refpropm('K', 't', Tsn, 'p', psn, fluid);
38 amnin=refpropm('a', 't', Tmnin, 'p', pmnin, fluid);

```

```

39 asn=refpropm('a','t',Tsn,'p',psn,fluid);
40 wmnin = 0;
41 wsnin = 0;
42
43
44 %% motive nozzle throat (t)
45
46
47 pmax=pmnin;
48 pmin=pmnin*0.2;
49 err=2;
50 while abs(err)>0.01
51     pmnth=0.5*(pmin+pmax);
52     hmnthis=refpropm('h','p',pmnth,'s',smnin,fluid);
53     qmnth = refpropm('q','p',pmnth,'h',hmnthis,fluid);
54     if qmnth > 1 % Saturated vapor -> refprop
55         amnthis = refpropm('a','p',pmnth,'s',smnin,fluid);
56     else % Two-phase flow -> Nguyen relation
57         rho_ls2 = refpropm('d','p',pmnth,'q',0,fluid);
58         rho_vs2 = refpropm('d','p',pmnth,'q',1,fluid);
59         volfrac_vs2 = qmnth / rho_vs2 / (qmnth / rho_vs2 + (1 -
qmnth) / rho_ls2);
60         u_ls2 = refpropm('a','p',pmnth,'q',0,fluid);
61         u_vs2 = refpropm('a','p',pmnth,'q',1,fluid);
62         f_t = (1 - volfrac_vs2) / (u_vs2^2) + (volfrac_vs2 *
rho_ls2) / (rho_vs2 * u_vs2^2);
63         s_t = (volfrac_vs2) / (u_vs2^2) + (1 - volfrac_vs2) *
rho_vs2 / (rho_ls2 * u_ls2^2);
64         amnthis = (1 / ((1 - volfrac_vs2) * sqrt(f_t) +
volfrac_vs2 * sqrt(s_t)));
65     end
66     hmnth=etamn*(hmnthis-hmnin)+hmnin;
67     wmnth=sqrt(2*(hmnin-hmnth)+wmnin);
68
69     err=(amnthis-wmnth);
70     if err>0
71         pmax=pmnth;
72     else
73         pmin=pmnth;
74     end
75 end
76
77 rhomnth=refpropm('d','h',hmnth,'p',pmnth,fluid);
78 smnth=refpropm('s','h',hmnth,'p',pmnth,fluid);
79 mmn=Amnth*wmnth*rhomnth;
80
81 %% motive nozzle outlet (a)
82
83

```

```

84 pmax=pmnth;
85 pmin=pmnth*0.1;
86 err=2;
87 while abs(err)>1
88     pmnout=0.5*(pmin+pmax);
89     hmnoutis=refpropm('h','p',pmnout,'s',smnth,fluid);
90     hmnout=hmnth-etamn*(hmnth-hmnoutis);
91     wmnout=sqrt(2*(hmnth-hmnout)+wmnth^2);
92     rhomnout=refpropm('d','h',hmnout,'p',pmnout,fluid);
93     wmnoutcalc=mmn/rhomnout/Amnout;
94
95     err=(wmnoutcalc-wmnout);
96     if err>0
97         pmin=pmnout;
98     else
99         pmax=pmnout;
100    end
101 end
102 smnout=refpropm('s','h',hmnout,'p',pmnout,fluid);
103
104
105 %% hypothetical throat (th)
106
107
108 errorGlobal = 2;
109 iteration = 1;
110 while errorGlobal > 0
111     if iteration == 1
112         pmax=psn;
113         pmin=0.2*psn;
114         for phyphth=pmax-(pmax-pmin)/50:-(pmax-pmin)/50:pmin
115
116             hmhypis=refpropm('h','p',phyphth,'s',smnout,fluid);
117             hmhyp=hmhypis;
118             hshypis=refpropm('h','p',phyphth,'s',ssn,fluid);
119             hshyp=hsn-etasn*(hsn-hshypis);
120             rhomhyp=refpropm('d','h',hmhyp,'p',phyphth,fluid);
121             rhoshyp=refpropm('d','h',hshyp,'p',phyphth,fluid);
122
123             wmhyp=sqrt(2*(hmnout-hmhyp)+wmnout^2);
124             wshyp=sqrt(2*(hsn-hshyp)+0);
125
126             Amhyp=etamny*mmn/(rhomhyp*wmhyp);
127             Ashyp=Amix-Amhyp;
128             msn=Ashyp*rhoshyp*wshyp;
129             if phyphth==pmax-(pmax-pmin)/50
130                 else
131                     if msn-msnold<0
132                         break

```

```

133         end
134     end
135     msnold=msn;
136 end
137 msn=msnold;
138 else
139     phypth = phypth * 1.01;
140     hmhypis=refpropm('h','p',phypth,'s',smnout,fluid);
141     hmhyp=hmhypis;
142     hshypis=refpropm('h','p',phypth,'s',ssn,fluid);
143     hshyp=hsn-etasn*(hsn-hshypis);
144     rhomhyp=refpropm('d','h',hmhyp,'p',phypth,fluid);
145     rhoshyp=refpropm('d','h',hshyp,'p',phypth,fluid);
146
147     wmhyp=sqrt(2*(hmnout-hmhyp)+wmnout^2);
148     wshyp=sqrt(2*(hsn-hshyp)+0);
149
150     Amhyp=etamn*mmn/(rhomhyp*wmhyp);
151     Ashyp=Amix-Amhyp;
152     msn=Ashyp*rhoshyp*wshyp;
153 end
154
155 if phypth > psn
156     fprintf('WARNING: backflow hyp throat')
157 end
158
159
160 %% mixer inlet
161
162
163     wmixin=etamix*(mmn*wmhyp+msn*wshyp)/(mmn+msn);
164     hmixin=(mmn*(hmhyp+wmhyp^2/2)+msn*(hshyp+wshyp^2/2))/(mmn+msn)
-wmixin^2/2;
165     pmixin=phypth;
166     rhomixin=refpropm('d','h',hmixin,'p',pmixin,fluid);
167     Tmixin=refpropm('t','h',hmixin,'p',pmixin,fluid);
168     qmixin = refpropm('q','p',pmixin,'h',hmixin,fluid);
169     if qmixin > 1 % Saturated vapor -> refprop
170         amixin=refpropm('a','h',hmixin,'p',pmixin,fluid);
171     else % Two-phase flow -> Nguyen relation
172         rho_ls2 = refpropm('d','p', pmixin, 'q', 0, fluid);
173         rho_vs2 = refpropm('d','p', pmixin, 'q', 1, fluid);
174         volfrac_vs2 = qmixin / rho_vs2 / (qmixin / rho_vs2 + (1 -
qmixin) / rho_ls2);
175         u_ls2 = refpropm('a','p', pmixin, 'q', 0, fluid);
176         u_vs2 = refpropm('a','p', pmixin, 'q', 1, fluid);
177         f_t = (1 - volfrac_vs2) / (u_vs2^2) + (volfrac_vs2 *
rho_ls2) / (rho_vs2 * u_vs2^2);

```

```

178     s_t = (volfrac_vs2) / (u_vs2^2) + (1 - volfrac_vs2) *
rho_vs2 / (rho_ls2 * u_ls2^2);
179     amixin = (1 / ((1 - volfrac_vs2) * sqrt(f_t) + volfrac_vs2
* sqrt(s_t)));
180     end
181     Mmixin=wmixin/amixin;
182     kmixin=refpropm('k','p',pmixin,'q',1,fluid);
183
184
185     %% mixer outlet
186
187
188     if fanno == 1 % use fanno, schlichting etc
189         mumixin = refpropm('v','p',pmixin,'h',hmixin,fluid);
190         Remixin = wmixin*Dmix/1000*rhomixin/mumixin;
191         Lmix = 10*Dmix/1000;
192         [pmixout,Tmixout,Mmixout,kmixout,kmixavg] = Fanno_function
(pmixin,Tmixin,Mmixin,kmixin,Remixin,Lmix,fluid);
193     else
194         pmixout=pmixin;
195         Tmixout=Tmixin;
196         Mmixout=Mmixin;
197         kmixout=kmixin;
198         kmixavg=kmixin;
199     end
200
201
202     %% diffuser inlet
203
204
205     Tdifin=Tmixout*(2+Mmixout^2*(kmixavg-1))*(2*kmixavg*Mmixout
^2-(kmixavg-1))/(Mmixout^2*(kmixavg+1)^2);
206     pdifin=pmixout*1/(kmixavg+1)*(2*kmixavg*Mmixout^2-(kmixavg-1))
;
207     kdifin= refpropm('k','t',Tdifin,'p',pdifin,fluid);
208     kmixdifavg=0.5*(kmixout+kdifin);
209     Mdifin=sqrt(((kmixdifavg-1)*Mmixout^2+2)/(2*kmixavg*Mmixout
^2-(kmixdifavg-1)));
210     adifin= refpropm('a','t',Tdifin,'p',pdifin,fluid);
211     wdifin=adifin*Mdifin;
212     hdifin= refpropm('h','t',Tdifin,'p',pdifin,fluid);
213
214
215     %% diffuser outlet (d)
216
217
218     hdifout=hdifin+wdifin^2/2;
219     hdifoutis = etadif * (hdifout - hdifin) + hdifin;
220     sdifin= refpropm('s','t',Tdifin,'p',pdifin,fluid);

```

```

221 kdifoutmax = 1.5*kdifin;
222 kdifoutmin = 0.5*kdifin;
223 err = 2;
224 while abs(err) > 0.001
225     kdifout = 0.5 * (kdifoutmax + kdifoutmin);
226     kdifavg = 0.5 * (kdifin + kdifout);
227     Tdifout = Tdifin* etadif * (1+0.5*(kdifavg-1)*Mdifin^2);
228     pdifout = pdifin* etadif * (1+0.5*(kdifavg-1)*Mdifin^2)^(
kdifavg/(kdifavg-1));
229     kdif_new = refpropm('k', 't', Tdifout, 'p', pdifout, fluid
);
230
231     err=(kdif_new-kdifout);
232     if err<0
233         kdifoutmax = kdifout;
234     else
235         kdifoutmin = kdifout;
236     end
237 end
238 iteration=iteration+1;
239 errorGlobal = pcondsat - pdifout; % If error is positive,
backflow occurs
240 end
241 end

```

# D

## Symbol List

In table D.1, an overview of the symbols used for the schematic drawing can be seen. The symbols for the compressor, ejector, expansion valve and pump were obtained from Capital Electra [130].

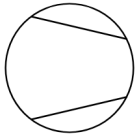
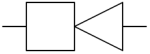
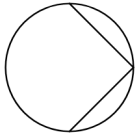
	Compressor / Booster		Expansion Valve
<b>C</b>	Condenser	<b>G</b>	Generator
	Ejector		Pump
<b>E</b>	Evaporator		

Table D.1: Symbol list. Images: [130].

## Matlab Script Hybrid 1 and MSC

## E.1 Hybrid 1

In this section, the Matlab script for the (seasonal) simulation of hybrid 1 can be seen.

```

1 %% Parameters
2
3 % Parameters ejector
4 Dt = 3.2;
5 Da = 1.5 * Dt;
6 Dm = 1.8 * Dt;
7 Dd = 4 * Dt;
8
9 % Parameters Solar Collectors
10 Asolar = 25;
11 eta0 = 0.755; % SUN600.20
12 a1 = 3.745; % SUN600.20
13 a2 = 0.015; % SUN600.20
14
15 % Parameters Compressor & Pump
16 etacomp = 0.8;
17
18 % Parameters House
19 Tin = 19.5 + 273.15;
20 Uavg = 2;
21 Area = 105;
22
23 Tdif = Tair - Tin;
24 Qcool = Uavg * Area * Tdif;
25
26 % Initialization for compressor and solar collector
27 T1 = 0 + 273.15; % Absolute zero in K
28 h1 = refpropm('h', 't', T1, 'q', 1, fluid);
29 s1 = refpropm('s', 't', T1, 'q', 1, fluid);
30
31 T4 = Tair + 5; % Condenser temperature 5 K above ambient
32 p4 = refpropm('p', 't', T4, 'q', 0, fluid); % Condenser pressure
33 h4 = refpropm('h', 'p', p4, 'q', 0, fluid); % Enthalpy
34 s4 = refpropm('s', 'p', p4, 'q', 0, fluid);
35 p3 = p4;
36
37 h7 = h4;
38 msnreal = Qcool / (h1 - h7); % kg/s
39
40 % Solar collector initialization
41 p5 = 1.7 * p4; % Fixed value for p5

```

```

42 max_iterations = 10; % Set a reasonable limit for overall
    iterations
43 iteration = 0;
44
45 p2max = p4;
46 p2min = 0.1*p4;
47 err = 2;
48 while err > 0.01
49     fail = 0;
50     iteration = iteration + 1;
51     % Adjust p2 and calculate h2
52     p2=0.5*(p2max+p2min);
53     if abs(p2 - p2min) < 1e-3 || abs(p2 - p2max) < 1e-3
54         fprintf('Skipping hour %d: p2 reached boundary\n', hour);
55         fails = fails + 1;
56         p2toohigh = 0;
57         break;
58     end
59
60     h2is = refpropm('h', 'p', p2, 's', s1, fluid);
61     h2 = h1 + (h2is - h1) / etacomp;
62     s2 = refpropm('s', 'p', p2, 'h', h2, fluid);
63
64     % Solar collector calculations
65     h5is = refpropm('h', 'p', p5, 's', s4, fluid);
66     h5 = h4 + (h5is - h4) / etacomp;
67
68     T5 = refpropm('T', 'p', p5, 's', s4, fluid);
69     T6 = T5 + 30; % Estimate temperature increase in the solar
    collector
70     if T6 > 80 + 273.15
71         fprintf('Skipping hour %d: T6 exceeded maximum limit\n',
    hour);
72         fails = fails + 1;
73         toohot = 1;
74         break;
75     end
76
77     if refpropm('t', 'p', p5, 'q', 1, fluid) > T6
78         fprintf('Skipping hour %d: T6 < Tsat\n', hour);
79         Liquid = Liquid + 1;
80         break;
81     end
82
83     p6 = p5;
84     s6 = refpropm('s', 't', T6, 'p', p6, fluid);
85     h6 = refpropm('h', 't', T6, 'p', p6, fluid);
86
87     % Solar collector efficiency and flow rate

```

```

88     Tsc = 0.5 * (T5 + T6); % Average temperature in the solar
collector
89     Tsc = 0.5 * (Tsc + T6);
90     Tstar = (Tsc - Tair) / G;
91     etasc = eta0 - a1 * Tstar - a2 * Tstar^2;
92     Qsolar = etasc * G * Asolar;
93     mmnreal = Qsolar / (h6 - h5); % kg/s
94
95     % Call ejector function
96     [p3, h3, mmn, msn, phypth, fail] = Ejector_Function_2(Dt, Da,
Dm, Dd, p6, p2, h6, h2, fluid, p4);
97     fails = fails + fail;
98
99     % Convergence check
100    ejrealratio = msnreal / mmnreal;
101    ejratio = msn / mmn;
102    err = ejrealratio - ejratio;
103
104    if err < 0
105        p2max=p2;
106    else
107        p2min=p2;
108    end
109 end
110
111 if toohot == 1
112     continue;
113 end
114
115 if p2toohigh == 1
116     h2is = refpropm('h', 'p', p2, 's', s1, fluid);
117     h2 = h1 + (h2is - h1) / etacomp;
118     Qcoolvap = msnreal * (h1 - h7);
119     Wvap = msnreal * (h2 - h1);
120     Qcooltot = Qcooltot + Qcoolvap;
121     Wtot = Wtot + Wvap;
122     COP(hour) = Qcoolvap / Wvap;
123     continue
124 end
125
126 % Skip hour if maximum iterations reached
127 if iteration == max_iterations
128     fprintf('Skipping hour %d due to non-convergence\n', hour)
    ;
129     nonconv = nonconv + 1;
130     continue;
131 end
132
133 % Accumulate results if successful

```

```

134 if iteration < max_iterations
135     Qcoolrl(hour) = msn * (h1 - h7);
136     Winrl = msn * (h2 - h1) + mmn * (h5 - h4);
137     Qcooltot = Qcooltot + Qcoolrl(hour);
138     Wtot = Wtot + Winrl;
139     COP(hour) = Qcoolrl(hour) / Winrl;
140     gamma(hour) = msn/mmn;
141     h_p_is = refpropm('h','p', p3, 's', s6, fluid);
142     h_s_is = refpropm('h','p', p3, 's', s2, fluid);
143     ej_eff(hour) = (gamma(hour)*(h_s_is-h2)/(h6-h_p_is));
144     i = i + 1;
145 end

```

## E.2 Mechanical Sub-Cooling Cycle

In this section, the Matlab script for the (seasonal) simulation of the mechanical sub-cooling cycle can be seen.

```

1 %% Parameters
2
3 % Parameters ejector
4 Dt = 3.2; % Diameter throat [mm]
5 Da = 1.5 * Dt; % Diameter nozzle outlet [mm]
6 Dm = 1.8 * Dt; % Diameter mixing area [mm]
7 Dd = 4 * Dt; % Diameter diffuser outlet [mm]
8 At = 0.25 * pi * Dt^2; Area throat [mm^2]
9 At_array = []; % Array of available throat areas
10
11
12 % Parameters Solar Collectors
13 Asolar = []; % Area of Solar Thermal Collectors
14 eta0 = 0.755; % SUN600.20
15 a1 = 3.745; % SUN600.20
16 a2 = 0.015; % SUN600.20
17
18 % Parameters Compressor
19 etacomp = 0.8; % Isentropic compressor efficiency
20
21 % Parameters House
22 Qcool = []; % Fixed Cooling load [W]
23
24 % Parameters Fluids
25 fluid_vap = 'co2'; % Working fluid vapor compression cycle
26 fluid_ej = 'propane'; % Working fluid ejector refrigeration cycle
27 SH = 5; % (Minimum) Superheating
28
29 %% Ambient Conditions
30 Tair = [] + 273.15 % Ambient Temperature
31 G = [] % Solar Irradiance

```

```

32
33 p9max = refpropm('p', 't', 70+273.15, 'q', 1, fluid_ej); % Upper
    limit generator pressure to ensure evaporation
34 p9min = 1600; % Lower limit primary pressure for ejector model
35
36 %% Assumed Constant Points
37
38 % Point 6, Evaporator outlet EJ cycle
39 T6 = 20 + 273.15;
40 p6 = refpropm('p', 't', T6, 'q', 1, fluid_ej);
41 h6 = refpropm('h', 't', T6, 'q', 1, fluid_ej);
42 s6 = refpropm('s', 't', T6, 'q', 1, fluid_ej);
43
44 % Point 1, Evaporator outlet EJ cycle
45 T1 = 0 + 273.15;
46 h1 = refpropm('h', 't', T1, 'q', 1, fluid_vap);
47 s1 = refpropm('s', 't', T1, 'q', 1, fluid_vap);
48
49 %% Simulation Ejector Cycle to Find Qms
50 ratio = 0
51
52 % Point 8
53 T8 = Tair+5;
54 p8 = refpropm('p', 't', T8, 'q', 0, fluid_ej);
55 h8 = refpropm('h', 'p', p8, 'q', 0, fluid_ej);
56 s8 = refpropm('s', 'p', p8, 'q', 0, fluid_ej);
57 h11 = h8;
58
59 p9 = p9max;
60 errp9 = 2;
61 COPold = 1;
62 while errp9 > 0
63
64     % Point 9
65     h9is = refpropm('h', 'p', p9, 's', s8, fluid_ej);
66     h9 = h8 + (h9is - h8) / etacomp;
67
68     % Point 10
69     Tsat = refpropm('T', 'p', p9, 'q', 1, fluid_ej); % fixed
    superheating
70     T10 = Tsat + SH;
71     h10 = refpropm('h', 't', T10, 'p', p9, fluid_ej);
72
73     % Solar collector efficiency and flow rate
74     Tsc = 0.5 * (Tsat + T10); % Average temperature in the solar
    collector
75     Tsc = 0.5 * (Tsc + T10);
76     Tstar = (Tsc - Tair) / G;
77     etasc = eta0 - a1 * Tstar - a2 * Tstar^2;

```

```

78 Qsolar = etasc * G * Asolar;
79 mmnsolar = Qsolar / (h10 - h9); % kg/s
80 [~, ~, mmn, msn] = Ejector_Function_2(Dt, Da, Dm, Dd, p9, p6,
h10, h6, fluid_ej, p8);
81
82 COPnew = msn*(h6-h11)/(mmn*(h9-h8));
83 errp9 = COPnew-COPold;
84 if errp9 < 0
85     p9 = p9old;
86     h9 = h9old;
87     msn = msnold;
88     break
89 end
90 p9old = p9;
91 h9old = h9;
92 COPold = COPnew;
93 msnold = msn;
94 p9 = p9-50;
95 if p9-p9min < 1e-3
96     p9 = p9old;
97     h9 = h9old;
98     break
99 end
100 end
101
102 if msn > 0
103     % Adjust ejector geometry
104     [mmnej, Dt, Da, Dm, Dd, At] = update_ej(mmnsolar, mmn,
At_array, At, Dt, Da, Dm, Dd);
105
106     % Adjust Point 9 and 10
107     [p9, h9, pptoolow, ~, h10, s10] = realprimarypressure(p9,
p9min, s8, h8, etacomp, SH, Tair, G, eta0, a1, a2, Asolar,
mmnej, fluid_ej);
108
109     % Find real secondary massflow and gamma
110     [p7, h7, mmn, msn] = Ejector_Function_2(Dt, Da, Dm, Dd, p9, p6
, h10, h6, fluid_ej, p8);
111     ratio = msn/mmn;
112 end
113
114 Qms = msn * (h6 - h11);
115
116 %% Simulation Vap Comp Cycle
117
118 COPold = e-10;
119 p2 = 14000; % Start at 140 bar then decrease to optimize
120 p2err = 2;
121

```

```

122 while p2err > 0
123
124     % Point 2
125     h2is = refpropm('h', 'p', p2, 's', s1, fluid_vap);
126     h2 = h1 + (h2is - h1) / etacomp;
127
128     % Point 3
129     p3 = p2;
130     T3 = Tair + 5;
131     h3 = refpropm('h', 't', T3, 'p', p3, fluid_vap);
132     if h3 > h1
133         h2 = h2old;
134         h5 = h5old;
135         mCO2 = mCO2old;
136         break
137     end
138
139     mCO2max = 0.7;
140     mCO2min = 0.0001;
141     mCO2err = 2;
142
143     while abs(mCO2err) > 1e-3
144         mCO2 = 0.5 * (mCO2min+mCO2max);
145         toobig = 0;
146         % Point 4
147         h4 = h3 - Qms / mCO2;
148         % Point 5
149         h5 = max(h4,refpropm('h', 't', T6+5, 'p', p3, fluid_vap));
150         % Can't cool past DeltaT limit
151         mCO2check = Qcool/(h1-h5);
152         mCO2err = mCO2-mCO2check;
153         if mCO2 > mCO2check
154             mCO2max = mCO2;
155         else
156             mCO2min = mCO2;
157         end
158     end
159
160     COPnew = (h1-h5)/(h2-h1);
161     p2err = COPnew-COPold;
162     if p2err < 0
163         h2 = h2old;
164         h5 = h5old;
165         mCO2 = mCO2old;
166         break
167     end
168     p2 = p2 - 50;
169     h2old = h2;
170     h5old = h5;

```

```

170     COPold = COPnew;
171     mCO2old = mCO2;
172 end
173
174 %% Accumulate Results for either EJ+Vap or Vap
175
176 if ratio > 0
177     h_p_is = refpropm('h','p', p7, 's', s10, fluid_ej);
178     h_s_is = refpropm('h','p', p7, 's', s6, fluid_ej);
179     gamma = ratio;
180     ej_eff = ratio*(h_s_is-h6)/(h10-h_p_is);
181     Qcool = mCO2*(h1-h5);
182     Win = mCO2*(h2-h1)+mmn*(h9-h8);
183     COP = Qcool/Win;
184     Qcooltot = Qcooltot + Qcool;
185     Wtot = Wtot + Win;
186 else
187     Qcool = mCO2*(h1-h5);
188     Win = mCO2*(h2-h1);
189     COP = Qcool/Win;
190     Qcooltot = Qcooltot + Qcool;
191     Wtot = Wtot + Win;
192 end

```

## Ejector Array Optimization Script

In this section, the Python script for determining the optimal throat diameters in an array of ejectors can be seen.

```

1 import numpy as np
2 from itertools import combinations
3 import matplotlib.pyplot as plt
4
5 # input
6 num_pipes = 7 #<-- Set number of ejectors
7 num_generated = 20 #<-- Set number of combinations to be tried \
8     # num_generated best kept below 20 for speed
9
10 def circ_area(diameter):
11     return np.pi * (diameter / 2) ** 2
12
13 def gnrt_d(lwr_bnd, uppr_bnd, num_pipes):
14     min_d = (lwr_bnd / np.pi) ** 0.5 * 2
15     max_d = (uppr_bnd / np.pi) ** 0.5 * 2
16     return np.linspace(min_d, max_d, num_pipes)
17
18 lwr_bnd = 0.2 * 1e-6 #<-- Set lower bound area
19 uppr_bnd = 15 * 1e-6 #<-- Set upper bound area
20 d_set = gnrt_d(lwr_bnd, uppr_bnd, num_generated)
21 best_comb = None
22 min_gap_std = float('inf')
23
24 for combination in combinations(d_set, num_pipes):
25     areas = [circ_area(d) for d in combination]
26     comb_areas = set()
27
28     for r in range(1, num_pipes + 1):
29         for subset in combinations(areas, r):
30             comb_areas.add(sum(subset))
31
32     sorted_areas = sorted(comb_areas)
33
34     if max(sorted_areas) >= uppr_bnd and min(sorted_areas) <= lwr_bnd:
35         gaps = np.diff(sorted_areas)
36         gap_std = np.std(gaps)
37
38         if gap_std < min_gap_std:
39             min_gap_std = gap_std
40             best_comb = combination
41
42 if best_comb is None:
43     raise ValueError("No combination achieves the required range \
44         consider adding more ejectors.")
45
46 areas = [circ_area(d) for d in best_comb[:num_pipes]]
47
48 comb_areas = set()
49 for r in range(1, len(areas) + 1):
50     for subset in combinations(areas, r):
51         comb_areas.add(sum(subset))
52
53 areas_array = [area * 1e6 for area in sorted(comb_areas)]
54 max_area = max(areas_array)

```

# Pressure Optimization R744 Vapor Compression

In figure G.1 the evolution of the COP of a R744 ( $CO_2$ ) vapor compression cycle versus the gas-cooler pressure can be seen for different values of ambient temperature.

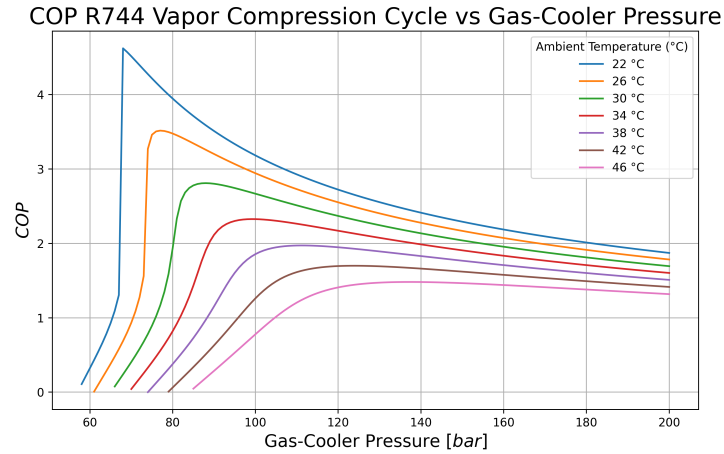


Figure G.1: COP R744 vapor compression cycle vs gas-cooler pressure.

The numerical values of the COP for relevant points are also included in table G.1. A dash indicates the gas-cooler pressure is too low for heat rejection and thus refrigeration at that ambient temperature.

Gas-Cooler Pressure (bar)	$COP_{T_{air} = 22\text{ }^\circ C}$	$COP_{T_{air} = 26\text{ }^\circ C}$	$COP_{T_{air} = 30\text{ }^\circ C}$	$COP_{T_{air} = 34\text{ }^\circ C}$	$COP_{T_{air} = 38\text{ }^\circ C}$	$COP_{T_{air} = 42\text{ }^\circ C}$	$COP_{T_{air} = 46\text{ }^\circ C}$
50	-	-	-	-	-	-	-
60	0.32	-	-	-	-	-	-
70	4.52	0.93	0.41	0.04	-	-	-
80	3.95	3.48	1.93	0.82	0.38	0.06	-
90	3.51	3.20	2.80	2.12	1.15	0.63	0.29
100	3.18	2.94	2.67	2.33	1.86	1.26	0.78
110	2.93	2.73	2.51	2.26	1.97	1.61	1.20
120	2.72	2.55	2.37	2.17	1.95	1.70	1.41
130	2.55	2.40	2.24	2.08	1.89	1.69	1.47
140	2.41	2.28	2.14	1.99	1.83	1.66	1.48
150	2.29	2.17	2.04	1.91	1.77	1.62	1.47
160	2.19	2.07	1.96	1.83	1.71	1.58	1.44

Table G.1: COP R744 vapor compression cycle for different gas-cooler pressures.